
Graduate Team Aircraft Design Competition: Electric Vertical Takeoff and Landing (E-VTOL) Aircraft Mistral Air Taxi




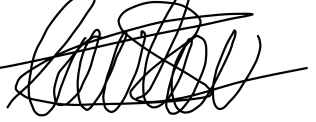




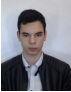









Team Name: The Huggy's Birds

S. ADDARKAOUI TAARABT	A. BERNIER
Y. CHEN	H. COMPERE
A. DORE	M. FRANSOLET
R. JUMPERTZ	L. MACCHIAIOLO

Faculty members:

Prof. G. DIMITRIADIS	Prof. L. NOELS
A. CROVATO	T. LAMBERT

Team member	AIAA number	Email adress	Signature	
	Saddik ADDARKAOUI	976674	s.addarkaoui@student.uliege.be	
	Albin BERNIER	976496	Albin.bernier@student.uliege.be	
	Yusi CHEN	977157	Yusi.Chen@student.uliege.be	
	Haiming COMPERE	976490	Haiming.Compere@student.uliege.be	
	Antoine DORE	976493	antoine.dore@student.uliege.be	
	Maxime FRANSOLET	977254	Maxime.Fransolet@student.uliege.be	
	Remy JUMPERTZ	965295	Remy.Jumpertz@student.uliege.be	
	Luca MACCHIAIOLO	976966	luca.macchiaiolo@student.uliege.be	

Contents

List of Figures

List of Tables

Nomenclature

1 Mistral Air Taxi design

1	Introduction	1
1.1	Context	1
2	Mission description and design objectives	2
2.1	State-of-the-art of VTOL technology	2
2.2	Mission and RFP analysis	3
3	Methodology	4
4	Design selection	5
5	Weight estimation	6
5.1	First mass estimation	6
5.2	Subsequent mass estimations	7
6	CAD	7
7	Components design	9
7.1	Fuselage	9
7.2	Wing	11
7.3	Canard	14
7.4	Control surfaces	15
7.5	Propulsion & energy systems	16
7.6	Electronic system	20
7.7	Landing gear	24
7.8	Autonomous system	26
8	Aerodynamic study	30
8.1	Tranair	30
8.2	Drag analysis.	33
9	Structure design	37
9.1	Flight Envelope	37
9.2	Loading	39

i

iii

iii

1

9.3	Materials selection	42
9.4	Fuselage section	44
9.5	Wing	48
9.6	Structure Conclusion	53
10	Stability analysis	54
10.1	Pitching moment stability	54
10.2	Dynamic analysis	56
10.3	Yaw controls	59
11	Aircraft performance	60
11.1	Segment Analysis	61
11.2	Reserve mission	71
11.3	Global Results	71
11.4	Point Performances	72
12	Mechanism	74
13	Trade-off study	78
13.1	Wing characteristics	78
14	Cost analysis	79
14.1	Method used	80
14.2	Market size and potential	80
14.3	Development and manufacturing costs	81
14.4	Break-even analysis	82
14.5	Operating costs	84
14.6	Comparison with other means of transport	84
15	Conclusion	86

Bibliography 87

A Appendix 90

1	Batteries	90
2	Dynamic analysis	91
3	Autonomous system cost breakdown	91
4	Cost comparison between different means of transport	92

List of Figures

1.1	Mobility mix shift. Comparison of Boston, Berlin and Shanghai.	1
1.2	CityAirbus	3
1.3	Lilium Jet	3
1.4	Aurora Passenger Air Vehicle	3
1.5	General view of a typical mission of the E-VTOL.	3
1.6	Schematic of the general methodology adopted for the conceptual design phase.	5
1.7	Percentage of gross weight.	7
1.8	Realistic view of Mistral Air Taxis.	8
1.9	Side, front and top view of the Mistral Air Taxi.	8
1.10	Top view	9
1.11	Lateral view	9
1.12	Position of CG (inches)	9
1.13	Proposed design for the main cabin.	10
1.14	Side view of the fuselage showing the dimensions.	10
1.15	Cabin interior view.	11
1.16	Wing airfoil NACA2412.	12
1.17	Comparison of the 3D lift coefficient and the 2D lift coefficient.	13
1.18	Canard airfoil NACA6412.	14
1.19	Top and lateral views of the elevons.	16
1.20	Engines power for sizing mission.	19
1.21	Payload range diagram.	22
1.22	Propulsion system on the canard.	22
1.23	Flight (left) and take-off (right) configurations for wing engines.	23
1.24	Views and locations for wing propulsion.	23
1.25	Landing gear geometric parameters.	24
1.26	Landing gear geometric parameters.	25
1.27	Certification and validation schedule proposed by Uber[40].	27

1.30	Autonomous system architecture. In yellow the aircraft, in green the public ATC and in grey the other flying objects.	29	1.59	The red and the blue lines represent the peak power required by the engines for the transition phase, expressed in percentage with respect to the hover nominal power. In yellow is presented the energy requirement trend with respect to the total transition period.	64
1.31	Airplane lift curve from <i>Tranair</i> and from the conceptual design.	31	1.60	Lift produced at the end of the transition period as function of the transition period.	64
1.32	Airplane drag polar from <i>Tranair</i> and from the conceptual design.	31	1.61	Wing, canard thrust (magnitudes) and lift profile over the transition phase.	65
1.33	Section lift coefficient along the half-span of the wing, in cruise, with and without the effect of the canard.	32	1.62	Wing engine thrust and energy consumption as a function of the desired vertical velocity.	66
1.34	Wing lift curve with and without the canard.	32	1.63	Wing engine thrust and energy consumption as a function of the cruise altitude.	66
1.35	Section lift coefficient along the half-span of the canard, at cruise, with and without the effect of the wing. The reference chord is c_w	33	1.64	Wing engine thrust and energy consumption as function of the cruise velocity.	67
1.36	Division of the drag.	35	1.65	Thrust and energy requirement with respect to cruise velocity.	67
1.37	Division of the different type of drag.	35	1.66	Maximum vertical velocities as function of cruise velocity.	67
1.38	Airplane drag polars obtained from <i>Tranair</i> and from empirical methods (advanced and conceptual design).	36	1.67	Thrust and energy requirement with respect to desired descending velocity at $V_{Descent}$	68
1.39	Design cruise (blue) and dive (dashed blue) velocities (TAS) as a function of the altitude.	38	1.68	Energy consumption as function of de-transient period.	68
1.40	Maneuver (red) and gust (blue) envelopes of the Mistral Air Taxi.	38	1.69	Wing and canard engine thrust profile (magnitude) as function of de-transient period.	68
1.41	Schematics of the aerodynamic forces acting on the aircraft.	39	1.70	Wing and canard engine thrust (magnitude) profile during breaking.	70
1.42	Position of stringers (red circles). The cross red is the centroid of the fuselage section.	47	1.71	Trend of the different drags during the breaking manoeuvre with the horizontal velocity profile (in purple).	70
1.43	Mesh of the fuselage structure.	47	1.72	Relation between sizing mission energy and reserve mission energy.	71
1.44	Deformation of the fuselage under maximum loading at point C of the flight envelope.	48	1.73	Partition of energy consumption during the sizing mission.	72
1.45	Position of stringers and flanges (red circles) and spars (blue). The red cross is the centroid of the wing section.	51	1.74	Phases time period.	72
1.46	Internal structure of the wing as studied using NX.	51	1.75	Phases covered distance.	72
1.47	Mesh of the wing structure.	51	1.76	Thrust profiles (absolute value of thrust) during transitions; dashed lines represent the thrusts profile for sizing mission, solid lines are the "high and hot" ones.	74
1.48	Maximal principal stresses on the structure of the wing under maximum loading at point B of the flight envelope.	53	1.77	Mechanism block diagram.	75
1.49	Deflection of the wing under maximum loading at point B of the flight envelope.	53	1.78	Engine motion diagram: from the top to the bottom 1) position as function of time 2) angular velocity as function of time 3) angular acceleration as function of time.	76
1.50	Important lever arms used for the pitching moment stability.	54	1.79	Tilting system installation.	77
1.51	Schematic of the elevator.	55	1.80	E-VTOL market size evolution and regional split between the year 2025 and 2035 from [59].	80
1.52	Representation in the complex plane.	57	1.81	Comparison of the labor cost in different countries [60].	81
1.53	Lateral velocity v perturbation evolution.	59	1.82	The development cost in millions of dollars as a function of units produced.	83
1.54	Roll angle ϕ and roll angular velocity p evolution.	59	1.83	Fixed cost, total cost and revenue as a function of the number of units produced.	83
1.55	Yaw angle ψ and yaw velocity r evolution. The dotted line represent the commanded yaw angle	60	1.84	Trip between New York and New Haven[61].	85
1.56	Segment analysis flow path.	61			
1.57	Thrust behaviour with respect to RPM^2 of the wing engines.	62			
1.58	Approximation of the thrust profile as function of RPM^2 for wing engines for a flight velocity of $v = 134mph$	62			

1.85 Trip between Newark and Kennedy airports [61].	85
A.1 Strengths and weaknesses of lead-acid, NiMH and NiCd batteries.	90

A.2 Autonomous system cost breakdown [70].	91
A.3 Volumetric energy density trends.[69]	92
A.4 Power density trends.[69]	92
A.5 BLADE Airport lines in New York.	93

List of Tables

1.1 Table of the main concept of E-VTOL aircraft currently in development.	2	1.23 Allowed configurations.	55
1.2 E-VTOL configurations.	3	1.24 controls fixed and free stability margins	55
1.3 Table of some of the aircraft considered for the first mass estimation.	6	1.25 Characteristics of the vibration modes of the aircraft.	58
1.4 Complete weight breakdown.	7	1.26 Aircraft mode of vibration under LQI control action.	59
1.5 Features of the wing.	14	1.27 Hovering results.	63
1.6 Summary of the main parameters of the canard.	15	1.28 Transient results.	65
1.7 Characteristics of the elevons.	16	1.29 Climb results for minimum requirements.	66
1.8 Global propellers characteristics.	18	1.30 Cruise results.	67
1.9 Comparison between different electric motors.	19	1.31 Descent results.	68
1.10 Electric motors characteristics and operating points for takeoff and cruse.	20	1.32 De-transient results.	69
1.11 Characteristics of the batteries. The total stands for 2 wing’s battery pack and 1 canard’s battery pack	21	1.33 Breaking results.	70
1.12 Landing gear Placement	25	1.34 Landing results.	70
1.13 Landing gear loads.	25	1.35 De-transient results.	71
1.14 Tire selection and specifications.	26	1.36 Hovering results.	73
1.15 Contributions of drag component at cruise.	34	1.37 Transient results.	74
1.16 Drag coefficients in cruise conditions evaluated via <i>Tranair</i> and via empirical methods.	37	1.38 Engine dynamics parameter for a cluster of seven engines.	77
1.17 Critical points of the flight envelope and aeronautical loads.	40	1.39 From the motor and transmission selection, sizes and system parameter are presented.	77
1.18 Structural loading on the fuselage for the critical points of the flight envelope.	41	1.40 Trade-off analysis for the aspect ratio of the wing. The values represent the % of variation with respect to the reference configuration obtained after the design.	79
1.19 Structural loading at the wing root for the critical points of the flight envelope.	42	1.41 Breakdown of the certification cost for the aircraft.	81
1.20 Mechanical properties of the selected composite.	44	1.42 Breakdown of the total cost for one aircraft.	82
1.21 Values of the main structural elements obtained with the analytical study.	51	1.43 Breakdown of the operating cost per aircraft.	84
1.22 Values of the main structural elements obtained through finite element analysis.	52	1.44 Comparison of different means of transport in terms of travel time and cost for a trip from New York to New Haven.	85
		1.45 Comparison of different means of transport in terms of travel time and cost for a trip from Newark to Kennedy Airport.	85

Nomenclature

List of acronyms

AC	Alternating Current	ATM	Air Traffic Management
ADS-B	Automatic Dependent Surveillance-Broadcast	BEM	Blade Element Method
AIAA	American Institute of Aeronautics and Astronautics	BEMT	Blade Element Method Theory
ATC	Air Traffic Control	BLDC	BrushLess DC
		BMI	Bismaleimide

CAD Computer - Aided Design
 CFD Computational Fluid Dynamics
 CG Center of Gravity
 CPI Consumer Price Index
 CPU Central Processing Unit
 CS Certification Specifications
 DC Direct Current
 DEP Distributed Electric Propulsion
 DGPS Differential Global Positioning System
 DOF Degree Of Freedom
 E-VTOL Electric Vertical Takeoff and Landing
 EIPF Earth Inertial Reference Frame
 EIS Entry Into Service
 EoM Equation of Motion
 EV Electric Vehicle
 FAA Federal Aviation Administration
 FAR Federal Aviation Regulation
 FEM Finite Element Method
 FWD Forward
 GA General Aviation
 GNSS Global Navigation Satellite System
 GPS Global Position System
 GPU Graphics Processing Unit
 HSI Hyperspectral Imaging Systems
 IFR Instrument Flight Rules
 ISA International Standard Atmosphere
 LHS Left Hand Side
 LQI Linear Quadratic Integral control
 MAC Mean aerodynamic chord
 MGTOW Maximum Gross Take-Off Weight
 MSI Multispectral Imaging Systems
 MSL Mean Seal Level
 MTOW Maximum Take-Off Weight
 MV Medium Voltage
 NACA National Advisory Committee for Aeronautics

NASA National Aeronautics and Space Administration
 ODM On-Demand Mobility
 PAV Passenger Air Vehicle
 PEEK Polyether Ether Ketone
 RFP Request For Proposal
 RHS Right Hand Side
 RPM Rotations Per Minute
 RTDC Research Development Testing and Certification
 SAE Society of Automotive Engineers
 SMPM Synchronous Motor Permanent Magnet
 SPO short Period oscillations
 STOL Short Takeoff and Landing
 TAS True Airspeed
 TRL Technology readiness level
 UAM Urban Air Mobility
 UN United Nations
 USA United States of America
 UV Ultra Violet
 VFR Visual Flight Rules
 VTOL Vertical Takeoff and Landing

List of symbols

α Angle of attack $^{\circ}$
 \ddot{x} Acceleration on EIRF x-axis ft/s^2
 \ddot{y} Acceleration on EIRF y-axis ft/s^2
 δ Maximum deflection $^{\circ}$
 η Engine efficiency -
 γ Climb angle rad
 λ Taper -
 Ω Angle between hovering pointing direction of engine and the axis of the propeller rad
 ρ Air density lb/ft^3
 σ Duct expansion ratio -
 A Disk actuator area of the ducted fan ft^2
 a The slope of the 3D lift -
 AR Aspect ratio -
 b Span ft
 B_{dens} Battery density KW/kg

B_{dens}	Battery energy density	Wh/kg	l_c	Distance between CG and the point of application of canard thrust along roll axis	ft
c	Chord	ft			
C_D	Drag Coefficient	-	$l_c P$	Distance between CG and the aerodynamic center of canard along roll axis	ft
C_L	Lift Coefficient	-	l_w	Distance between CG and the point of application of wing thrust along roll axis	ft
$C_{D,0}$	Zero-Lift Drag Coefficient	-			
$C_{l,\alpha}$	airfoil slope of the lift curve	rad^{-1}	$l_w P$	Distance between CG and the aerodynamic center of wing along roll axis	ft
C_{L3D}	3D lift coefficient	-	M_{peak}	Mass of battery packs	W/kg
$C_{L\alpha}$	Lift coefficient derivative with respect to the angle of attack	rad^{-1}	P	Power required per engine	KW
$C_{M\alpha,c/4}$	Moment coefficient at the quarter chord	-	P_a	Available power	KW
D	Total drag of the aircraft	lbf	P_r	Required power	KW
d	Distance covered during certain phase	ft	P_{peak}	Peak specific power	W/kg
D_e	Drag due to engines movable part	lbf	P_{TOT}	Power required by the engines	W/kg
D_s	Drag due to Airbreakers	ft	S	Surface	ft^2
E	Energy	KW	T	Thrust	lbf
e	Oswald efficiency factor	-	V	Aircraft velocity	ft/s
$E_{mission}$	Mission energy	Wh	W	Total weight of aircraft	lb
h_c	Distance between CG and the point of application of canard thrust along yaw axis	ft	x_{AC}	Chordwise coordinate of the aerodynamic center	in
h_w	Distance between CG and the point of application of wing thrust along yaw axis	ft			
i	Incidence angle	$^\circ$			
L	Total lift of the aircraft	lbf	w	Wing	

List of subscript

- c Canard
- e Elevons
- s Spoiler
- w Wing

1 Mistral Air Taxi design

1 Introduction

In response to the Request for Proposal (RFP) emitted by the American Institute of Aeronautics and Astronautic (AIAA) in the context of the 2018-2019 graduate team aircraft competition, we, the members of the Huggy's bird team are proud to present the Mistral Air Taxi. The Mistral Air Taxi is a four-seater Electric Vertical Takeoff and Landing aircraft (E-VTOL).

This report is the work of a team of eight students who are enrolled in the first year of the Master's degree in Aerospace Engineering at the University of Liège in Belgium. This project is part of the official curriculum and was supervised by several faculty members, including professors L. Noels and G. Dimitriadis.

The report starts with an analysis of the E-VTOL aircraft market and a presentation of the design methodology. Then, the possible configurations are discussed. The core of the report presents the design of the different components of the aircraft. The performance is also studied into details. Lastly, an economical study of the aircraft is performed.

1.1 Context

According to the figures presented in a 2014 United Nations' (UN) report on world's urbanization [1], more than half (54 %) of the world population lives in a urban environment. In North America, this figure even rises to 82 %. It is projected that by 2050, 66 % of the world's population will be living in an urban area. This will inevitably pose great challenges in terms of mobility. Already today, it is estimated that 64 % of the kilometers travelled each year take place in urban areas. This number is only expected to rise as the urban population increases. It is in this context that companies like Uber Elevate are developing new services for unscheduled on-demand air transportation [2][3]. This new kind of service has a great commercial potential. Researches conducted in different cities have shown that airport and end-to-end city transfers, as well as daily commuting are the most promising segments [3]. Future transportation trends are shown in Fig. 1.1. A decrease of personal and mass transit is expected, favoring an *uberisation* of the transport sector and enhancing the urban mobility mix where E-VTOL aircraft have a clear advantage: movement in 3D space [4].

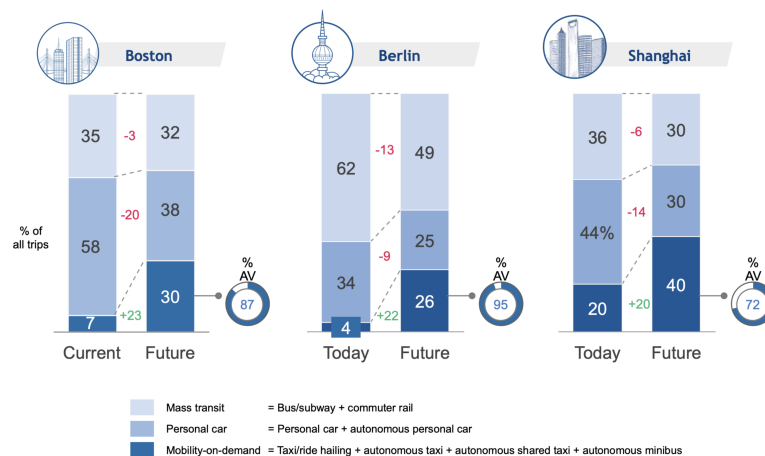


Figure 1.1: Mobility mix shift. Comparison of Boston, Berlin and Shanghai.

Moreover, the most recent improvements in electric motors and battery technology have prompted new interest in all-electric aircraft propulsion. Even though the power requirements for longer trips or airliners are far from being met, all-electric propulsion could be applied in the context of smaller vehicles performing shorter trips. These smaller vehicles would be well suited for urban mobility [5].

In consideration of the above, several companies have started designing new concepts of electric aircraft that could meet the future demand for urban air mobility. Currently, no concept of E-VTOL has yet been commercialised. Some of the most notable project are presented in Table 1.1. It is in the same context that the AIAA has emitted the RFP for the design of an E-VTOL aircraft.

Name	Company	# of passengers	Status
Lilium jet	Lilium GmbH	2 (expected 5)	undergoing test flights
A3 Vahana	Airbus	2	undergoing test flights
Aurora Passenger Air Vehicle (PAV)	Aurora (Boeing)	2	undergoing test flights
Bartini flying car	Bartini	2 or 4	under development
DreamMaker	Embraer	4 (+1 pilot)	under development
KittyHawk	Cora	2	undergoing test flights
CityAirbus	Airbus Helicopter	4	under development
Volocopter 2X	Volocopter	2	undergoing testing

Table 1.1: Table of the main concept of E-VTOL aircraft currently in development.

2 Mission description and design objectives

2.1 State-of-the-art of VTOL technology

The purpose of the conceptual design is to define an initial configuration for the aircraft. In order to do so, a review of the state-of-the-art of E-VTOLs is carried out. One of the main problems to tackle when designing an E-VTOL is the vertical takeoff and landing capabilities. Currently, there exist very few aircraft that are capable of such a feat. Example of VTOL aircraft include the F35-B or the V-22 Osprey.

There are basically three ways to tackle this issue: either the aircraft is built like an helicopter and the lift is produced exclusively by rotors, or the lift is produced by wings during the flight. In the second case, the takeoff lift is either produced by a set of fixed motors different from the motors producing the thrust (lift + cruise), or by the same engines that will produce the thrust during the flight (vectored thrust). In the latter case, the motors must tilt to provide thrust. Each configuration has its own advantages and disadvantages, summarized in Table 1.2.




Classification	Illustration	(+) Benefits	(-) Disadvantages
Wingless	 <p>Figure 1.2: CityAirbus</p>	Compactness Efficiency in hovering	Energy consumption in cruise Complex
Vectored thrust	 <p>Figure 1.3: Lilium Jet</p>	Reduced Mass VTOL + STOL	Complex manoeuvres Tilting mechanism
Lift + Cruise	 <p>Figure 1.4: Aurora Passenger Air Vehicle</p>	Simplicity VTOL + STOL No tilting mechanism	Mass Unused propellers Drag

Table 1.2: E-VTOL configurations.

2.2 Mission and RFP analysis

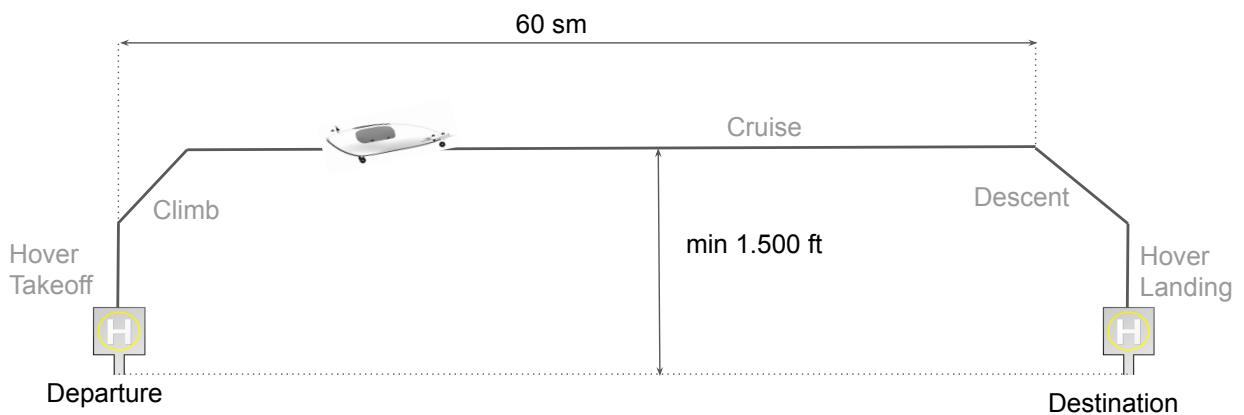


Figure 1.5: General view of a typical mission of the E-VTOL.

The general requirements to be met by the aircraft are defined in the RFP of the AIAA and are summarized below:

- Must be able to transport 4 people (1 pilot and 3 passengers or 4 passengers), each person weighing 180 lb (+20 lb of luggage for each passengers);

- Must be able to take off and land vertically, as well as hover;
- Minimum cruising altitude is 1,500 ft;
- Average speed during cruise and climbing must be at least 150 mph;
- Maximum speed of at least 176 mph at altitudes between 1,500 and 3,000 feet;
- Must have a minimum range of 60 statute miles;
- In case a landing is aborted, the aircraft must be able to divert to an alternate landing spot located at a distance of 2 statute miles from the original location;
- Average climb rate not to exceed 500 feet/min;
- Descent rate not to exceed 1,000 feet/min;
- FAA part 23 airworthiness requirements must be met;
- Capable of VFR and IFR flight with autopilot;
- Can be fully autonomous.

3 Methodology

The conceptual design of the aircraft begins with a careful study of the requirements defined in the proposal, as well as a market review. Some key parameters of the airplane are then fixed. Empirical formulas can be used to compute quantities such as the mass, the wing area or the required thrust. However, due to the interdependence between each quantity, this work is an iterative process. It is therefore not possible to obtain a stable and converged configuration in one iteration. The general methodology followed during the conceptual design is described in Fig. 1.6 and was heavily inspired by [6] and [7].

As illustrated in the flow chart, the first step is to decide on a configuration: canard or tail, high wing or low wing, propellers or ducted fans. Then a first estimation of the mass is obtained as described in Section 5. Using the knowledge of that first mass, every component of the aircraft (fuselage, wing, tail, propulsion) can be sized. Once every component has been computed, a new total mass is calculated. If the difference between the previous mass and this new mass is small enough, stability and performances can be verified. Otherwise, the components of the aircraft must be recomputed using the last mass computed. This process must be repeated until convergence.

In the second part of the project, each component is studied with more care. Advanced tools like *Tranair* or *Siemens NX* are used to obtain more precise results for certain parts of the design. Advanced empirical correlations are also used to perform the drag and performance analysis.

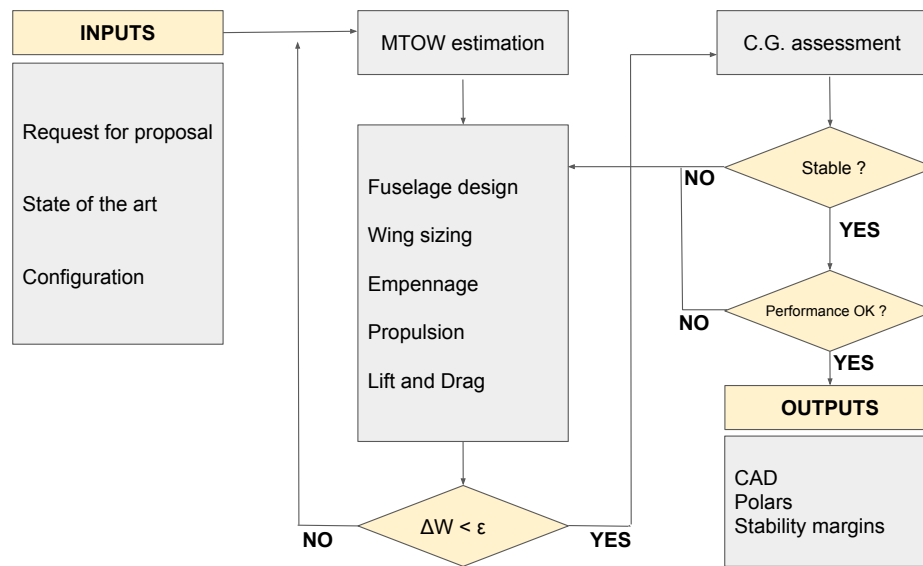


Figure 1.6: Schematic of the general methodology adopted for the conceptual design phase.

4 Design selection

The initial configuration is to be used as starting point to evaluate all the components. The choices made are justified hereunder:

Distributed electric propulsion

According to ONERA's study [8], the use of Distributed Electric Propulsion (DEP) has some potential especially in all-electric powered airplanes for civil transportation. This concept, which is compliant with the CS23 regulations, has been retained for its promising performances.

Wing & Canard

The wingless configuration was discarded as the energy consumption was considered to be too important. In addition, instead of a conventional tail and wing design, it was decided to use a canard and wing configuration. The canard configuration has the obvious advantage of placing the elevons in an undisturbed flow [7]. This makes the response of those control surfaces more predictable, which is a clear advantage as the aircraft is autonomous. Furthermore, in opposition to the lift of a tail which is oriented downwards, the canard lift is pointing upwards, counteracting gravity alongside with the wing. This results in lower wing loading and lower drag [7].

A high wing configuration was preferred over more traditional designs. One of the advantages of this configuration is that the access to the passenger cabin is not obstructed by the wing. Boarding and unboarding is consequently easier and faster. Moreover, high wings are also better in terms of stability. The geometrical parameters of the wing will be discussed in a later section.

Vectored Thrust

Among the different propulsion strategies, vectored thrust is preferred as it fully exploits the thrust contribution of each engine throughout the whole mission. The way this principle takes place in the Mistral Air Taxi is a compromise with the choice of a canard configuration; canard structure stiffness avoid distributed tilting propulsion to be placed along the span, so it's decided to fix engines directly on the fuselage at the canard roots.

Differential thrust

Traditionally, yaw control is achieved by installing a fin on the aircraft. Adding a fin would make the aircraft heavier and therefore reduce its efficiency. Moreover, it would require the fuselage to be longer to have a sufficient lever arm. It was decided here not to use a fin. Rather yaw control will be achieved through a differential thrust system.

Autonomous system

Machine learning and artificial intelligence in the oncoming years will reshape the way people travel. It will contribute to improve safety and security, reduce jams and time loss, thus improving resource management and time allocation, but not without risk, uncertainties or controversies. Equipping the aircraft with an autonomous system is mandatory [9] [10].

5 Weight estimation

5.1 First mass estimation

A first estimation of the total mass is obtained by studying similar concept of aircraft. The data used for this first estimation was found online through extensive research [11]. A summary can be found in Table 1.3.

Name	Number of passengers	Mass per passengers [lb]
Lilium jet	2	705.48
Transcend Air Vy 400	6	1,165
Hop Fly Ventury	4	447.54
Bartini flying car	4	606.27
XTI Aircraft Trifan 600	6	883.33
A ₃ Vahana	2	897.28
Initial design of an E-VTOL in [12]	2	1,106.72
Initial design of an E-VTOL in [12]	4	974.4

Table 1.3: Table of some of the aircraft considered for the first mass estimation.

The mass of each aircraft has been divided by the number of passengers in order to obtain comparable values. The 20 %

lowest values were removed and the remaining masses were averaged to calculate an average aircraft mass per passengers. Adding a safety margin of 10 %, it was eventually found that the initial starting mass was 3,307 lbs.

5.2 Subsequent mass estimations

The mass calculated in the previous section was used as a starting point for the design. During the following parts of the project, the mass of the different components were primarily estimated using the empirical formulas found in Raymer's book [7]. The mass of the wing was not calculated using the formulas from the previous source. Rather, it was computed using the formulas found in [13].

The total weight of the aircraft is simply obtained by summing the mass of the different parts. Table 1.4 presents a breakdown of the mass of all the subparts of the aircraft while Fig 1.7 provides a visual breakdown of the total mass. The maximum takeoff weight of the aircraft is found to be about 3,470 lb.

Weight breakdown [lb]	
Fuselage	295
Wing	268
Canard	125
Control systems	41
Landing gear	165
Autopilot	154
Engine rotation mechanism	54
Engines	291
Nacelles	77
Batteries	649
Electrical	180
Avionics	184
Furniture	136
Air-conditioning	50
Payload	800
Total	3,470

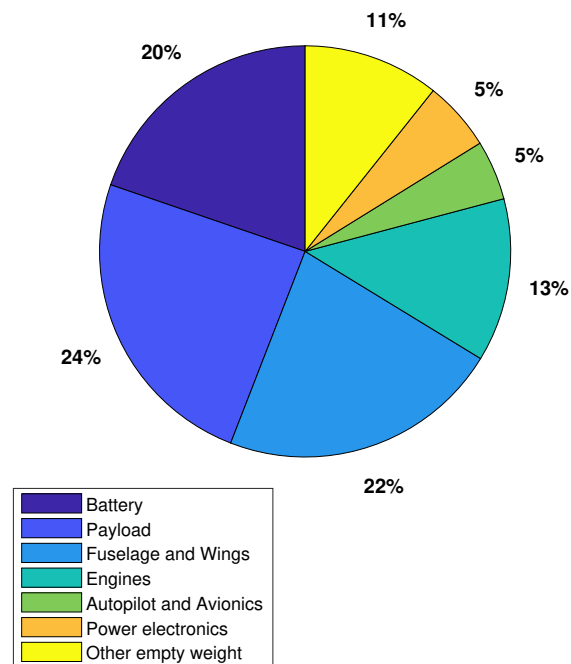


Figure 1.7: Percentage of gross weight.

Table 1.4: Complete weight breakdown.

6 CAD

The aim of the CAD is to give a realistic view of the aircraft and to check the integration of each subsystem. It is also useful to calculate a better approximation of the mass, the position of CG and the inertias of the aircraft.

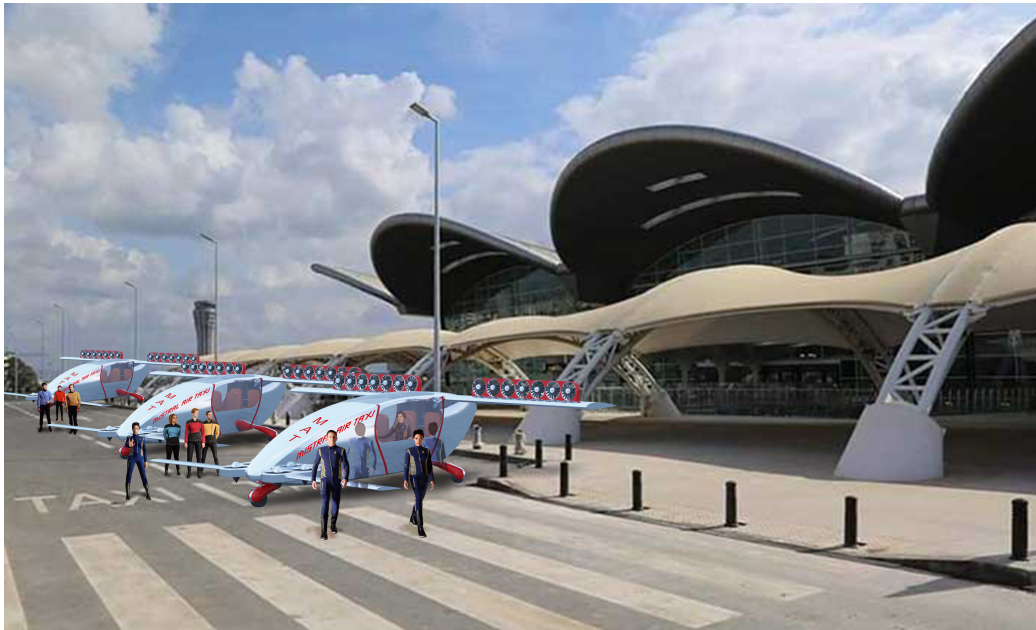


Figure 1.8: Realistic view of Mistral Air Taxis.

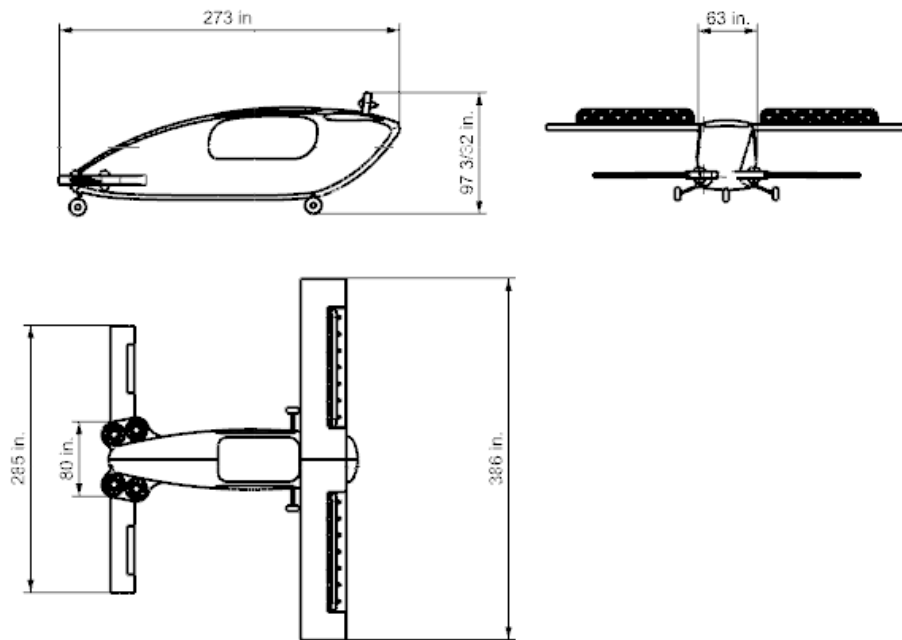


Figure 1.9: Side, front and top view of the Mistral Air Taxi.

The position of each subsystem is shown in Fig. 1.10 and 1.11 while the position of the center of gravity at its maximum take off weight is shown in the Fig. 1.12. The electrical systems are supposed to be distributed so they are not shown in these drawings.

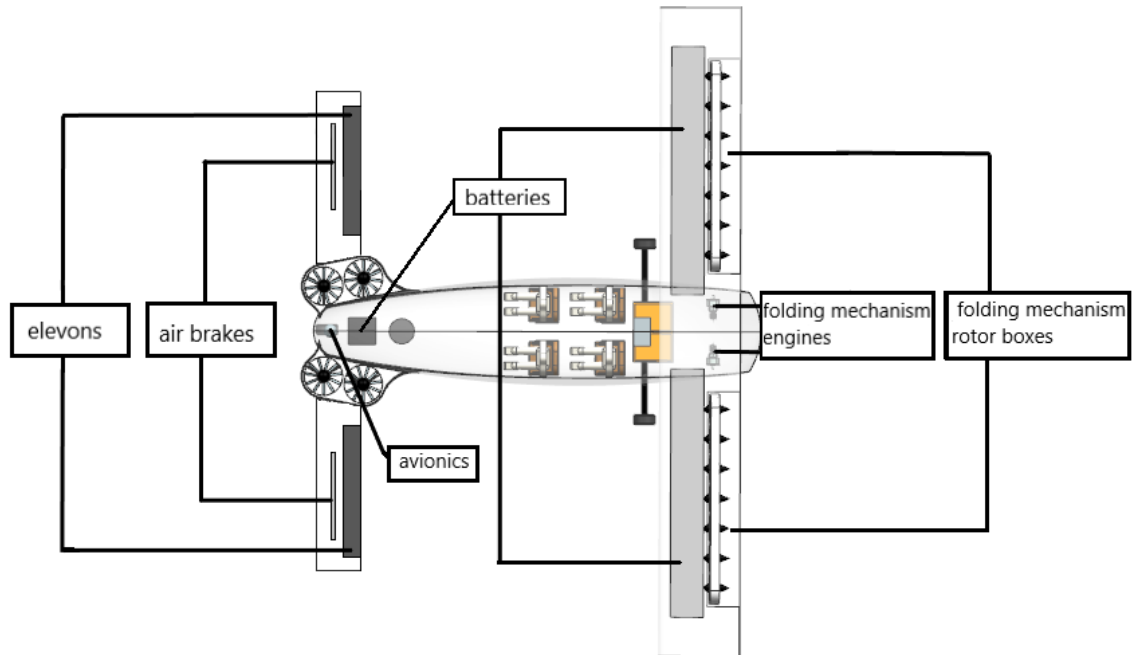


Figure 1.10: Top view

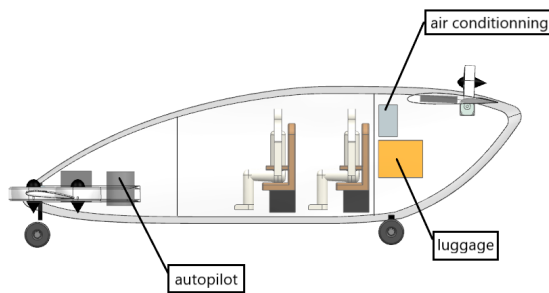


Figure 1.11: Lateral view

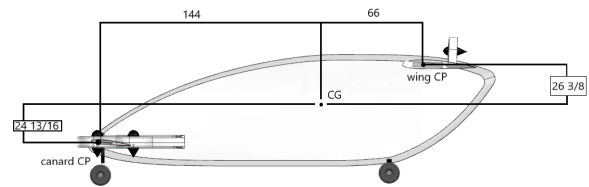


Figure 1.12: Position of CG (inches)

7 Components design

7.1 Fuselage

It could be argued that the fuselage is the key element of any aircraft as it will carry the useful loads. The design of the fuselage is therefore of the utmost importance. The dimensions of the main cabin must be chosen in order to offer maximum comfort to the passengers. Once the main cabin has been designed, the rest of the fuselage must be designed in order to accommodate the different required systems.

Main cabin design The main cabin design is of paramount importance in the overall design process. A balance between passenger comfort and performance must be found. A very large cabin would provide more comfort to the passengers but it would result in higher drag. Roskam [14] gives the size of the seats and aisles as a function of the travel class. In order to provide the best customer experience, it was decided to take the highest possible values. The proposed cabin design is presented in Fig. 1.13.

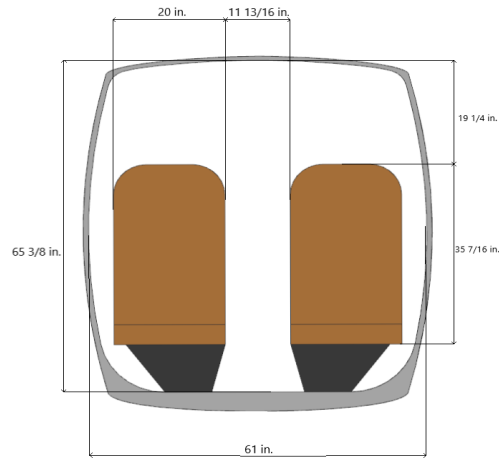


Figure 1.13: Proposed design for the main cabin.

Fuselage length Besides the main cabin, there are no other parts of the fuselage that must be accessible to passengers (since the flights will be very short, there are no lavatory and no galley). There must however be a luggage compartment at the rear of the aircraft and room to accommodate the auto-pilot and air-conditioning systems at the front of the fuselage. With those constraints in mind, the fuselage length was determined through successive stability analysis. The final design is presented in Fig. 1.14.

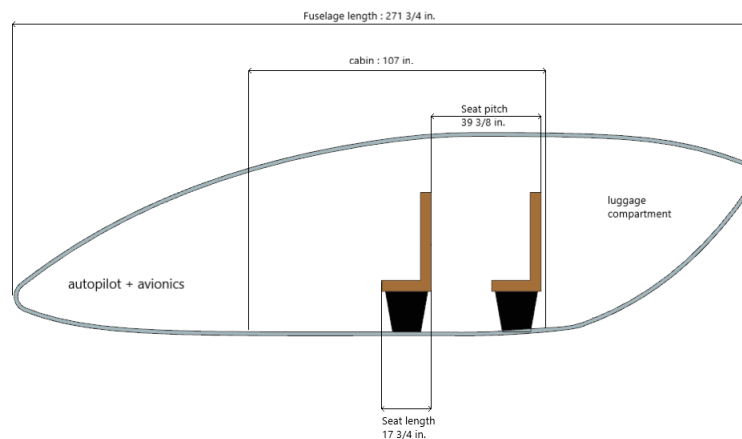


Figure 1.14: Side view of the fuselage showing the dimensions.



Figure 1.15: Cabin interior view.

7.2 Wing

The wing produces a large portion the required lift for the airplane to fly. As such, its design is a key step in the conception procedure of a new aircraft. The wing is firstly designed from an aerodynamic point of view using empirical formulas. Then, in the preliminary design, its aerodynamic properties will be reassessed with *Tranair* along with the loads acting on it, in order to properly design it from a structural point of view.

In order to be consistent throughout the design process, choices have been made. They are detailed hereunder.

- **Cruise Mach number:** the RFP states that the average cruising speed should be 150 mph. Flying at an altitude of 1,500 feet, it leads to a flight Mach number of 0.1979 .
- **Design lift coefficient:** using the simple relationship linking the lift coefficient and the drag coefficient:

$$C_D = C_{D,0} + \frac{C_L^2}{e\pi AR} \quad (1.1)$$

it could be shown that the optimal lift coefficient for the wing is in the range [0.75 - 1]. However, using such a high lift coefficient would lead to a very high wing loading, which would result in a bigger and heavier structure. It was therefore decided here to favor a lower wing loading over optimal aerodynamic performances. The lift coefficient must then lie in the interval [0.3 - 0.45]. Based on the results presented in [6], conservative values were chosen for e and $C_{D,0}$: $e = 0.75$ and $C_{D,0} = 0.03$.

- **Airfoil selection:** as mentioned previously, the flight Mach number is subsonic. This means that simple 4-digits

NACA profile can be used. The design lift coefficient of the airfoil should match the flight lift coefficient to reduce the drag. The NACA 2412 was selected. This airfoil has a thickness ratio of 12 and a max camber located at 40% of its chord. Its design lift coefficient is in the range [0.3 - 0.4] and therefore matches our chosen lift coefficient.

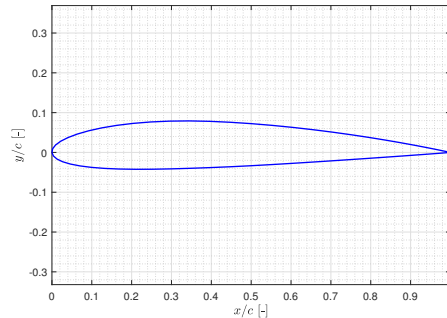


Figure 1.16: Wing airfoil NACA2412.

- **Aspect ratio:** The aspect ratio is defined as follows:

$$AR = \frac{b^2}{S_w} \quad (1.2)$$

In [7], the recommended aspect ratio for general aviation aircraft is around 7.6 - 7.8, depending on the number of engines. It was decided to round up this value to 8 for this aircraft.

- **Taper:** in this case, a tapered wing is not required because although tapered wings usually have lower drag, they are harder to manufacture.

Using the same method as in Section 14 to determine the cost, it appears that only the tooling costs are influenced by the fact that the wing is tapered or not. Using the method described in the aforementioned section, the additional tooling cost associated with tapered wings is estimated to be 5,000,000 \$.

Moreover, using the method described in Section 8, the drag for different tapers is evaluated. In the end, the drag for an ideal taper value ($\lambda = 0.45$ according to [7]) is found to be 98 % of the drag of an untapered wing. This has virtually no effects on the weight of the battery, the range or the performance of the aircraft.

In this case, the benefit of lower drag was considered to be too reduced to be profitable. Easier and cheaper manufacturing were preferred to aerodynamic performances.

- **Other geometric parameters:** in order to keep the wing as simple as possible, it was decided that the twist angle would be zero and that there would not be a dihedral.

Methodology The first step when designing a wing is to compute its 3D lift coefficient. Its slope can be computed from the airfoil lift slope (computed using *Xfoil*) using the following formula [15]:

$$C_{L,\alpha} = 0.995 \frac{c_{l,\alpha}}{E_J + \frac{c_{l,\alpha}}{\pi AR}} \quad (1.3)$$

where $E_J = 1 + \frac{2\lambda}{AR(1+\lambda)}$ is Jone's correction. The 3D lift coefficient obtained using this formula is shown as a function of the angle of attack in Fig. 1.17.

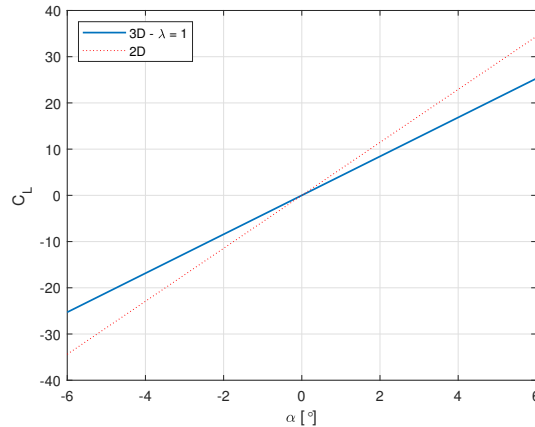


Figure 1.17: Comparison of the 3D lift coefficient and the 2D lift coefficient.

Through successive stability analysis, it was determined that the wing would sustain 63 % of the lift (and therefore, the canard 37%). Then assuming that in cruise the lift of the wing must equal 63 % of the weight, we can write:

$$L = 0.63W = \frac{1}{2}V^2 C_L \rho S_w. \quad (1.4)$$

The methodology consists here in setting the surface area of the wing and then computing the required incidence angle in order to obtain the required C_L to produce enough lift. This is an iterative process as the values of C_L and S_w have impact on stability and on the flight envelope.

Once the surface area has been fixed, the other parameters of the wing can be computed using, among others, the definition of the aspect ratio.

Results The final wing features are presented in table 1.5.

Wing	
S_w [ft ²]	129.67
b_w [ft]	29.53
c_w [ft]	3.28
i_w [°]	2.18
C_L [-]	0.3255

Table 1.5: Features of the wing.

7.3 Canard

This section shows how the canard is designed. As it was previously mentioned in Section 4, the choice of a canard is especially motivated by its important contribution to the lift.

Canard Firstly, a wing must be chosen for the canard. The goal is to produce high lift at low angles of attack. Ideally, the stall must occur at a relatively small angle of attack. Indeed, for stability reasons, a small stall angle is required to ensure that the canard stalls before the wing. From these constraints, the NACA 6412 (see Fig. 1.18) was selected, as it fulfills the aforementioned criteria.

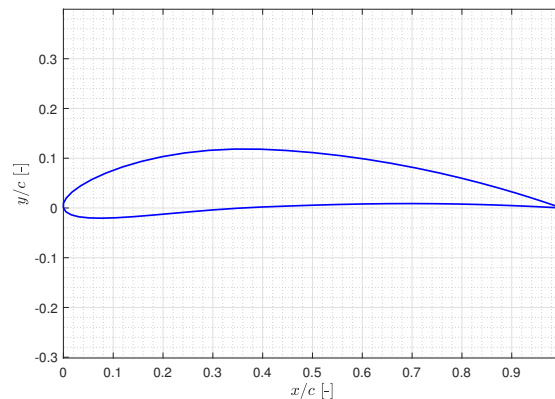


Figure 1.18: Canard airfoil NACA6412.

The 3D lift coefficient is computed using to the formula:

$$C_L = a(\alpha_{root} - \alpha_{L_0,root}) \quad (1.5)$$

where α_{root} is the angle of attack at the root and $\alpha_{L_0,root}$ is the angle of attack at the root at for a zero lift coefficient. The coefficient a is the slope of the 3D lift which is computed using Eq.1.3.

As the division of the lift is 33% for the canard and 67% for the wing, the lift required by the canard is not negligible.

The amount of lift produced by the canard depends on the angle of attack. Moreover it is mandatory to keep a certain margin of maneuver before the stall due to a too high angle of attack. Because of these very important constraints, the angle of incidence chosen is 3.5° .

As the canard must account for 37% of the total lift required to fly the aircraft, its dimensions can be determined using the formulas below:

$$L = 0.37W = \frac{1}{2}\rho V^2 C_L S_c \quad (1.6)$$

$$S_c = \frac{L}{\frac{1}{2}\rho V^2 C_L} \quad b_c = \sqrt{AR_c \times S} \quad c = \frac{b_c}{AR_c} \quad (1.7)$$

Finally, the dimensions obtained for the canard are summarized in Table 1.6. Taper, sweep and aspect ratio are the same as for the wing.

Canard	
S_c [ft ²]	36.75
b_c [ft]	17.15
AR_c [-]	8
c_b [ft]	2.14
C_{L_c} [-]	0.76
i_c [°]	3.5

Table 1.6: Summary of the main parameters of the canard.

7.4 Control surfaces

The control surfaces are of utmost importance, they play the principal role in maneuverability. The presence of a big number of engines on the wing makes the choice of control surfaces more difficult as it will be explained.

Elevons Elevons are used to control both the pitch and the roll of an airplane. This component is a combination of an aileron (roll control) and an elevator (pitch control). The design is based on FAA requirements (which provides maximum values for pitching and rolling rates) and on statistical data [14]. To work as elevators, the elevons must be deflected in the same direction. When they are used for roll control, as ailerons, they must deflect in opposite sense.

Because of the small space available on the wing it would have been impossible to design efficient ailerons. Furthermore, it would have been impossible to place elevons on the wing behind the engines. Indeed, in the wake of the engine, the flow is very disturbed rendering the response of the elevons very unpredictable. It was therefore decided to place the elevons on the canard [14].

The maximum deflection angle is set at 30° , which is a typical value for GA aircraft [7]. When they are deflected, a

moment around the center of gravity is created and the aircraft moves accordingly. The design is presented in Fig. 1.19 and the dimensions are summarized in Table 1.7.

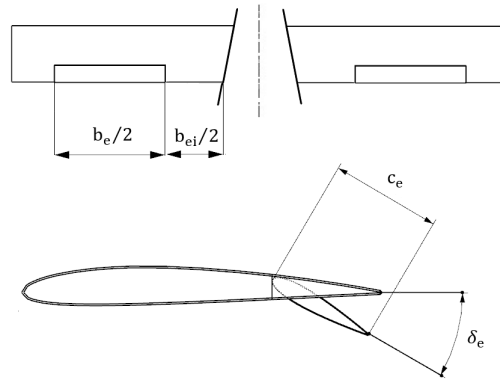


Figure 1.19: Top and lateral views of the elevons.

Elevons	
S_e [ft ²]	1.71
b_e [ft]	8.53
c_e [ft]	0.2
δ_e [°]	30
b_{ei} [ft]	1

Table 1.7: Characteristics of the elevons.

7.5 Propulsion & energy systems

Engine selection

In order to meet the strict requirements in terms of safety and cost-effectiveness described in the RFP, a distributed electric propulsion is preferred. Conservative choices about electric motors trends are made to fit the 2028 EIS. Particularly, the selected engines need to anticipate future FAA certification criteria and provide reasonable performance. The electric engines chosen for this aircraft are composed of two main parts: the electric motor and the ducted fan.

The mission presented in Fig. 1.5, has been divided into multiple segments in order to evaluate their respective power requirements. The only important consideration for the engine design is the maximum power (function of the rotation speed and torque) needed to generate the required thrust.

Number of engines The thrust-to-weight ratios of the engines on the wing and on the canard are 0.63 and 0.37 respectively. These values are imposed by the positioning of the different elements of the aircraft and the static stability analysis. The total amount of thrust generated by the engines on the wing and canard should respect the fixed ratios.

The number of engines strongly depends on the quality and type of electric motor and on the design of the propeller that should be optimized. Several configurations have been tested: this is, number of engines, type of electric motor (maximal torque generated, maximal rotation velocity, power required) and propeller (number of blades, airfoil, twist angle). The final configuration is characterized by four engines placed on the canard and 14 on the wing.

The reduced available space at the nose of the aircraft reduces the number of engines that could be placed. As a result, it was decided that 4 engines would be placed at the front of the aircraft. This ensure a fail-safe mode as the aircraft could still perform emergency maneuver if one of the canard engine was nonoperational.

As far as the number of engines on the wing is concerned, the compromise between the available space along the wingspan and the number of engines leads to placing 14 engines on the wing. In this case the emergency landing manoeuvre can be performed with only twelve operational engines on the wing.

Ducted fan Ducted fans for aircraft are mainly chosen because they offer higher power loading than open rotors of the same radius [16]. The presence of the duct results in an additional thrust. Consequently, the thrust produced by a ducted fan will be greater than open rotors operating at the same power. A last benefit of placing a duct around the propeller is the reduction of noise.

In the first place, the performances of hovering and cruise have been evaluated using disk actuator theory adapted for ducted fans [17][18][19][20]. The power required per engine to generate a certain amount of thrust is given by

$$P = \frac{1}{\eta} \frac{T^{3/2}}{\sqrt{4\sigma\rho A}} \quad (1.8)$$

where A is the disk actuator area of the ducted fan, $T = T_{fan} + T_{duct}$ is the thrust generated by the fan and the duct, η the engine efficiency, $\rho = 1.225 \text{ kg/m}^3$ the sea level air density and $\sigma = 1$ is the duct expansion ratio (i.e. ratio of exit area to disk area). The duct becomes more efficient as the expansion ratio increases above 1 (compared to 0.5 for an open rotor), but to avoid complex shape design, σ is kept to 1. The thrust T that each engine should generate is obtained by dividing the required forces to be stable by the number of engines. This is, each engine on the canard should generate a thrust equal to $\frac{0.37 \cdot \text{MGTOW}}{\text{Number of canard engines}}$, and similarly for the engines on the wing. This simple assumption is enough for the take-off segment.

The theoretical results are used as a starting point for further analysis based on the blade element theory. Using a modified version of the BEM code [21], the effect of the different propeller parameters such as diameter, airfoil, twist angle and rotation velocity on the thrust and the torque is studied. The BEM code does not take into account the presence of the duct neither the tip losses, such that it can be supposed that tip losses are compensated by the positive effect of the duct.

In Table 1.8, a summary of the different design parameters for both the wing's and canard's propellers is presented.

	Wing propeller	Canard propeller
Diameter [in]	15.75	21.65
Number of blades [-]	16	11
Chord [in]	1.181	1.378
Collective pitch [°]		5
Root twist [°]		32
Tip twist [°]		8
Root cutout [in]	0.984	1.969
Disk Loading [lbf/ft ²]	195.75	187.4

Table 1.8: Global propellers characteristics.

Taper was not considered for the sake of simplicity. A twist distribution is taken along the span of the blade in order to homogenize lift distribution. The aerodynamic profile used for the blades of both wing's and canard's propellers is the NACA8412. This cambered airfoil is the most convenient to generate the needed thrust. Indeed, it has a great aerodynamic (drag-to-lift ratio = 0.1523) and aeroacoustic performance [22]. Moreover, the number of blades is set such that the flow is not blocked by the superposition of blades. The span of the blades is limited by geometric considerations and thrust requirements.

Due to the different requirements for the canard's and wing's propellers, two separated studies have been performed in parallel. The first one is dedicated to establish the right amount of thrust needed by the canard for take-off and transition. Particular attention is paid to ensure that the torque and power required by the propeller do not overpass the limits of the chosen electric motor. As far as the wing propeller is concerned, the design is more restricted; many parameters are involved and a good balance between size, number of engines and number of propeller for each engine must be found. This step is an iterative process that has been carried out in accordance with stability and structural constrains.

Electric motor The choice of the motors is based on performance criteria and propeller requirements to generate the needed thrust. A particular attention is paid to working parameters such as RPM, power and torque. However, other secondary parameters such as long lifespan, low maintenance and high efficiency are also important.

DC motors are privileged since they are lighter than AC engines and mass reduction is a mandatory objective for the design of an aircraft, and even more important for an E-VTOL. Among the numerous existing types of DC motors, brushless DC motor (BLDC) are the most suitable for the design objectives described in [23]. The detailed comparison of some DC motors presented in Table 1.9 highlights their intrinsic characteristics as their high power-to-weight ratios combined with high RPM range and a good provided torque level. As both BLDC and AC engines need additional elements to operate, a medium voltage controller for the first and an AC-DC converter for the latter, BLDC remains the best choice in terms of weight saving.

Type	Motor	Total mass [lb]	Power-to-weight ratio [hp/lb]	Max. speed [RPM]	Torque [lb·ft]
BLDC	MP154120	13.23	4.05	9,600	55.32
BLDC	MP202150	26.46	4.05	9,000	110.63
SMPM	HAWK60	28.44	2.59	7,200	88.51
SMPM	EVM-42/30	30.86	0.48	12,000	22.86
SMPM	EMRAX 188	15.43	4.87	6000	66.38
Yokeless Axial Flux PM Motor	Magnax AXF225	35.27	7.30	14,000	184.39

Table 1.9: Comparison between different electric motors.

It must be noted that, for optimization reasons, two different engines are used since the power requirements are different, Figure 1.20. It's worth noticing that the maximal engine power is determined by the security margin required for fail-safe maneuvers which introduces a necessary oversize of the engines and battery. The characteristics of the motors on the canard and wing are detailed in Table 1.10.

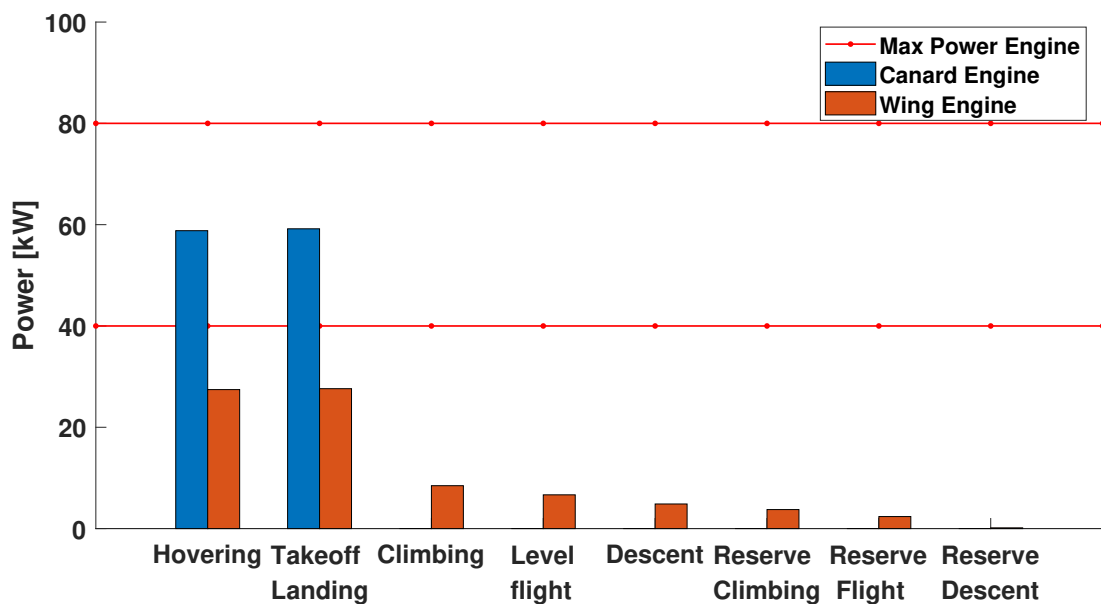


Figure 1.20: Engines power for sizing mission.

	Wing motor	Canard motor
Power [hp]	53.6	107.3
Size [in]	6.06 × 4.53	7.95 × 5.9
Total Mass [lb]	13.23	26.46
Max. speed [RPM]	10,000	9,000
Torque [lb·ft]	55.32	110.63
Max. VOLT. [V]	120	300
Max. AMP. [A]	500	650
Efficiency [%]		88
Power-to-weight ratio [hp/lb]		4.05
Takeoff requirements		
Speed [RPM]	8,850	8,150
Torque [lb·ft]	22.1	51.41
Power [hp]	37.04	79.36
Cruise requirements		
Speed [RPM]	6,650	N/A
Torque [lb·ft]	7.25	N/A
Power [hp]	8.93	N/A

Table 1.10: Electric motors characteristics and operating points for takeoff and cruise.

7.6 Electronic system

Battery selection

The difficulty for the battery selection is to forecast their properties in 2028. In this selection two principles are followed, battery trends and nowadays market for electric vehicles. Lithium-based batteries are the most suitable for an E-VTOL application in terms of specific energy, lifetime, and others advantages promoted by a majority of studies ([24] to [28]). Furthermore, their prices remain attractive compared to other type batteries and may still decrease in the next few years according to Blomberg New Energy Finance [29].

An increase of the energy density up to 400 Wh/kg is expected thanks to more advanced battery technologies [28]. Moreover, potential progress in Li-polymer may achieve a value for the energy density of around 650 Wh/kg [30]. Fig. A.3 and A.4 in Appendix show the trends concerning the volumetric energy density and power density battery packs for the automotive industry. For 2028, an optimistic assumption for the volumetric energy density is 700 Wh/L.

For reasons evoked in the next section, Placement & installation, the batteries are divided into three packs: one for

canard's engines and two for the wing's engines, Fig. 1.22 and 1.24. To meet the RFP requirement concerning the energy density B_{dens} for each pack and evaluate its weight M_{pack} , the system of equations 1.9 must be verified.

$$\begin{cases} B_{dens} = 450 \text{ Wh/kg} - P_{peak} \times 85 \text{ s} \\ B_{dens} = \frac{E_{mission}}{M_{pack}} \end{cases} \quad (1.9)$$

where $P_{peak} = \frac{P_{TOR}}{M_{pack}}$, is the specific peak power of the pack with P_{TOR} the power required by the engines on the canard or the wing. $E_{mission}$ is the energy needed by engines for their operations throughout the entire mission.

By solving Eqs. 1.9, the energy density for the two batteries connected to the engines on the wing is 398 Wh/kg. For the battery pack used for the canard engines, its energy density is 138 Wh/kg. Those values are respectively obtained by considering a peak specific power of approximately 2,217 W/kg and 13,333 W/kg. Table 1.11 summarizes the characteristics concerning the batteries.

A reasonable battery efficiency value of around 96% is chosen based on the studies cited above. Moreover, a safety factor is taken over the total storage energy to guarantee battery health by taking an additional 10% of its energy capacity.

	Wing's battery pack	Canard's battery pack	Total
Energy density [Wh/kg]	398	138	N/A
Volumetric density [Wh/L]		700	N/A
Power Density [W/kg]	2,217	13,333	N/A
Efficiency [%]	96	96	N/A
Total mass [lbs]	243.6	52.91	540.13
Total volume [ft ³]	7.06	4.24	18.36

Table 1.11: Characteristics of the batteries. The total stands for 2 wing's battery pack and 1 canard's battery pack

The aircraft has been designed to fly 62 sm (sizing mission plus a reserve for a diversion of 2 sm). In opposition to traditional aircraft, the weight do not decrease during the flight since no fuel is burned and the weight of the battery remains constant. Only the weight at takeoff influences the distance traveled, i.e. only the number of passengers will modify the payload range diagram, Fig. 1.21.

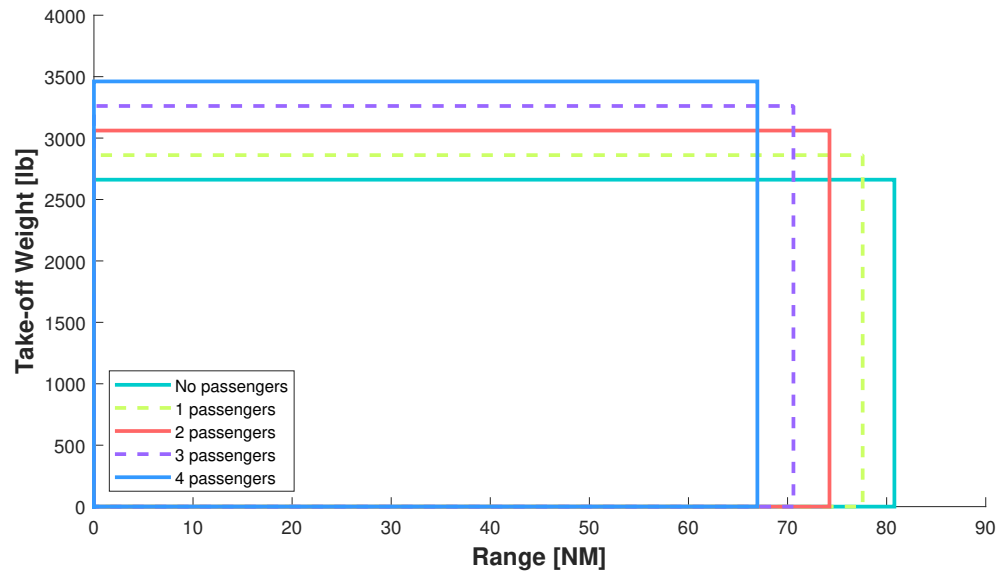


Figure 1.21: Payload range diagram.

Placement & installation

Engine positioning depends on stability, aerodynamics and structural issues and. The aerodynamic influence of the positioning of the engines should be analysed using computer fluid dynamics and wind tunnel tests in a further state of the development of the Mistral Air Taxi. Also, the structure containing the engines should be studied in detail with a special focus on the hovering and transition phases.

The engines on the canard are located close to the fuselage and not at the tips of the canard for structural reasons. Moreover, this position reduces the distance to the battery pack which is in the middle of the fuselage for stability reason and makes connections easier, Fig. 1.22.

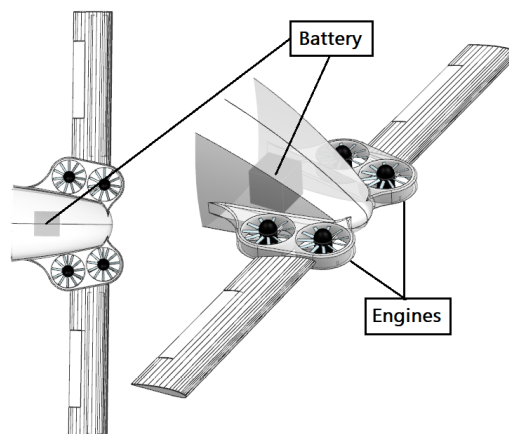


Figure 1.22: Propulsion system on the canard.

The engines on the wing (electric motor, propeller and duct) are assembled together and placed at the trailing edge of the wing. The structure, Fig. 1.24, is designed in order to reduce the drag related to the significant number of engines even

if some additional weight is introduced. The additional difficulty of those engines is in terms of structure.

In order to reduce the wing deflection in analogy with traditional aircraft and to shorten the cables for engines connection the batteries are assembled into the wing. Another important issue is related to the mechanism allowing the engines to tilt from the horizontal to the vertical configuration, as shown in Fig. 1.23, as it introduces significant stresses in the joints.

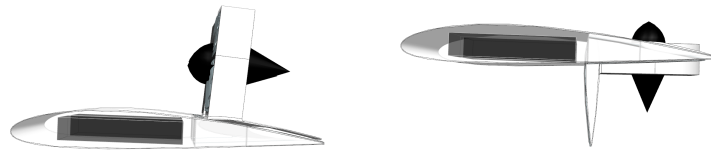


Figure 1.23: Flight (left) and take-off (right) configurations for wing engines.

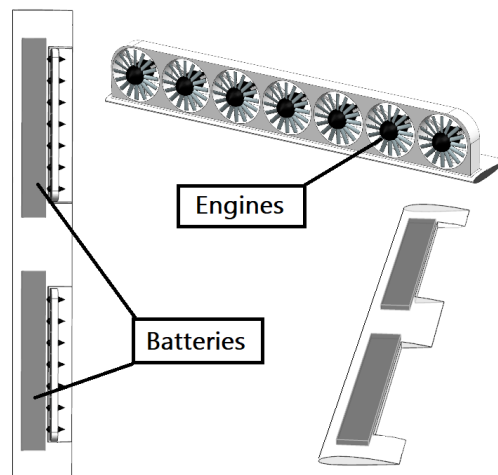


Figure 1.24: Views and locations for wing propulsion.

Transmission & control

To ensure the control of the aircraft in the safest way possible, inter-connectivity and redundancy principles are fundamental. In case of system failure the global architecture must be able to reroute the power to the operational engines and maintain the aircraft stable allowing landing maneuvers. A fine architecture design is necessary to reduce the weight propulsion equipment to optimize the redundancy factors. [31][32].

Concerning the controllers, they are placed between the batteries and the engines in order to avoid any additional cable weight. Cables and wires are thicker and heavier than for typical aircraft since they should transport high voltage (MV cables), but in this conceptual design state a standard weight is assumed for cables, Table 1.4. The power losses from controllers are negligible due to their high efficiency, most of them are more or less 0.99.

7.7 Landing gear

Landing Gear Form

For light vertical takeoff and landing aircraft, the landing gear can either be a skid or a wheeled landing gear. The skid landing gear is preferred for most helicopters, especially those lighter than 5 tons, because they are simple and have very light structures. However, because of the poor on-ground mobility capabilities, skid gears will not be considered as an option here.

Another option for VTOL aircraft is wheeled landing gear. This category includes tricycle landing gear, rear three-point landing gear, four-point landing gear, bicycle landing gear, etc. These have the significant advantage of allowing autonomous ground motion of the aircraft. Wheeled gears also allow for better shock absorbing properties, which is of paramount importance to guarantee a comfortable travel experience for passengers. In the context of this project, it was decided to use a tricycle landing gear. Moreover, the landing gear will be non-retractable to reduce the weight and the complexity of the system.

Landing Gear Placement

When determining the position of the landing gear, there are some basic requirements that must be met:

- The weight carried by the nose gear should not be more than 20% of the total weight, but it should not be less than 10% either;
- The angle between the vertical line of the main landing gear and the CG point should be between $16^\circ - 25^\circ$;
- For land-based aircraft, the overturn angle should be less than 63° . The overturn angle is a measure of the tendency of the aircraft to overturn when it taxis around a sharp corner.

Fig. 1.25 and 1.26 define the geometric parameters of the landing gear.

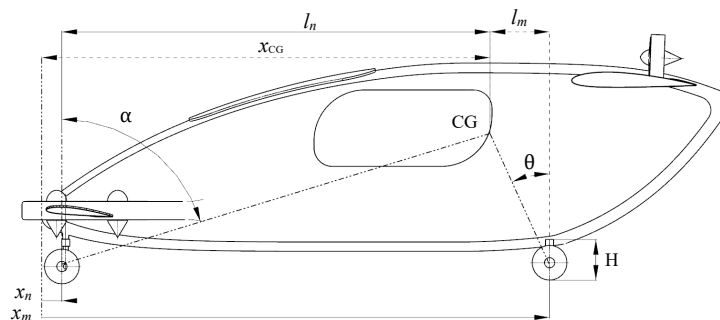


Figure 1.25: Landing gear geometric parameters.

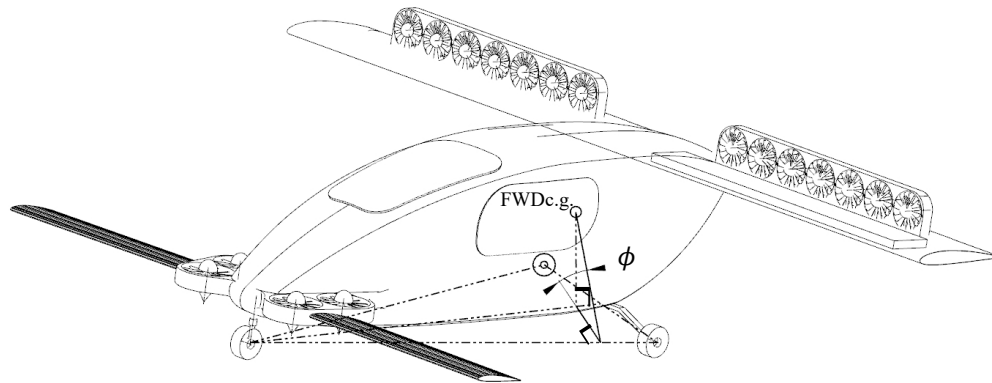


Figure 1.26: Landing gear geometric parameters.

CG Position [ft]	x_{ng} [ft]	x_{mg} [ft]	l_n [ft]	l_m [ft]	B [ft]	H [ft]	ϕ [°]	θ [°]	α [°]
14.37	0.78	16.17	13.68	1.8	8.14	1.15	55	20	70

Table 1.12: Landing gear Placement

The tire size can be determined by studying the maximum static load (which is obtained during vertical landing) and the required inflation pressure. As the aircraft will most likely always operate from runways/heliports made of concrete or asphalt, the maximum inflation pressure is 75 psi. The static load limits are presented in table 1.13. In that Table, the weight of the aircraft was multiplied by 1.25 in order to add a safety margin. Using this loading, the size of the tires can be computed. The results are presented in Table 1.14.

	W [lb]	Max $P_{m_{static}}$ [lb]	Max $P_{n_{static}}$ [lb]
2 Passenger	3,149.4	1,770.0	531.2
4 Passenger	3,549.4	1,994.8	598.6

Table 1.13: Landing gear loads.

	Main Gear	Nose Gear
Tire Type	Three Part Type	Type III
	13.5×6.0-4	5.00-4
Outer Diameter [in]	13.5	13.0
Width [in]	6.0	5.0
Rim Diameter [in]	4.0	4.0
Max load [lb]	3450	2500
Inflation Pressure [psi]	135	115
Static Loaded Radius [in]	5.35	5.2

Table 1.14: Tire selection and specifications.

The purpose of a shock absorber is to absorb any shocks (for instance at touchdown) in order to increase passenger comfort. For a general aviation (GA) aircraft, typical vertical speed at touchdown ranges from 10 to 20 ft/s, while for a vertical landing aircraft, these speeds are much smaller. In the case of the Mistral Air Taxi, the vertical speed is almost zero. Therefore, the required damping for an E-VTOL aircraft is much smaller than for GA aircraft. As a result, the damping that leaf springs can provide is enough, and can therefore be used for the landing gear. They have the advantages of simplicity and low weight, and they are also inexpensive, stout, durable, and relatively easy to mount on an airplane.

7.8 Autonomous system

Market justification The current level of automation in aviation, including drones, is comparable to level 3 as defined by the Society of Automotive Engineers (SAE)[33], and level 4 in certain unmanned military drones. Indeed, self-driving taxis are expected to land in the coming Tokyo 2020 Olympic Games. The major driving forces for an autonomous system are

- Aviation future: more aircraft in a finite airspace. Air traffic control will become a big challenge due to the diversity of flying objects: personal aircraft, air taxis, delivery drones, medical drones, etc. [34] [35].
- Human errors: in 2013, 32,179 fatalities and more than 2 million injured in crashes for the USA from Figure. More equipped vehicles (automatic braking, blind spot assist, proximity sensors, etc.) more than a third could be avoided. Indeed, 31% of the fatalities are due to alcohol abuse and other driver related errors [36] [37] [38]. Therefore, reducing the number of personal cars and promoting mobility-on-demand driven by autonomous system, those numbers will strongly decrease. Moreover, 80% of aircraft accidents are due to human errors and only 20% related to machine errors.
- Paradigm changer: those who are unable to drive (blind, disabled and even children) will obtain independence and reduce their social isolation [39].

Legislative issues Overall results of autonomous systems outweigh the possible disadvantages and costs at first sight, however deeper analysis is expected and accurate quantification has to be done as technology improves and autonomous system introduces in the society daily life. Very important regulatory issues and technology readiness (similar concept to Technology readiness level (TRL)) should taken into account by policy makers, agencies and public society, Fig. 1.27. Because even if the improvements are undeniable, unlikely catastrophic situations may occur.

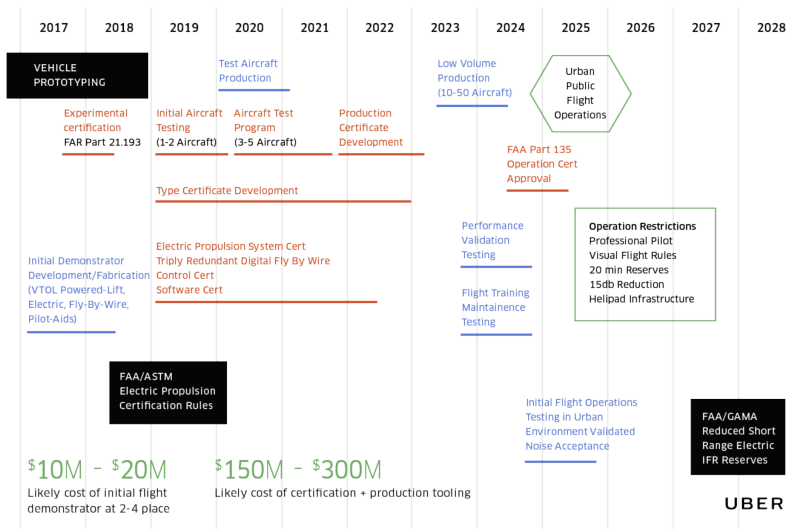


Figure 1.27: Certification and validation schedule proposed by Uber[40].

The conservative nature of aviation safety regulation is challenged with technologies which cannot be certified using the traditional safety standards for aircraft and ATM systems, thus representing an important barrier for new autonomous systems relying on adaptive software and machine learning algorithms (non-deterministic)[41][42][43].

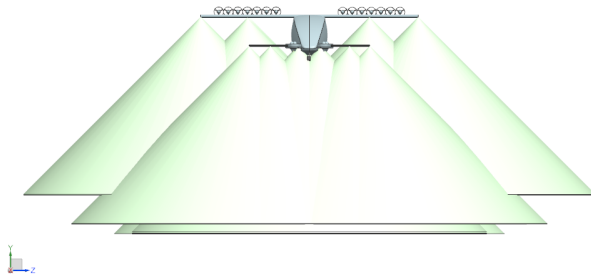
System architecture For a fully autonomous aircraft the sensors provide all the needed information about the environment and should cover the entire airspace around the aircraft. A detailed explanation of the avionics used by the autonomous system is given, focusing on the most important components and the redundancy to avoid major failures, or at least to provide fail-safe maneuvers such as emergency landings. The importance of the airspace management and how it will be implemented for fully autonomous flying objects is also discussed. In the appendix, Figure A.2, the number of sensors of each type is detailed with their cost.

System avionics The different type of sensors, [44], are summarized here:

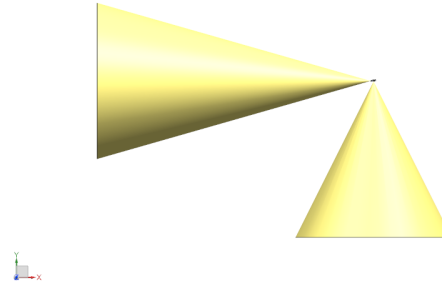
- **Sonar sensors:** allow short range information gathering and are used mainly for take-off and landing maneuvers. Located on landing gear, aircraft nose and rear part, at wingtips and under the aircraft. The coverage range is around 26ft.
- **Radar** is a crucial sensor used for measuring distances, altitudes, directions and velocities of both static and moving objects and also ground morphology. The coverage range goes up to 950ft. The distances for both, lidar and sonar

are such that the autonomous system has 5 seconds to react if it detects a problematic situation. Short range radars are also used to cover and provide redundancy and correction to the short range cameras.

- Scanning lidar are used to introduce redundancy, corrective sensing to the radar and provide a stereo vision for collision avoidance. The range coverage goes up to 1150ft [45].

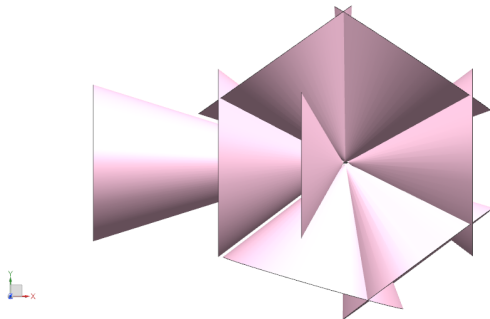


(a) Downward sonar coverage.

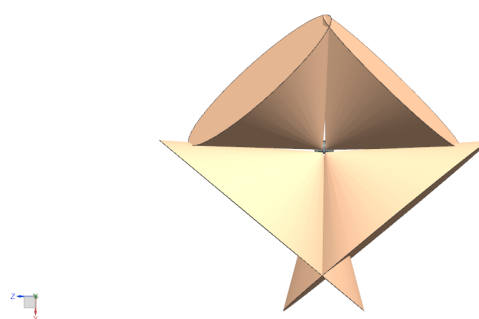


(b) Frontal and downward lidar and radar coverage.

- High quality cameras, and possible MSI or HSI (multispectral and hyperspectral imaging) systems. Several types of cameras can be used: long range cameras are used mainly in the front part allowing at least 5 seconds of reaction time. The short range cameras and wide-angle cameras covers the close surrounding airspace and work in parallel with the short range radars.



(a) Frontal, rear, upward and downward camera coverage.



(b) Short range lateral camera coverage.

- GPS and DGPS used to provide an accurate positioning of the aircraft and allow a better trajectory setting. Also important for the ATC station to manage the flying vehicles.
- Inertial navigation systems composed of accelerators, gyroscopes, etc to provide enough information on different parameters such as velocity, changes in direction, attitude, altitude, etc.
- Proximity sensors will allow the autonomous system to detect other flying objects, in a similar fashion to the automatic dependent surveillance broadcast system (ADS-B) being developed by NASA [45].
- Vehicle-to-vehicle communication to share instantaneous information between near-by flying objects that are close on direction, velocity, etc.

- Flow sensing probes such as Pitot tubes and pressure sensors.
- Other sensors to control batteries, engines, control surfaces, the cabin, etc.

The connection between the different components is achieved using a principal bus and for security issues some redundancy is added, allowing the information to follow another path in case of failure of the principal bus. Connections are made by wires, but for safety in case of major failure, each set of components is able to send data to the ground station independently.

Global organisation Firstly, before takeoff, the autonomous system proposes a flight plan to the public ATC and expect the clearance: this means that the flight plan is allocated to the aircraft and will avoid interference from other flying objects. Moreover, the aircraft relies on several sensors of paramount importance providing an accurate perception of the environment with a long range coverage. The gathered data will be processed by the on-board computer (GPU and CPU to process the gathered information) and control the aircraft while following the flight plan. Real-time information will be shared with the public ATC to manage the airspace in an optimal manner. In an ideal future, the air traffic control will also be autonomous. A major role is played by a the private ground station that will receive all the sensed data and have full control of the aircraft in case of failure of the autonomous system. Several degrees of failure can be imposed: From a fully autonomous ground based system to the exceptional intervention of a human operator[46] [47] [48] [43]. Additional arguments in favour of a public ATC is privacy, secrecy and rivalry that could exist between private companies.

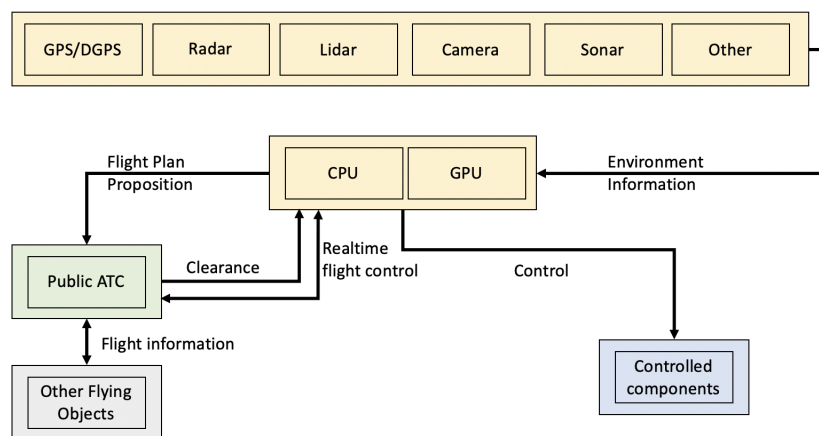


Figure 1.30: Autonomous system architecture. In yellow the aircraft, in green the public ATC and in grey the other flying objects.

Some basic operations that should be performed autonomously by the aircraft are summarized here [49]:

- Path planning: determining an optimal path for vehicle to follow while meeting mission objectives and constraints, such as obstacles or fuel requirements
- Trajectory generation (motion planning): determining control maneuvers to undertake in order to follow a given path or to go from one location to another[50].

- Trajectory regulation: constraining a vehicle within some tolerance to a trajectory
- Self-level: attitude stabilization on the pitch and roll axes.
- Altitude hold: The aircraft maintains its altitude using barometric or ground sensors.
- Hover/position hold: Keep level pitch and roll, stable yaw heading and altitude while maintaining position using GNSS or inertial sensors.
- Care-free: automatic roll and yaw control while moving horizontally
- Take-off and landing (using a variety of aircraft or ground-based sensors and systems: Autoland)
- Failsafe: automatic landing or return-to-home upon loss of control signal
- Return-to-home: Fly back to the point of takeoff (often gaining altitude first to avoid possible intervening obstructions such as trees or buildings).
- GPS waypoint navigation: Using GNSS to navigate to an intermediate location on a travel path.
- Orbit around an object or position: Similar to follow-me but continuously circle a target waiting orders from the ATC or ground station. (Fail-safe mode)
- Pre-programmed trajectories.

8 Aerodynamic study

Once the geometry of the aircraft is fixed, a more in-depth analysis than what was done at the design stage may be performed to increase the accuracy of the evaluation of the structural loads and the performance analysis.

In particular, the software *Tranair* is on the one hand used to compute the pressure distribution around the wing for the structural analysis (neglecting fuselage effect, but accounting for the canard) and on the other hand used to obtain more accurate wing and canard aerodynamic properties.

The drag of the full aircraft is assessed using an empirical method described by E. Torenbeek[51]. This method provides a complete drag breakdown by aircraft component and by drag type, allowing the latter to be compared with *Tranair*. The computed drag coefficients for the canard and the wing are then compared with those obtained from *Tranair*, and the most appropriate results are used for performance assessment.

8.1 Tranair

Tranair solves the full potential equation around arbitrary geometries. Its adaptative gridding capability offers a great flexibility regarding the geometry, as it is able to successively refine the grid based on local estimations of the error, as opposed to most modern (and more accurate) CFD tools that require manual meshing and refinement.

Tranair offers reasonably good accuracy for low computational cost, but must be used with care at high angles of attack, as it does not handle flow separation. It can be used for both inviscid and viscous cases, coupling the inviscid problem with the 2D boundary layer equations in the latter case. Computations with only the canard, only the wing and both together were run in order to evaluate the effect of the canard on the wing to proceed to an accurate stability and performance analysis.

Airplane lift curve and drag polar

The airplane lift and drag coefficients are reassessed at a Reynolds number $Re_{c_w} = 5.4 \times 10^6$ (which corresponds to the cruise velocity) at different angles of attack. These *Tranair* estimates are then interpolated to be compared to the airplane coefficients computed during the conceptual design using Eq.¹ 1.10 and 1.11:

$$C_{L_{\text{plane}}} = C_{L_w} + \frac{S_c}{S_w} C_{L_c} \quad (1.10)$$

$$C_{D_{\text{plane}}} = C_{D_{\text{plane},0}} + \frac{C_{L_w}^2}{e\pi AR_w} + \frac{C_{D_c}^2}{e\pi AR_c} \frac{S_c}{S_w}. \quad (1.11)$$

As can be seen in Fig. 1.31, both curves are almost superimposed and the slope of the *Tranair* lift curve is slightly smaller as it accounts for viscosity and for the effect of the canard on the wing. Since these results do not include the fuselage, the actual airplane lift coefficient will probably be even smaller, meaning that it will have to fly at a slightly higher angle of attack.

While empirical data provided a drag coefficient $C_{D_{\text{plane},0}}$ accounting for the profile drag of the whole aircraft, only the wing and the canard were modelled in *Tranair*, which leads to a significant gap between both polars, as shown in Fig. 1.32. However, both curves do show similar parabolic behaviour, as the (induced) drag essentially increases linearly with the square of the lift coefficient.

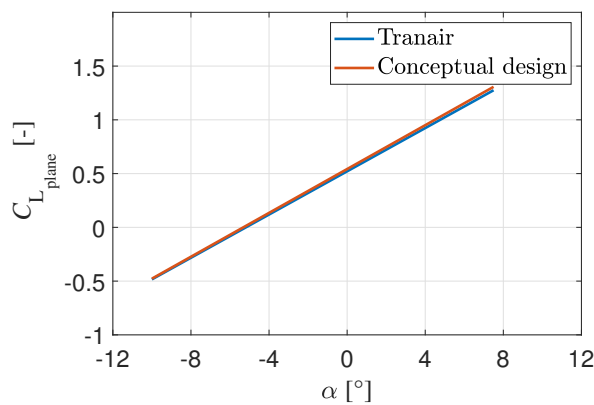


Figure 1.31: Airplane lift curve from *Tranair* and from the conceptual design.

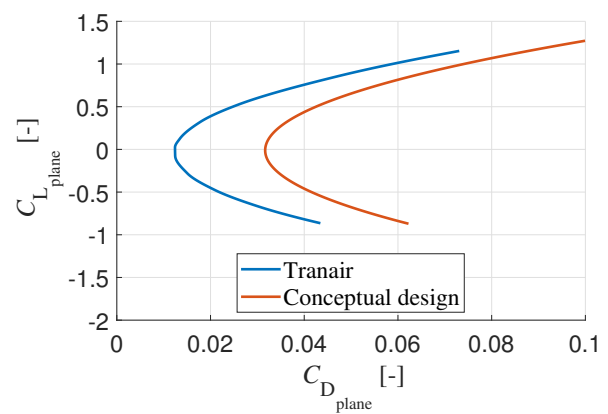


Figure 1.32: Airplane drag polar from *Tranair* and from the conceptual design.

¹Particular care must be taken when computing the airplane coefficients, as the wing and the canard do not have the same root angle with respect to the longitudinal axis of the fuselage.

Effect of the canard on the wing

As the air flows over the canard before passing over the wing, it is important to determine how the flow seen by the wing is affected. For this purpose, the section lift coefficient of the wing is extracted from two computations: one involving solely the wing, and one involving the wing and the canard, at cruise conditions. Both curves are depicted in Figure 1.33 and show that the canard induces a significant loss in wing lift.

Indeed, the canard, as it produces lift, also pushes the flow downwards, so that the flow seen by the wing is at lower incidence than it would have been in the absence of the canard, which is why less wing lift is produced between the two wingtip vortices of the canard. This lift loss can be computed by integrating the sectional lift coefficient along the span (for each curve):

$$2 \frac{c_w}{S_w} \int_0^{b/2} c_{l_w} dy = C_{L_w} \quad (1.12)$$

which gives a difference of $0.3510 - 0.2985 = 0.0525$, which is a seventh of the lift the wing would produce in the absence of canard. A faster way of proceeding to compute the "corrected" wing lift coefficient (*i.e.* accounting for the effect of the canard) is described below.

Assuming that the canard produces the same amount of lift independently of the presence of the wing, the "corrected" wing lift coefficient can also be computed from the difference between the canard and the airplane lift coefficients, if both are defined with respect to S_w . Doing so for different angles of attack provides a lift curve which is depicted in Figure 1.34, along with the wing lift curve in the absence of canard. The lift loss seems to increase with the angle of attack, which is expected since the higher the angle of attack, the stronger the wingtip vortices are. The earlier assumption made regarding the lift produced by the canard is also verified to be good, as the canard section lift coefficient drawn in Figure 1.35 is not significantly impacted by the presence of the wing downstream.

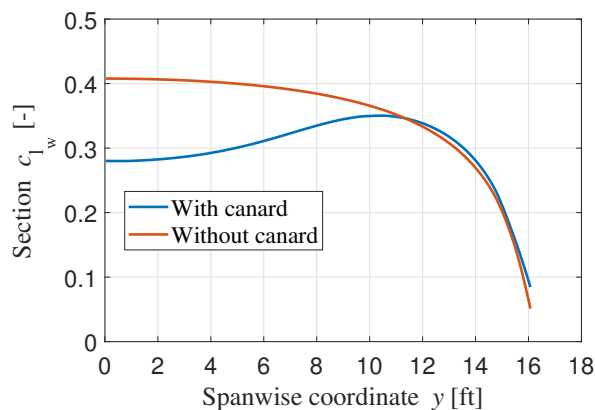


Figure 1.33: Section lift coefficient along the half-span of the wing, in cruise, with and without the effect of the canard.

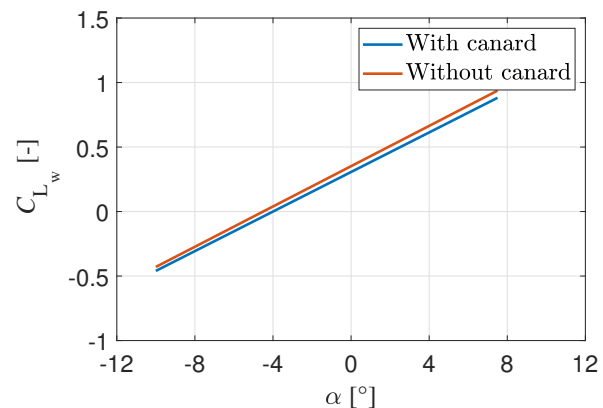


Figure 1.34: Wing lift curve with and without the canard.

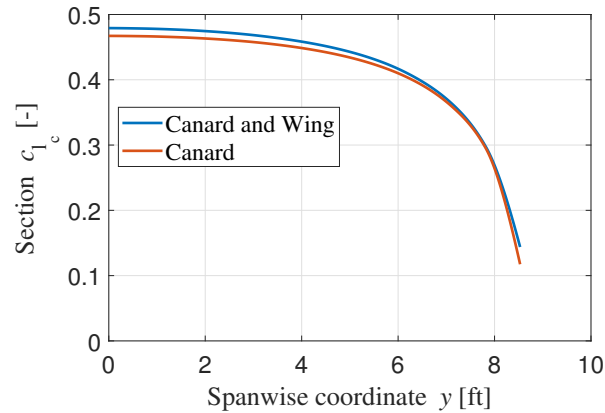


Figure 1.35: Section lift coefficient along the half-span of the canard, at cruise, with and without the effect of the wing. The reference chord is c_w .

Aerodynamic center of the wing

The aerodynamic center can be reassessed with *Tranair* to obtain more accurate results in the analytical study of the aircraft's structure, as it is where the wing loads will be applied.

Lateral position The lateral position can be directly computed from the wing section lift coefficient distribution shown above using Eq. 1.13:

$$y_{AC} = \frac{\int_0^{b/2} y c_{l_w} dy}{\int_0^{b/2} c_{l_w} dy}, \quad (1.13)$$

and therefore $y_{AC} = 7.79$ ft, which is slightly closer to the fuselage than the MAC.

Longitudinal position While it is usually assumed to be at the quarter chord, in subsonic cases, the real position of the aerodynamic center of a wing is often a little ahead of it. Indeed, if the moment coefficient derivative at the quarter chord and the lift coefficient derivative with respect to the angle of attack are known, the longitudinal position of the aerodynamic center (with respect to the leading edge) can be found using the following relationship:

$$x_{AC}/c_w = 0.25 - \frac{C_{M\alpha, c/4}}{C_{L\alpha}} = 0.2299$$

so that $x_{AC} = 11.08$ in.

8.2 Drag analysis.

In the following section, the total drag of the aircraft is computed by using the methodology of reference [51]. The different drag sources are the following:

Vortex induced drag The vortex induced drag, also known as lift-induced drag or simply induced drag, is the drag component generated by wingtip vortices. As these vortices tend to redirect the flow downwards, they also lower the

effective angle of attack seen by the wing, which in return reduce the lift and increase the drag produced by the wing.

Profile drag : The profile drag is the drag resulting from skin friction drag and from pressure drag (or form drag). The skin friction drag is directly related to the wetted area of the body, as it is directly due to the interaction between fluid particles and the skin of the body. Pressure drag mainly depends on flow velocity and on the longitudinal shape of the body.

Interference corrections : In reality, each component of the aircraft is not isolated which means components will interact with each other. Some corrections are thus made to better approximate the drag of the entire aircraft.

Protuberances, surfaces imperfections, etc: In order to complete the drag study, all external components have to be taken into account. Moreover, the aircraft is still at the preliminary design stage, which means the design is not completely defined. This leads to the use of empirical corrections and statistical data to estimate the drag of protuberances and imperfections.

Aircraft part	Drag coefficient
Wing	0.0126
Canard	0.0087
Fuselage	0.0168
Engine	0.0026
Landing gear	9.58×10^{-4}

Table 1.15: Contributions of drag component at cruise.

The pie chart of Fig. 1.36 shows the percentage of the total drag that each drag component is responsible for. Then Fig. 1.37 provides the impact of each type of drag cited above.

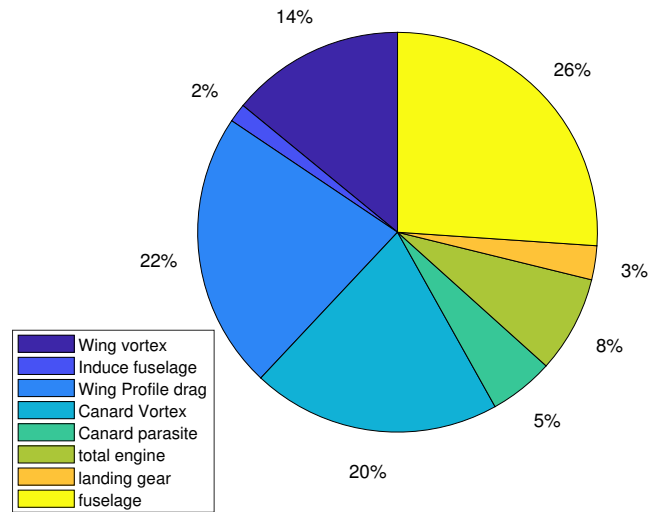


Figure 1.36: Division of the drag.

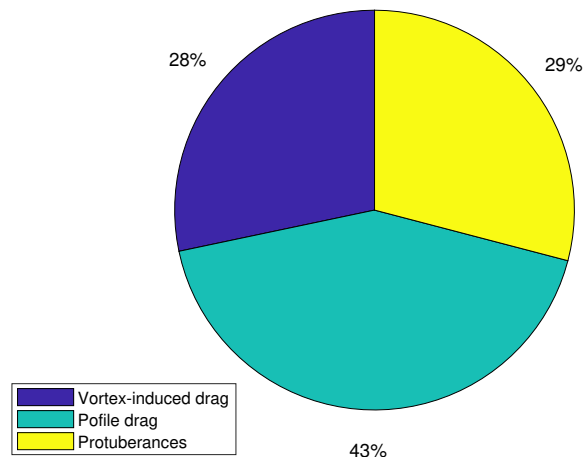


Figure 1.37: Division of the different type of drag.

The most important contribution to the total drag comes from the fuselage. It represents more than a quarter of the total drag of the aircraft. Then the total wing and canard contributions give together 61 % of the total. The landing gear and the total engine represent only 8% and less than 3% respectively. This differences between influences of these components is due to their surface. Indeed the drag is directly proportional to the surface thus it is logical that most of the drag comes from the fuselage. Afterwards Fig. 1.37 shows that the profile drag represents 43% of the total drag which the most important drag type. Indeed the protuberances and the induced-vortex drags represents 29% and 28% respectively and then are weaker but not negligible.

The total drag can be calculated using Eq. 1.14 and by applying a summation on all the components taken into account.

The result is equal to 225.26 lbf in cruise configuration that is to say at 150 mph.

$$D = \frac{1}{2} C_D \rho V_\infty^2 S \quad (1.14)$$

Drag polar Computing the total drag coefficient for different values of wing and canard lift coefficients. Using those provided by *Tranair* allows to take into account the loss of wing lift. The resulting empirical drag polar is shown in Fig. 1.38, along with the previously computed drag polars. As the empirical method includes all the aircraft components affecting the airflow, the drag coefficients obtained are *de facto* larger than those obtained with *Tranair*. They are however smaller than the values from the conceptual design which were expected to be overestimates.

One thing to notice is that the empirical polar is slightly shifted upwards compared to both other curves. Since both the canard and the wing generate a significant amount of lift, $C_{L_{\text{plane}}} = 0$ only implies that both components compensate each other and not that the drag is the lowest, as in the conceptual design estimation. Furthermore, for the empirical computation, the wing and canard profile drag also depend on their respective lift coefficients, and the fuselage induced drag is also impacted, resulting in the significant offset observed.

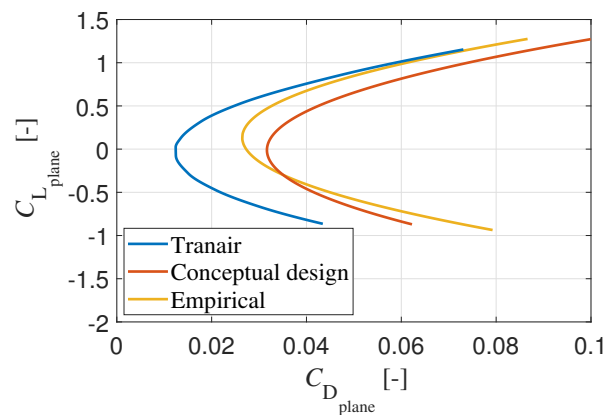


Figure 1.38: Airplane drag polars obtained from *Tranair* and from empirical methods (advanced and conceptual design).

Finally, the individual drag component estimates from *Tranair* and from the empirical method at cruise are listed in Table 1.16. The drag analysis values are all smaller than those from *Tranair*. In particular, due to the fuselage, the wetted area used to empirically compute the profile drag is not as large as the wetted area in *Tranair*², which is more impactful for the canard than for the wing as a larger proportion of the surface of the former is taken by the fuselage, resulting in a greater difference between the profile drag coefficients. There also is a noticeable difference between both wing induced drags, since the one from *Tranair* was computed without accounting for the canard effect, and the empirical one using the "corrected" lift curve, thus generating less induced drag.

²As the fuselage was not modelled in *Tranair*.

	Tranair	Drag analysis
Canard profile drag	0.0028	0.0018
Canard induced drag	0.0072	0.0069
Wing profile drag	0.0082	0.0078
Wing induced drag	0.0054	0.0038

Table 1.16: Drag coefficients in cruise conditions evaluated via *Tranair* and via empirical methods.

9 Structure design

The aircraft's structure is designed such that it is able to withstand the loads that it could encounter while flying inside its flight envelope.

The flight envelope is first studied to determine the loads that are applied on the aircraft under the most critical flight conditions. Using those loads, the structures of the fuselage and the wing are then designed using a simple analytical procedure. Finally, the finite element method is used to confirm the analytical analysis.

For the worst case scenario, only the section of the fuselage in front of the wing and the section of the wing at the root are considered for the analytical approach since they withstand the biggest loads. Therefore, if those sections are designed such that they can resist the loading, the rest of the structure will inevitably be structurally safe.

The mathematical procedure is substantially based on the theoretical developments presented in [52].

9.1 Flight Envelope

In the following section, every speed mentioned will be an equivalent airspeed, unless explicitly stated otherwise.

The placard diagram shown in Fig. 1.39 is drawn using a design cruise speed of 204 kts (TAS), which is the speed achieved at the design altitude, at maximum engine thrust and in level flight. The design diving speed V_D is fixed based on the greatest speed increase between $M = 0.05$ and a specific maneuver described by the FAA[53]. The mach is kept constant to obtain limit values of the velocity above the design altitude, and the drag is kept constant to obtain values below it. While the airplane is able to provide sufficient thrust for the aircraft to maintain cruise up to really high altitudes, since the cabin is unpressurized, it shall never exceed an altitude of 14,000 ft at which oxygen supplies would become mandatory. A more reasonable maximum operating altitude is then fixed at 8,000 ft, which is where altitude sickness typically starts to occurs.

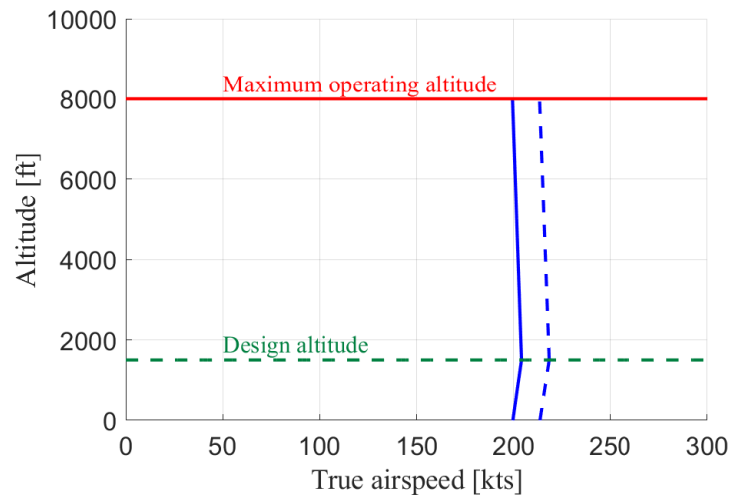


Figure 1.39: Design cruise (blue) and dive (dashed blue) velocities (TAS) as a function of the altitude.

The maneuver and gust envelopes of the Mistral Air Taxi are displayed in Fig. 1.40. They show the loads that can be reached by the aircraft at an altitude of 1500ft, with and without the effect of gusts, for the different flying velocities.

The envelopes are drawn using a $C_{L_{max,plane}}$ of 1.27 and $C_{L_{max,neg,plane}}$ of -0.87 , based on the stall angles of the canard computed using *Xfoil*. The upper and lower load factor bounds of the maneuver envelope are 3.8 and -1.8 . The light green dashed lines represent the load applied by vertical sinusoidal gusts (upwards and downwards) with gust equivalent velocities of 66, 50 and 25ft/s (respectively used for stall, cruise and dive), as a function of the equivalent airspeed of the aircraft.

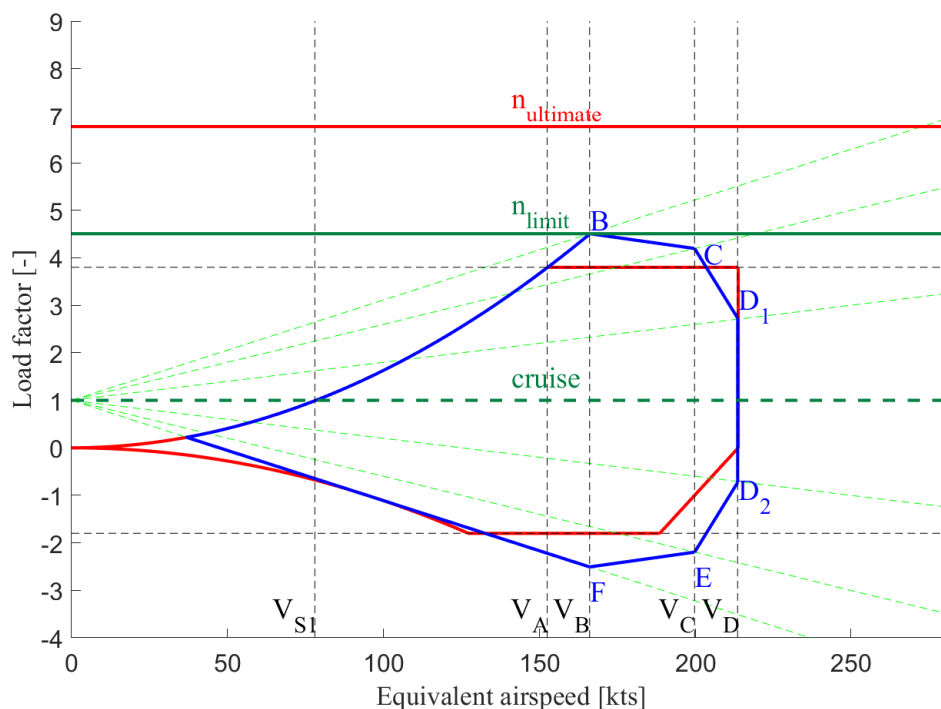


Figure 1.40: Maneuver (red) and gust (blue) envelopes of the Mistral Air Taxi.

The flight envelope gives the different critical flight conditions which may arise during the mission and should be withstood by the structure. It is then to the autopilot to never exceed these and fly inside the envelope. V_{S1} is the lowest speed at which the aircraft may achieve cruise and is known as the stall speed. In this case, V_{S1} is equal to 79 kts. V_A is the stall speed under maximum loading and is equal to 156 kts. It can be noted that the largest maneuver load factor the aircraft will undergo is lower than the strongest gust load, at the design speed V_B .

9.2 Loading

Aerodynamic loading

The aerodynamics loads are obtained by a simple equilibrium of vertical forces and moments around the center of gravity of the aircraft at the critical points of the flight envelope. The aircraft's structure should be able to overcome these loads, so that the most critical point will be the main design criterion. It must be noted that the critical point is not necessarily the same for wing and fuselage.

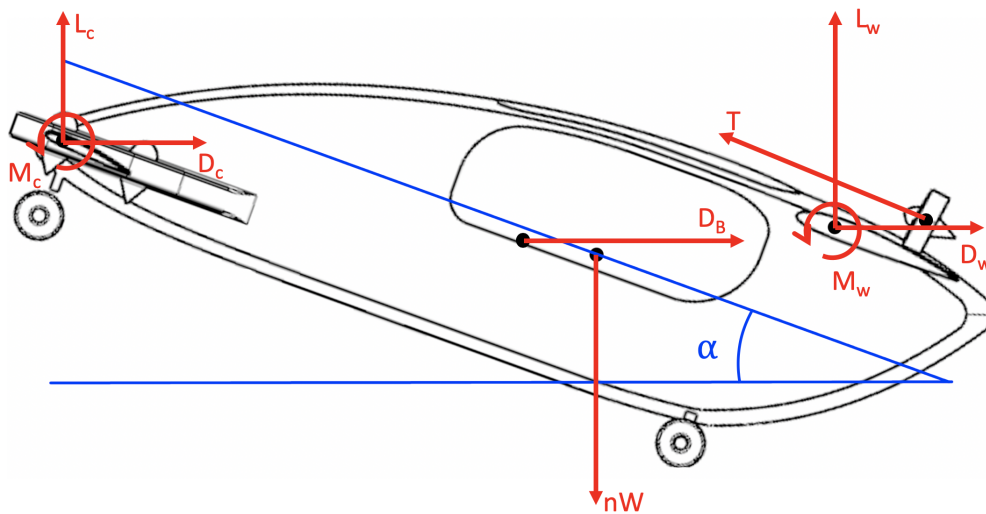


Figure 1.41: Schematics of the aerodynamic forces acting on the aircraft.

The E-VTOL will not be forced to react abruptly, the flight maneuvers are supposed to be smooth and do not introduce any potential additional loading. Nevertheless, to introduce a certain physical behaviour, the pitching acceleration is assumed to be equal to $\ddot{\theta} = \pi/6$, even though this value is difficult to validate at this stage of the project. Other phenomena such as side-slip induced loads are not only difficult to evaluate correctly but negligible since the side-slip angle will not be high and the aircraft has no fin. In the framework of a preliminary design, the lift and drag produced by the wing and the canard (L_w , D_w , L_c , D_c respectively), the thrust (T), the drag of the fuselage (D_B) and the fully loaded aircraft's weight (Wn where n is the load factor) are considered preponderant. Notice that the angle of attack of the aircraft and the incidence angle of the wing and canard should be taken into account.

Two different procedures are followed. At point B, the stall curve is intercepted, and thus the angle of stall is known, therefore, the unknown is the velocity. At the other points of the flight envelope, the velocity is known, however the angle

of attack is unknown. However, for both cases, the solved equilibrium equations are

$$\begin{aligned}
 L_w - \frac{1}{2} \rho_0 V_{eq}^2 S_w C_{L_w} (\alpha + i_w) &= 0 \\
 L_w + L_c + T \sin \alpha - nW &= 0 \\
 L_w \cdot l_{L_w} + D_w \cdot l_{D_w} + L_c \cdot l_{L_c} + D_c \cdot l_{D_c} + D_B \cdot l_{D_B} + T \cdot l_T + M_w + M_c - I\ddot{\theta} &= 0
 \end{aligned} \tag{1.15}$$

where the l_i are the distances from the application point of the force to the center of gravity. Notice that the body drag should be applied to the aerodynamic center of the fuselage, however here it is applied to the aerodynamic center of the wing projected on the symmetry plane of the aircraft, which is a reasonable approximation. The values for the mass, the inertia and geometry are obtained from the computer model of the aircraft.

The points of interest for structural analysis are listed in Table 1.17. They are the cases for which loads on the aircraft will be computed in order to determine the most critical conditions.

Point	B	C	D ₁	D ₂	E	F
Load factor [-]	4.31	3.87	2.54	-0.54	-1.9	-2.31
V_{eq} [kts]	168	199	213	213	199	168
α [°]	7.5	4.82	0.61	-5.41	-8.21	-10.28
L_w [lbf]	$2.496 \cdot 10^4$	$2.173 \cdot 10^4$	$1.365 \cdot 10^4$	$-0.302 \cdot 10^4$	$-0.946 \cdot 10^4$	$-1.097 \cdot 10^4$
L_c [lbf]	$-1.001 \cdot 10^4$	$-8.028 \cdot 10^3$	$-4.721 \cdot 10^3$	$1.132 \cdot 10^3$	$3.020 \cdot 10^3$	$3.112 \cdot 10^3$
M_w [lbf]	$-8.536 \cdot 10^3$	$-1.019 \cdot 10^4$	$-9.382 \cdot 10^3$	$-5.460 \cdot 10^3$	$-3.210 \cdot 10^3$	$-1.635 \cdot 10^3$
T [lbf]	$2.723 \cdot 10^3$	$2.1682 \cdot 10^3$	$1.8431 \cdot 10^3$	$1.8431 \cdot 10^3$	$2.1682 \cdot 10^3$	$2.7231 \cdot 10^3$

Table 1.17: Critical points of the flight envelope and aeronautical loads.

The other variables in Eq 1.15 are several orders of magnitude smaller than those in the table. Therefore the principal results are mainly affected by the values in the table. Nonetheless the calculations have been performed without neglecting any values.

Structural loads

From the previous results, the loads on the fuselage and wing are determined by solving the equilibrium equations as detailed below.

Fuselage section loading

For the fuselage, the reference frame used is such that the origin is at the center of gravity, the \mathbf{e}_x pointing towards the nose of the aircraft and \mathbf{e}_z downwards. These should be taken into account for the analytical study since two different reference frames are used.

Moreover, in addition to the aerodynamic forces to which the fuselage is subjected, some additional loads must be taken into account, namely the weight of the canard, engines, the packs of battery placed on the canard and the weight of the fuselage itself.

Taking into consideration all these parameters, which were estimated in different parts of the preliminary design, the expressions of the reaction forces and moments equilibrium become

$$\begin{aligned}
 T_x &= (n(W_{canard} + W_{eng} + W_{batt} + W_{fus}) - P) \sin \alpha \\
 T_z &= (n(W_{canard} + W_{eng} + W_{batt} + W_{fus}) - P) \cos \alpha \\
 M_y &= (n(x_{canard} \cdot W_{canard} + x_{eng} \cdot W_{eng} + x_{batt} \cdot W_{batt} + x_{fus} \cdot W_{fus}) - x_{CP} \cdot P) \cos \alpha
 \end{aligned} \tag{1.16}$$

Note that T_y and M_z are always zero because the aircraft under consideration has no fin. Moreover, since it does not have a tail neither, M_x will always be zero as well. The results can be found in Table 1.18.

Case	T_x [lbf]	T_y [lbf]	T_z [lbf]	M_x [lbf-ft]	M_y [lbf-ft]	M_z [lbf-ft]
B	$1.7251 \cdot 10^3$	0	$1.3104 \cdot 10^4$	0	$4.4820 \cdot 10^4$	0
C	$-1.5802 \cdot 10^3$	0	$-1.8757 \cdot 10^4$	0	$-5.9872 \cdot 10^4$	0
D ₁	-125.0166	0	$-1.1775 \cdot 10^4$	0	$-3.7554 \cdot 10^4$	0
D ₂	$-0.2437 \cdot 10^3$	0	$0.2576 \cdot 10^4$	0	$0.8203 \cdot 10^4$	0
E	$-1.1496 \cdot 10^3$	0	$0.7962 \cdot 10^4$	0	$2.5317 \cdot 10^4$	0
F	$-1.6457 \cdot 10^3$	0	$0.9076 \cdot 10^4$	0	$2.8786 \cdot 10^4$	0

Table 1.18: Structural loading on the fuselage for the critical points of the flight envelope.

As can be observed, the most critical case is point C. Therefore, the subsequent analysis will be based on this load case.

Wing root loading

For the wing, the reference frame is such that the origin is at the center of gravity of the wing, the \mathbf{e}_y is spanwise and the \mathbf{e}_x is pointing towards the leading edge.

The wings are subjected to three main loads: its weight (including batteries, engines, ...), the thrust and the aerodynamic forces. The different weights come from the different subsections of the conceptual and/or preliminary design and must be multiplied by the load factor (n). The thrust force is known from the propulsive study of the Mistral Air Taxi. The thrust is considered to be aligned with the fuselage's principal axis (here the angle of incidence of the wing is ignored). Finally, the aerodynamic forces are taken into account by applying the lift, drag and a moment at the aerodynamic center. The values for those forces and moment come from the previous analysis, and an estimation of the position of the aerodynamic center, were obtained using Tranair.

The structural loads at the wing root can then be computed using the following formulas

$$\begin{aligned}
 T_x &= \left(n.W_w - \frac{L_w}{2} \right) \sin(\alpha + i_w) - \frac{D_w}{2} \cos(\alpha + i_w) + \frac{T}{2} \\
 T_z &= \left(\frac{L_w}{2} - n.W_w \right) \cos(\alpha + i_w) + \frac{D_w}{2} \sin(\alpha + i_w) \\
 M_x &= \left(\frac{L_w}{2} \cos(\alpha + i_w) + \frac{D_w}{2} \sin(\alpha + i_w) \right) y_{AC} + n.W_w \cos(\alpha + i_w) y_{CG} \\
 M_z &= \left(-\frac{L_w}{2} \sin(\alpha + i_w) - \frac{D_w}{2} \cos(\alpha + i_w) \right) y_{AC} + n.W_w \sin(\alpha + i_w) y_{CG} + \frac{T}{2} y_T \\
 M_y &= \frac{M_w}{2} + \frac{T}{2} h_T
 \end{aligned} \tag{1.17}$$

where y_{AC} is the spanwise position of the aerodynamic center, y_{CG} is the spanwise position of the center of gravity of the half-wing, y_T is the point of application of the thrust force, h_T is half the diameter of the engine, T is the thrust force, L_w is the total lift of the wing, D_w is the drag of the wing and W_w is the weight of the half-wing (structure and batteries). The numerical results obtained for the different critical points of the flight envelope are given in table 1.19.

Case	T_x [lbf]	T_y [lbf]	T_z [lbf]	M_x [lbf·ft]	M_y [lbf·ft]	M_z [lbf·ft]
B	$-0.3726 \cdot 10^3$	0	$0.9720 \cdot 10^4$	$0.7935 \cdot 10^5$	$-0.7575 \cdot 10^4$	$-0.7529 \cdot 10^4$
C	-27.8772	0	$0.8405 \cdot 10^4$	$0.9543 \cdot 10^5$	$-0.9423 \cdot 10^4$	$-3.8131 \cdot 10^3$
D ₁	$0.5970 \cdot 10^3$	0	$0.5271 \cdot 10^4$	$4.3599 \cdot 10^4$	$-1.6844 \cdot 10^4$	$1.8185 \cdot 10^3$
D ₂	$0.7900 \cdot 10^3$	0	$-1.1541 \cdot 10^3$	$-0.9455 \cdot 10^4$	$-4.8125 \cdot 10^3$	$3.3951 \cdot 10^3$
E	$0.6457 \cdot 10^3$	0	$-0.3546 \cdot 10^4$	$-4.3866 \cdot 10^4$	$-2.4423 \cdot 10^3$	$1.6547 \cdot 10^3$
F	$0.7365 \cdot 10^3$	0	$-0.4007 \cdot 10^4$	$-4.0226 \cdot 10^4$	-675.0721	$1.4334 \cdot 10^3$

Table 1.19: Structural loading at the wing root for the critical points of the flight envelope.

It may be noted that the most critical loading is encountered at point B. The subsequent analysis is therefore based on that loading.

9.3 Materials selection

For an urban E-VTOL, performance and costs are major design limiters. The development of light-weight and urban environment resistant composite materials will set the basis of high-performance, economical aircraft, which is required for the large market of electric urban air mobility.

In general, aircraft structure is made mainly of metallic materials such as aluminium, steel and titanium. Aluminium is privileged for skin due to its lower density (a third of steel's density) and a good corrosion resistance, in contrast to steel and titanium with greater tensile strength, Young's modulus and toughness, used mainly to reinforce the structure.

Nevertheless, composites such as carbon fibers-epoxy or carbon fibers-cyanate ester used in high performance vehicles (aircraft, spacecraft, automotive industry) are a balanced trade-off between light weight characteristics and very high

strength capabilities with the added difficulty of manufacturing and material health assessment and a higher cost. Even with the existing difficulties, composites are preferred since they enhance performances.

In the next section, a detailed material selection is performed in order to select the appropriate composite for the wing and fuselage using *CES EduPack 2018* with the *Aerospace Level 3* database.

Criteria

The selection is limited to composites with a polymer matrix. This first criterion provides in *CES* an extensive list of composites with different manufacturing process, lay-up configuration, and percentages of fibers/matrix. Great care should be taken when designing the lay-up to ensure the quasi-isotropic property of the material. This allows to further refine the selection.

The matrix materials used in the aerospace industry are principally

- BMI (bismaleimide) used generally for aerospace components where resistance to elevated temperature performance is required.
- Cyanate ester used generally for high performance spacecraft and aircraft. The matrix has low out-gassing and moisture absorption.
- Epoxy is used for aircraft and aerospace structural parts.
- PEEK (Polyether ether ketone) is also used for lightweight structural members in aerospace and automotive components.
- Phenolic widely used for different applications in aerospace and automotive applications, due to its good thermal and fire retardant properties.
- Polyamide has similar applications to BMI.

Additional constraints on durability are imposed for obvious reasons

- Good or excellent water (fresh and salt) resistance
- Good or excellent UV radiation (sunlight) resistance
- Flammability to slow-burning, self-extinguishing or non-flammable.

For composites, the compressive strength is lower than the yield strength (elastic limit). The product of these two mechanical properties should be maximized. The same reasoning can be applied to Young's modulus and shear modulus: their product should be as high as possible, and if the density is taken into account to favour light materials, the product is divided by the density. Obtaining thus a distribution of $\frac{EG}{\rho}$ as a function of $\sigma_y \sigma_c$ reduces the *CES* list to 19 different composites. The selection becomes more restrictive once the fracture toughness is taken into account. The refinement is

pushed further considering the fatigue strength at 10^7 cycles. A limit value for the fatigue strength is fixed to be higher than the stresses expected from the analytical part.

From 71 composites of polymer matrix available in *CES*, only 11 materials pass through the different stages. Moreover if the price is evaluated, and the pertinence of the material as explained previously is considered, the chosen material is high strength carbon fiber/epoxy composite presenting a quasi-isotropic laminate (0/+45/-45/90) produced from unidirectional tape pre-preg, with a nominal fiber volume fraction of 0.65 and the autoclave cure at 115-180°C with 6-7 bar of pressure. The number of layers used will be deduced from the required thickness of the structure, considering that a single layer of the composite is 0.0049 inches thick.

The properties of this material are summarised in table 1.20 and compared to the widely used aluminum alclad 2024-T3.

	Composite	Aluminum
Price [\$/lb]	39.37	2.19
Density [slug/ft ³]	3.066	5.394
Young's modulus [psi]	$8.702 \cdot 10^6$	$1.088 \cdot 10^7$
Tensile strength (elastic limit) [psi]	107,038	53,954
Shear modulus [psi]	$3.336 \cdot 10^6$	$4.351 \cdot 10^6$
Shear strength [psi·in ^{0.5}]	$1.802 \cdot 10^5$	$2.821 \cdot 10^5$
Fracture toughness [psi·in ^{0.5}]	$1.802 \cdot 10^4$	$3.731 \cdot 10^4$

Table 1.20: Mechanical properties of the selected composite.

It can be noticed that even if the price is much higher, and certain mechanical properties are low in comparison, the fact that the density is almost the half of the aluminum makes the composite worth considering. Moreover, since the wing and the fuselage do not undergo the same loads, a different material could be used for each part. This material optimisation would be done during the continuity of the project.

The material that will be used is considered quasi-isotropic, thus the analytical procedure used for isotropic materials is consistent for the chosen material or at least provides a sufficient starting point for the finite element analysis.

9.4 Fuselage section

Throughout this preliminary design the fuselage will be composed of a skin and several stringers and frames, which will transmit the loads, and its behaviour will be assessed under the action of the forces and moments computed above. This will provide the basis for the finite element simulations.

Analytical study

A preliminary study is performed from the results of the fuselage loading obtained previously. The purpose of this analytical section is to deduce the stresses appearing in a pertinent section. Based on the materials selection, the number of

stringers and the thickness can be determined. Subsequently, the finite element simulation can be carried out, discussed and verified.

For a preliminary design, in order to reduce the complexity of the problem, several assumptions have been imposed. The fuselage section is idealized as a squircle, a square whose corners are quarters of a circle. The resemblance with the real section is more than acceptable. Moreover, the structural elements are taken such that the stringers carry no shear stress but only the direct loading and for the skin, the shear stress is supposed to be constant between stringers. Nevertheless, skin and stringers will participate on carrying the different loads, therefore the analytical study will overestimate the reality.

The reference frame for the fuselage section is such that the origin is at the centroid, the \mathbf{e}_y axis is directed to the right and \mathbf{e}_z upwards.

Bending The skin between stringers is supposed flat. This assumption is correct except for the corners with circular form, for that a major number of stringers is imposed at these locations. The direct stress in each stringer is calculated from

$$\sigma_{xx} = \frac{(I_{zz}M_y + I_{yz}M_z)z - (I_{yz}M_y + I_{yy}M_z)y}{I_{yy}I_{zz} - I_{yz}^2} \quad (1.18)$$

in which the reference axes is positioned at the center of the section (being by symmetry the centroid and shear center).

Since $M_z = 0$ and by symmetry $I_{xy} = 0$,

$$\sigma_{xx} = \frac{M_y}{I_{yy}}z \quad (1.19)$$

The inertia is calculated as a function of the stringers area and their position around the fuselage.

Torsion A fuselage section is essentially a closed beam section. The shear flow produced by a pure torque, here M_x , is given by

$$qT = \frac{M_x}{2S} \quad (1.20)$$

with S the cross-section area of the fuselage. The shear flow is constant over the entire section and its computation is direct.

Shear The shear flow in the skin due to shear forces can be calculated by solving a closed single-cell section beam. The shear flow is obtained by calculating the "open section" shear flow (cutting the skin anywhere between two stringers)

$$q_b = - \left(\frac{I_{zz}T_z - I_{yz}T_y}{I_{yy}I_{zz} - I_{yz}^2} \right) \sum_{r=1}^n A_r z_r - \left(\frac{I_{yy}T_y - I_{yz}T_z}{I_{yy}I_{zz} - I_{yz}^2} \right) \sum_{r=1}^n A_r y_r \quad (1.21)$$

where A_r , y_r and z_r are the stringer's cross-section area and coordinates. All the stringers are supposed to have the same cross-section area. Since T_y and $I_{yz} = 0$,

$$q_b = -A \left(\frac{I_{zz}T_z}{I_{yy}I_{zz}} \right) \sum_{r=1}^n z_r \quad (1.22)$$

The shear flow $q_{s,0}$ is obtained by solving a moment equilibrium, here around the centroid,

$$y_T T_z + z_T T_y = \oint_{fuselage} q_p p ds + 2S q_{s,0} \quad (1.23)$$

where y_T and z_T are the coordinates of application of the shear forces. Thus, the shear flow is given by

$$q_{s,0} = \frac{y_T T_z - \oint_{fuselage} q_p p ds}{2S} \quad (1.24)$$

and the complete shear flow distribution follows by summing up $q_{s,0}$ and q_b .

Final results Using the analytical formulation presented above, the stresses are computed based on the loading of the previous section. Several considerations must be taken into account. The unknowns are the area and the number of stringers. In terms of optimisation of the weight, the small area and reduced number of stringers are the best option, but the validity of the assumptions would be dubious. Indeed, the assumptions and the final result should be in coherence, thus the number of stringers should be sufficiently elevate to ensure the hypothesis of flat skin and constant shear between stringers. This is mainly problematic at the corners due to the circular form. Moreover, the material should withstand both compressive and traction efforts and in this case the compressive strength is the mechanical characteristics that will limit the design since it is the smaller one. Furthermore, a security factor is taken to be $s = 1.5$.

$$\sigma_{max} = \frac{\sigma_{0.1\%}}{s} \quad \text{and} \quad \tau_{max} = \frac{\tau_{strength}}{s} \quad (1.25)$$

Moreover the thickness of the skin should be coherent with the manufacture method of the composite, i.e. the layers lay-up. The thickness of a composite layer is supposed to be 0.0049in. The final structural configuration verifying the different constraints is done with a thickness of the skin of 0,0787in and an area of stringers of 0.0155in². The schematic view of the cross-section of the fuselage is available in Fig. 1.42.

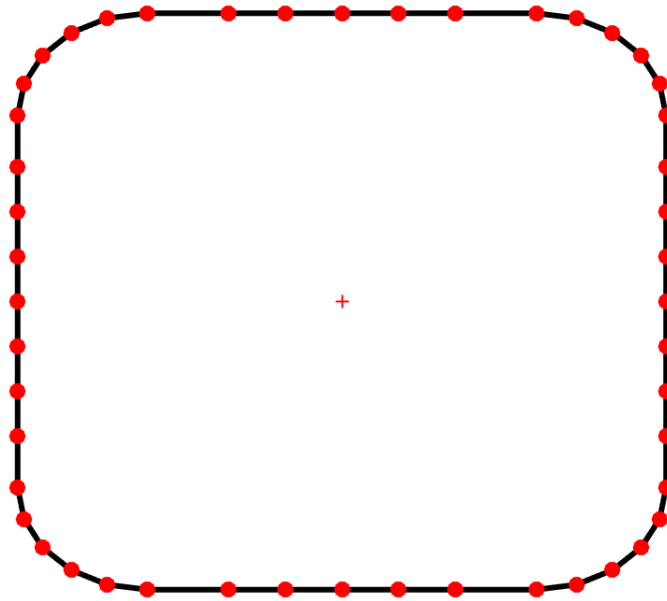


Figure 1.42: Position of stringers (red circles). The cross red is the centroid of the fuselage section.

Finite element study

In this section, the structure of the fuselage is studied using the finite element theory. The goal is to validate the results of the analytical study. To that end, the structure of the fuselage including the stringers, the bulkheads and the skin. The structure of the wing is presented in Fig.1.43

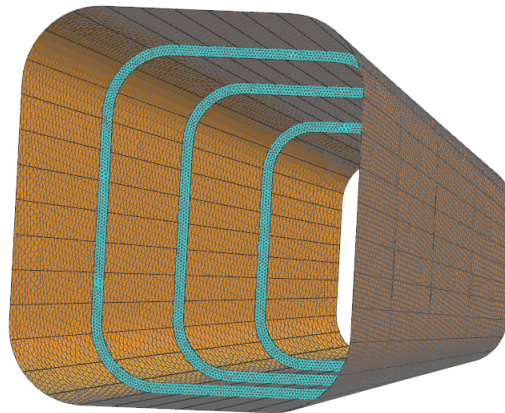


Figure 1.43: Mesh of the fuselage structure.

Boundary condition Once the structure of the fuselage has been meshed, constraints have to be applied on the model. The only condition that must be applied is the clamping of the fuselage at one of its end.

Loading Subsequently, the loads have to be added to the meshed part. Firstly, the self-weight of the fuselage is applied as a downward acceleration with a value of $g \cdot n$ (with n the loading factor). Secondly, the other three forces taken into account -engines, batteries and canard weights- as distributed loads in the transverse direction at the position where the

canard must be applied. These forces have a value of $W_i \cdot n$, where i represents each force. Other forces such as the thrust, the lift of the wing or the weight of the main engines were not taken into account here, since they correspond to the aft part of the fuselage and were already used in the equilibrium equations.

Results In this section, the results of the FEM analysis are briefly discussed. In Fig. 1.44, the deformation of the fuselage under the loading is shown. As can be seen, the deformation of the fuselage is quite limiting. The maximum deflection of the fuselage is located where the canard is attached and is equal to 3.9 in. As far as the stress is concerned, the maximum principal stress is found at the same location as the maximal displacement. Those results are in accordance with the results obtained during the analytical study.

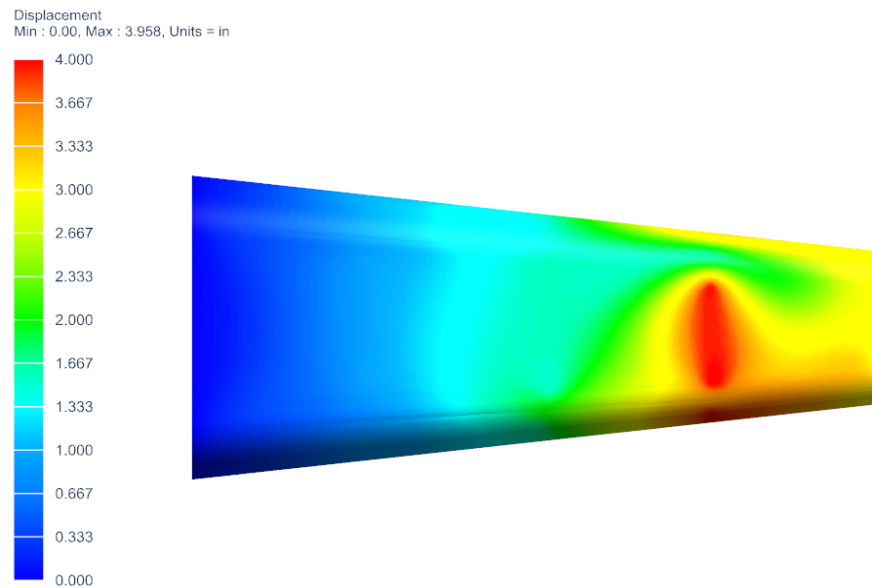


Figure 1.44: Deformation of the fuselage under maximum loading at point C of the flight envelope.

Through successive FEM simulations, it was found that the size of the stringers and bulkhead could theoretically be reduced. However, as composites materials are used, the lay up must be respected. As a result, the size of the different elements cannot be reduced.

9.5 Wing

As for the fuselage, the structure of the wing is made up of a skin, stringers and flanges. In addition, there are also spars in the spanwise direction and ribs in the transverse direction. The spars are connected to the skin using flanges. The structure is deliberately kept simple in this study. To do so, some structural components, for instance rivets, are ignored.

Analytical study

The first step in the preliminary design of the structure of the wing is an analytical study. However, some idealization is required beforehand. It was assumed here that the direct stresses are only carried by the stringers and flanges, while the

shear stress is carried by the skin and the spars. Furthermore, the shear flow is assumed to be constant along each spar and between stringers. This assumption is valid as long as the distances involved are small. This evaluation inevitably leads to oversized stringers. Eventually, warping was allowed even though the wing is clamped. This very last assumption has the opposite effect compared to the previous one: it leads to under-sized stringers. This is due to the fact that torsion of a clamped beam induces direct longitudinal stresses. Therefore, when performing the finite element analysis, great attention should be paid to those details.

The objective of this analytical study is twofold. Firstly, it is used to determine the configuration of the structure. Through an iterative process, the number of stringers and their positions can be optimized. Secondly, the areas of the stringers, flanges and the size of the spars can easily be computed during this stage. All this information is then used to perform the finite element simulations. After the analytical study, the optimised configuration has 35 stringers, 4 flanges and 2 spars. Moreover, the trailing edge of the wing is occupied by the engines and control surfaces and consequently without structural role.

In the following paragraphs, the method and the formulas used are described. The results are then presented. Notice, that the reference frame for the wing cross-section is such that the origin is at the leading edge, the \mathbf{e}_y axis is directed towards the leading edge and \mathbf{e}_z upwards.

Bending The expression to evaluate the direct stresses in the stringers for an untapered wing is

$$\sigma_{xx} = \frac{(I_{zz}M_y + I_{yz}M_z)z - (I_{yz}M_y + I_{yy}M_z)y}{I_{yy}I_{zz} - I_{yz}^2} \quad (1.26)$$

in which the coordinates (y, z) refer to any point in the cross-section and the inertias are evaluated from the axes $C\mathbf{e}_y, \mathbf{e}_z$ where the origin coincides with the centred of stringers and flanges. No simplifications can be performed since the airfoil is not symmetric and both moments M_y and M_z are present.

Torsion For the torsion, only pure torque is considered with no axial constraint effects, i.e. no direct stress in the wing section, only shear. The stringers will not affect this analysis. The wing section comprises of 2 cells carrying a torque M_x , generating 2 unknown shear flows, q_I and q_{II} (where I and II refers to the two cells). The total torque is

$$M_x = 2S_I q_I + 2S_{II} q_{II} \quad (1.27)$$

where S represents the cross-section of the cells. Additional equations are required for the 2 cells, relating the rate of twist in the cell and the shear of the cell. closing the system (the unknowns are then q_I , q_{II} and $\frac{d\theta}{dx}$) since the twist rate is the same for both cells (by compatibility) with two equations of the type

$$\frac{d\theta}{dx} = \frac{1}{2S_i G} \oint_{C_{cell_i}} \frac{q}{t} ds \quad (1.28)$$

since the same shear modulus G is used for the entire wing and where t is the thickness. The circular integral is simply the length of the walls of the given cell multiplied by the shear load. Solving the system will provide the shear flow, and thus the shear stress by dividing by the wall thickness.

Shear flow The effect of shear loads should be added to the shear stresses obtained from pure torque (torsion). Since these loads do not pass necessarily through the shear center, the results is the combined effect of shear and torsion due to the shear loads.

The method used here is similar to the torsion solution, but extended to take into account the presence of stringers. Moreover, here the skin is "cut" to obtain a statically determinate wing section. The open section shear flow q_b is given by

$$q_b = - \left(\frac{I_{yy}T_y - I_{yz}T_z}{I_{yy}I_{zz} - I_{yz}^2} \right) \sum_{r=1}^n A_r y_r \quad (1.29)$$

However, the shear flow at the cut walls is still unknown, $q_{s,0,I}$, $q_{s,0,II}$, while the rate of twist $\frac{d\theta}{dx}$ which is given by

$$\frac{d\theta}{dx} = \frac{1}{2S_i G} \oint_{Cell_i} \frac{q_b + q_{s,0,i}}{t} ds \quad (1.30)$$

where the $q_{s,0,i}$ is seen as a constant shear flow acting around the cell, and the shear flow around a cell is obtained by summing up the open section shear flow. Therefore, two equations of this type are obtained. A third equation is needed, which is the moment equilibrium,

$$T_{yzT} - T_{zyT} = \sum_{i=1}^2 \oint_{Cell_i} \frac{q_b p_0}{t} ds + \sum_{i=1}^2 2S_i q_{s,0,i} \quad (1.31)$$

Solving this system will provide the shear stress due to shear loads once the shear flow is divided by the thickness of the skin.

Final results Using the formulas presented above, the stresses at the wing root can be computed based on the loading. Then the materials and the size of each element must be chosen such that the structural elements always remain in the elastic region for every point of the flight envelope. This means that the stresses must always remain under the elastic limit. A safety factor s must be applied onto the elastic limit to further increase safety. Here, this safety factor is taken to be $s = 1.5$. Therefore, the maximum tensile and shear stresses are given by:

$$\sigma_{max} = \frac{\sigma_{0.1\%}}{s} \quad \text{and} \quad \tau_{max} = \frac{\tau_{strength}}{s} \quad (1.32)$$

The values obtained after the analytical study are presented in table 1.21 and a graphic representation of the section is given in Figure 1.45.

A_{str} [in^2]	A_{fl} [in^2]	t_{spars} and t_{ribs} [in]	t_{skin} [in]
0.217	0.217	0.157	0.0787

Table 1.21: Values of the main structural elements obtained with the analytical study.

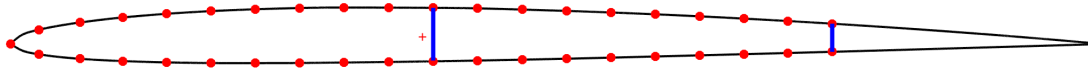


Figure 1.45: Position of stringers and flanges (red circles) and spars (blue). The red cross is the centroid of the wing section.

Finite element study

The structure of the wing has been designed by means of an analytical approach in the previous section. In this section, the finite element method is used to validate the results. To do so, a CAD of the wing structure was constructed and is presented in Figure 1.46. The structure is then meshed using shell elements (see Figure 1.47) and is studied using the loads computed previously.

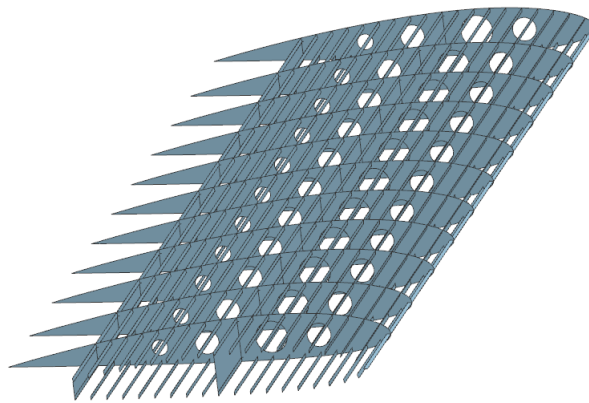


Figure 1.46: Internal structure of the wing as studied using NX.

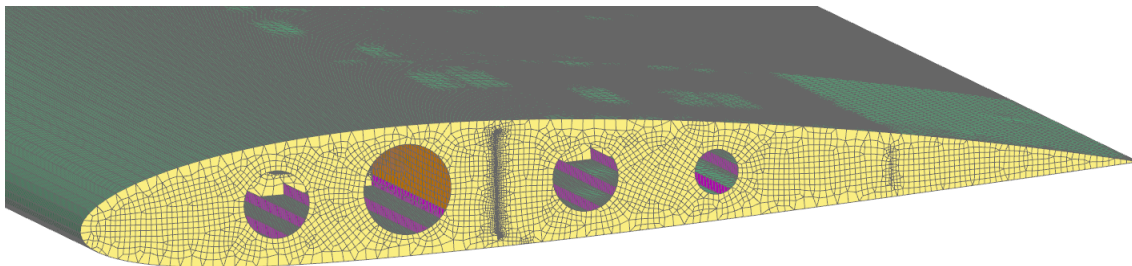


Figure 1.47: Mesh of the wing structure.

Boundary condition Once the model has been meshed, constraints have to be applied on the model. The first condition to impose is the clamping of the wing at its root. This physically represents the clamping of the wing in the fuselage.

Loading The different loads that must be applied on the wing have been described previously. In this paragraph, the way these loadings are applied to the model for the FEM analysis are described. Firstly, the self-weight of the half-wing is simply taken into account by imposing an acceleration which equals $n \times g$. The weight of the engines is taken into account by applying a linear force along the second spar which is equal to $W_{eng} \times n \times g$. The same formula is used for the weight of the battery and is applied onto the spars and the ribs. As far as the thrust is concerned, a force and a moment are applied at the location of the motors: between the third and the tenth ribs on the second spar. A moment is required since the motors are located on top of the wing's skin. Lastly, the lift and drag are modeled using the lift distribution obtained from aerodynamic analysis performed using *Tranair*.

Results Using the finite element method, several simulations were performed in order to optimize the structure of the wing. In the end, the sizes of the different components are updated. The new values are presented in table 1.22.

A_{str} [in^2]	A_{fl} [in^2]	t_{spars} [in]	t_{ribs} [in]	t_{skin} [in]
0.128	0.128	0.11	0.11	0.055

Table 1.22: Values of the main structural elements obtained through finite element analysis.

Nevertheless, even if the thickness is reduced, the composite lay-up will impose a certain number of layers with a given thickness, this is, a layer of composite is 0.0049 in and to obtain a quasi-isotropic behaviour four layers are needed, and to verify the required thicknesses from the FEM analysis, 8 layers. Therefore, the results in Table 1.21 are kept for the thickness of spars, ribs and skin.

Fig. 1.48 shows that, the maximum stress was not located at the wing root. Rather, it could be found at the second spar where the motors are fixed. As far as the wing root is concerned, the greatest stresses are found in the flanges of the front spar. This is consistent with the results of the analytical study. Additionally, from the numerical analysis, it was found that the deflection at the wing tip for point B of the flight envelope was 5.5 in, which is an acceptable value.

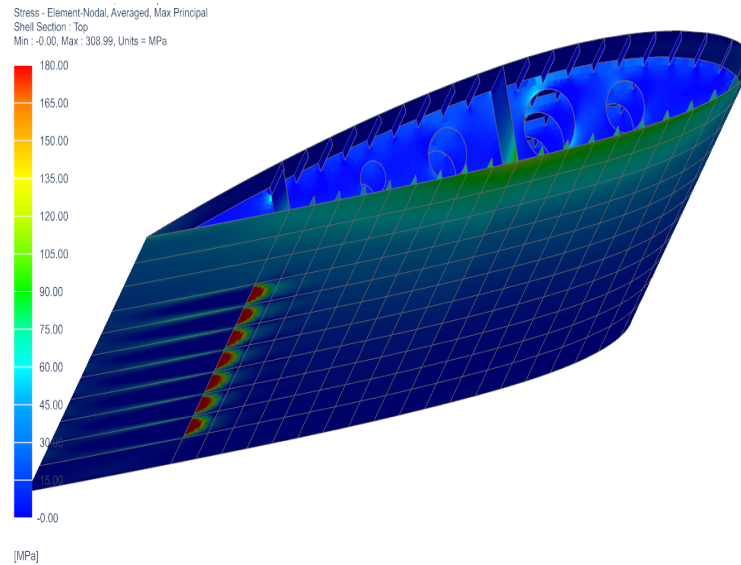


Figure 1.48: Maximal principal stresses on the structure of the wing under maximum loading at point B of the flight envelope.

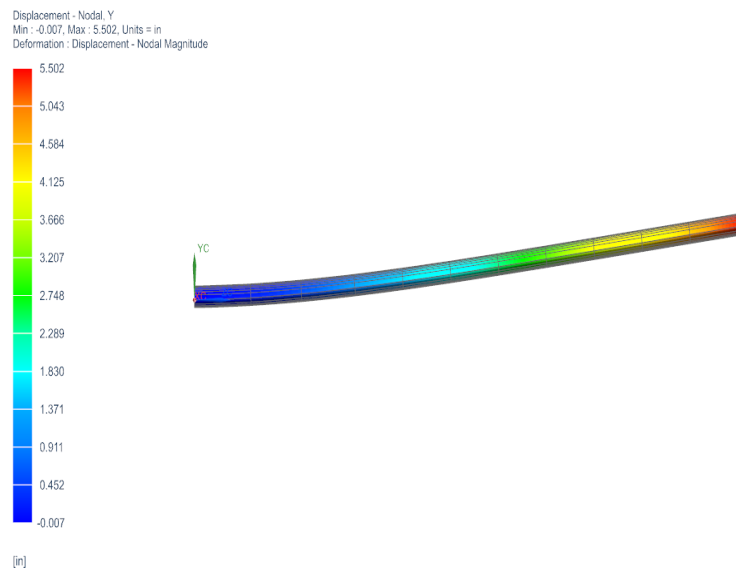


Figure 1.49: Deflection of the wing under maximum loading at point B of the flight envelope.

9.6 Structure Conclusion

Through simple analytical formulas and basic finite element simulations, the structure of the wing and of the fuselage of the Mistral Air Taxi have been designed. It must be noted that during this preliminary analysis, strong assumptions were made in order to simplify the work and obtain a starting point for the finite element simulations. Furthermore, the fuselage and the wing were studied separately. In addition, only one section of the fuselage was studied, and some elements of the wing like the ailerons or the spoilers were ignored. Therefore, the results obtained are obviously not optimized. However they are satisfactory for the preliminary design of the aircraft. In later stages of the design, more advanced analysis will be

performed to optimize the structure. Example of such analysis include modal analysis, vibratory analysis, fatigue analysis and crack resistance verification. Moreover, since composites are used, the evaluation of its resistance should be evaluated properly as detailed in [54].

10 Stability analysis

10.1 Pitching moment stability

In order to be FAA compliant, the value of the controls fixed stability margin (κ_n) and the controls free stability margin (κ_n') must be over 5%. This should be verified for any number of passengers (0 to 4). In that case, the plane is said to be stable. These values must not exceed 20% so that the aircraft stays maneuverable.

The important distances used to calculate pitching moment equilibrium and the stability margins are given in Fig. 1.50.

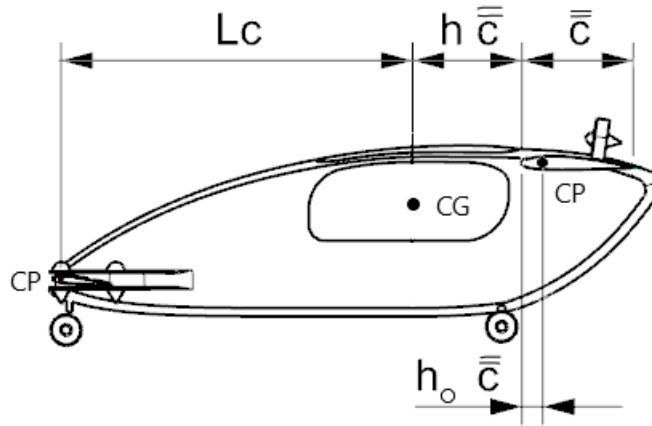


Figure 1.50: Important lever arms used for the pitching moment stability.

With this geometry, the controls fixed stability margin and the controls free stability margin are defined as:

$$\kappa_n = (h + h_0) \left(1 - \frac{d\varepsilon}{d\alpha}\right) - V_c \frac{a_1}{a} - \frac{dC_{m_{fus}}}{dC_{L_w}} \quad (1.33)$$

$$\kappa_n' = (h + h_0) \left(1 - \frac{d\varepsilon}{d\alpha}\right) - V_c \frac{a_1}{a} \left(1 - \frac{a_2 b_1}{a_1 b_2}\right) - \frac{dC_{m_{fus}}}{dC_{L_w}} \quad (1.34)$$

where the different coefficients are:

- $V_c = \frac{l_c S_c}{\bar{c} b}$ is the canard volume ratio with respectively S_c , \bar{c} and b the surface of the canard, the chord of the wing and the span of the wing.

- a is the slope of the lift coefficient of the wing
- $\frac{d\varepsilon}{d\alpha}$ is the slope of the downwash angle with α
- a_1 and a_2 are so that the canard lift coefficient can be written: $C_{Lc} = a_1\alpha_c + a_2\eta$
- b_1 and b_2 are the elevator hinge moment coefficient: $C_H = b_1\alpha_c + b_2\eta$

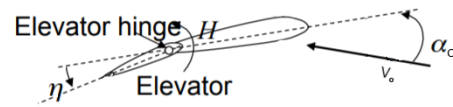


Figure 1.51: Schematic of the elevator.

- $\frac{dC_{mfus}}{dC_{Lw}}$ is the fuselage effect computed with the empirical method NACA TR711

The values of the controls free and fixed stability margins are not between 5 and 20% for all the possible configurations. This means that rules on where the passengers have to sit must to be imposed. The allowable configurations are given in table 1.23

Number of passengers	Allowed configurations
0 passenger	
1 passenger	
2 passengers	
3 passengers	
4 passengers	

Table 1.23: Allowed configurations.

The values of the controls fixed and free stability margins of the kept configurations are given in the Tab. 1.24.

Table 1.24: controls fixed and free stability margins

	case 1	case 2	case 3	case 4	case 5	case 6	case 7
κ_n	0.0871	0.1191	0.0573	0.0882	0.118	0.0626	0.0903
κ_n'	0.156	0.1874	0.1267	0.1571	0.1864	0.1319	0.1591

10.2 Dynamic analysis

The scope of this section is to present both the dynamic behaviour of the airplane in terms of vibration modes and the control system developed in order to achieve the stability requirements imposed by the FAA. This analysis focuses on the response of the airplane during cruise as the airplane spends most of its mission time in cruise configuration (more than 70% as shown later in Section 11). Moreover, a section is dedicated to analyse the feasibility of the no-tail configuration by analysing the yaw control dynamics.

Methodology

The full 6-DOF non-linear equations of motion, Eqs. A.1 presented in Appendix 2, are linearized around the cruise equilibrium configuration Eqs. 1.35. These equations involve the perturbation trims. The LHS represent the inertial loads while in the RHS are expressed the external forces and moments acting on the body axes of the airplane.

$$\left\{ \begin{array}{l} m\dot{u} = X_g + X_a + X_p + X_c \end{array} \right. \quad (1.35a)$$

$$\left\{ \begin{array}{l} m\dot{v} + mU_e r = Y_g + Y_a + Y_p + Y_c \end{array} \right. \quad (1.35b)$$

$$\left\{ \begin{array}{l} m\dot{w} - mU_e q = Z_g + Z_a + Z_p + Z_c \end{array} \right. \quad (1.35c)$$

$$\left\{ \begin{array}{l} I_x \dot{p} - I_{xz} \dot{r} = L_a + L_p + L_c \end{array} \right. \quad (1.35d)$$

$$\left\{ \begin{array}{l} I_y \dot{q} = M_a + M_p + M_c \end{array} \right. \quad (1.35e)$$

$$\left\{ \begin{array}{l} I_z \dot{r} - I_{xz} \dot{p} = N_a + N_p + N_c \end{array} \right. \quad (1.35f)$$

The evaluation of the RHS is not straightforward; particular attention must be paid for the aerodynamic and control forces. Their definition is based on the so called *Stability and Control derivatives* whose evaluation is performed following the USAF DATCOM guidelines [55].

To better underline the dynamic properties of the aircraft it is useful to rewrite Eqs. 1.35 in a *State Space formulation* Eqs. 1.36 where $x = \{x y z p q r \phi \theta \psi\}$ is the state vector, $u = \{\omega_1 \dots \omega_{14} \xi \eta\}$ is the input vector and y is the output vector defined depending on what it's supposed to analyse.

$$\begin{aligned} \dot{x} &= Ax + Bu \\ y &= Cx + Du \end{aligned} \quad (1.36)$$

Generally pitch stability is decoupled from roll and yaw stability and the equations of motion are split into: *Longitudinal stability* involving $x_{Long} = \{x z p \theta\}$ and u_{Long} , and *Lateral stability* involving $x_{Lat} = \{y p r \phi \psi\}$ and u_{Lat} . It's thus possible to write Eq.1.36 for both longitudinal and lateral equations.

Mode analysis

The properties of the modes of vibration of the aircraft are expressed through the eigenvalues of the matrix A . Complex conjugate eigenvalues generate oscillatory modes and are named *dutch roll*, *phugoid oscillation* and *short period oscillations* (SPO); the first is associated with the lateral stability and represents the coupling mode between rolling and yawing, while the last two are associated with longitudinal stability. Real eigenvalues describe round non-oscillatory modes, the *spiral divergence* and the *roll subsidence*.

A mode of vibration is defined stable if its related eigenvalue has a negative real part and the aircraft is defined stable if all its modes of vibration are stable. For each mode *Time constant* T_c can be defined to characterize the modal response to a step input; furthermore the oscillatory mode properties are described through three other important parameters: the *natural frequency* ω_n , the *damped frequency* ω_d and the *damping factor* ξ . The first two represent the frequency of vibration of the associated mode in the undamped and damped case, while the damping factor expresses the intensity of the damping itself.

The A -matrices for lateral and longitudinal state-space equations are shown below and their eigenvalues are represented in Fig. 1.52. Eigenvalues and their associated parameters are also listed in Tab. 1.25

$$A_{lat} = \begin{bmatrix} -0.1943 & 0 & 0 & 9.81 & 0 \\ -0.1825 & -4.622 & 0.0116 & 0 & 0 \\ -0.4457 & -0.7094 & 0.0414 & 0 & 0 \\ 0 & 1 & 0 & 0 & 0 \\ 0 & 0 & 1 & 0 & 0 \end{bmatrix} \quad A_{long} = \begin{bmatrix} -0.0442 & 18.7 & 0 & -32.2 \\ -0.0013 & -2.18 & 0.97 & 0 \\ 0.0024 & -23.8 & -6.08 & 0 \\ 0 & 0 & 1 & 0 \end{bmatrix} \quad (1.37)$$

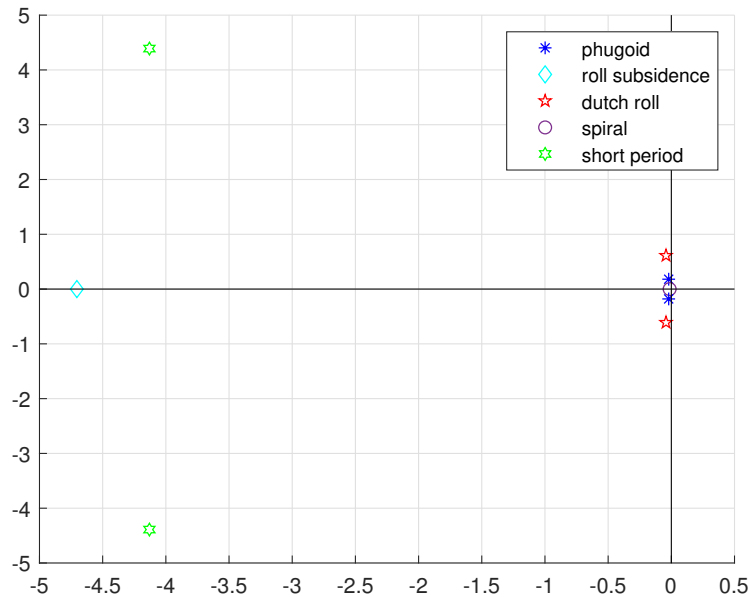


Figure 1.52: Representation in the complex plane.

	Mode of vibration	Eigenvalue	ω_n	ω_d	ξ	T_c
Longitudinal modes	Phugoid	$-0.0209 \pm 0.18i$	0.179	0.178	0.117	47.73
	SPO	$-4.13 \pm 4.39i$	6.03	4.39	0.758	0.24
Lateral modes	Roll subsidence	-4.7	/	/	/	0.21
	Dutch roll	$-0.0421 \pm 0.6111i$	0.6125	0.611	0.0687	23.7
	Spiral divergence	0.0134	/	/	/	74.8

Table 1.25: Characteristics of the vibration modes of the aircraft.

All the mode attributes comply with the requirements imposed by FAR for cruise phase, except for the dutch roll. It is thus necessary to develop an adequate control system to match the requirements.

Control system

The primary aim of the control system presented in this section is to ensure compliance of the mode attributes with FAR requirements. Moreover the control system must enable the aircraft to properly follow the reference state imposed by the autopilot in order to pursue the desired trajectory. It is out of the scope of this report to design the automatic pilot and to design the process through which the reference state is generated for trajectory keeping.

In the wide range of control techniques, the *Linear Quadratic Integral control* (LQI) is adopted because of its unique characteristics: it grants the stabilization of the system with the minimal control effort ensuring also a steady state error $e_{ss} = r - Cx$ of zero [56] (reference state following). The LQI adopts a full state feedback control law such that the input vector u can be written as

$$u = -Gx \quad (1.38)$$

and tune the G matrix, called *Gain matrix* in order to minimize the cost function expressed in Eq. 1.39

$$J = \frac{1}{2} \int_0^{\infty} x^T Q x + u^T R u dt \quad (1.39)$$

The mathematical procedure used for tuning LQI parameters (Q and R matrices) is based on the theoretical discussion presented in [56]. The application of LQI to the aircraft dynamic model provides new dynamics characteristics represented by new eigenvalues and thus new modes properties whose values are presented in Tab. 1.26

	Mode of vibration	Eigenvalue	ω_n	ω_d	ξ	T_c
Longitudinal modes	Phugoid	-3.2 ± 4.3	5.37	4.3	0.599	0.31
	SPO	-7922	/	/	/	0.0001
Lateral modes	Roll subsidence	-1	/	/	/	1
	Dutch roll	-2.27 ± 2.16	3.13	2.16	0.726	0.44
	Spiral divergence	-2480	/	/	/	0.0004

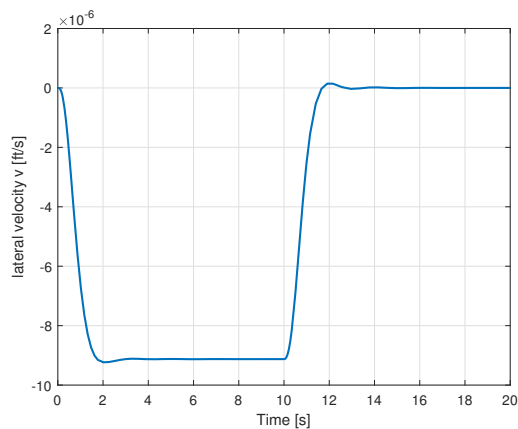
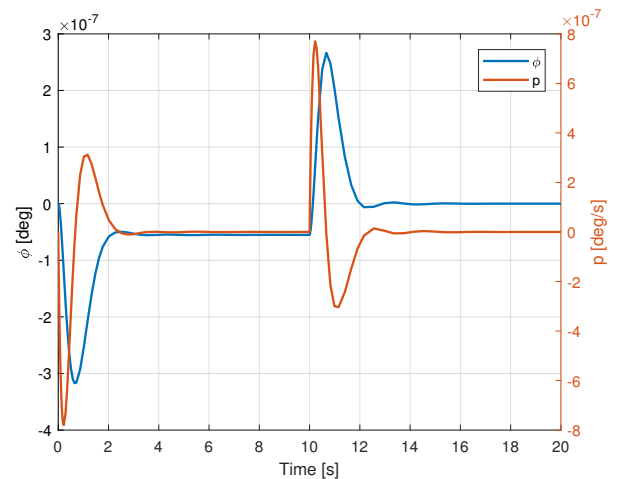
Table 1.26: Aircraft mode of vibration under LQI control action.

As shown in Tab. 1.26 all the modes are heavily damped by the control system. Significant is the influence of LQI upon SPO; the mode it's not anymore an oscillatory mode as the control action prevent the system to oscillate providing a damping value higher than the critical damping. Adopting LQI control system the FAR requirements for the dutch roll, as well as for all the other modes, are fully achieved.

10.3 Yaw controls

As the Mistral Air Taxi presents no tail nor rudder, the yaw control is actuated through *Differential Thrust Technique*; it is based on a proper tuning of the thrust provided by each aircraft engine in order to obtain a net control moment around the yaw axis. Scope of this section is to demonstrate the feasibility of the technique by proving the capability of the airplane to follow and imposed yaw angle law without major changes in the remaining state components.

A reference state of $\psi = 10$ [deg] is imposed to be reached with yaw velocity $r = 1$ deg/s and it's given as input to the aircraft control system. Fig. 1.53, Fig. 1.54 and Fig. 1.55 show the evolution of the state during a simulation period of 20s.

Figure 1.53: Lateral velocity v perturbation evolution.Figure 1.54: Roll angle ϕ and roll angular velocity p evolution.

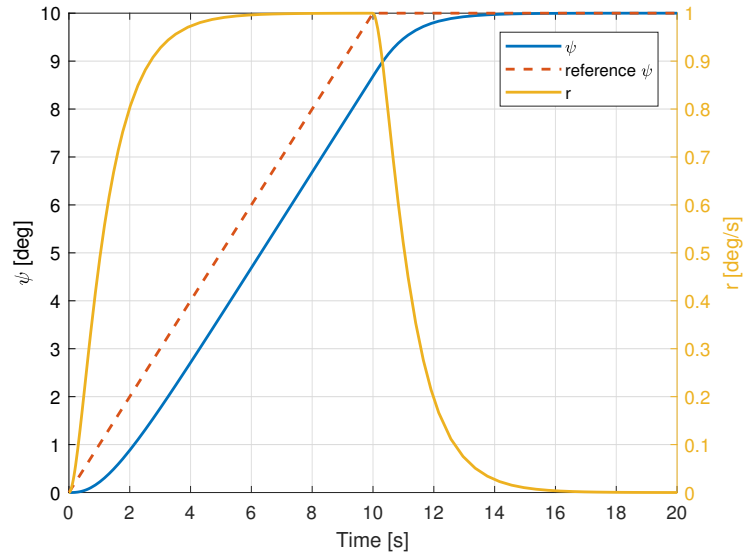


Figure 1.55: Yaw angle ψ and yaw velocity r evolution. The dotted line represent the commanded yaw angle

From the results presented, it is straightforward to conclude that yaw control is stable and its influence upon the other state parameters is negligible (order of magnitude of $10^{-6} - 10^{-7}$). Computing the engine effort in terms of RPM, the variations with respect to the cruise rotational speed are of the order of 0.001% so that the energy consumption can be considered not affected by the control system. From the previous considerations the *differential thrust technique* is thus feasible.

11 Aircraft performance

In the previous sections, the most important subsystems of the E-VTOL were designed and their influence upon the characteristics of the aircraft were explained; the analysis here presented, instead, takes the aircraft as a whole to show its global performances throughout the flight envelope.

The sizing mission described in the AIAA proposal has been divided in different segments:

- Take-Off and Hovering
- Transition to climb
- Climb
- Cruise
- Descent
- Transition to hover
- Breaking
- Hovering and Landing

which are analysed in this section according to the following quantities and their behaviour with respect to the design parameters of each segment:

1. Kinematic: phase time, distance covered, velocity, aircraft attitude.

2. Forces: required thrust profile, engines rotational speed, lift and drag evolution.
3. Energy consumption

11.1 Segment Analysis

Methodology

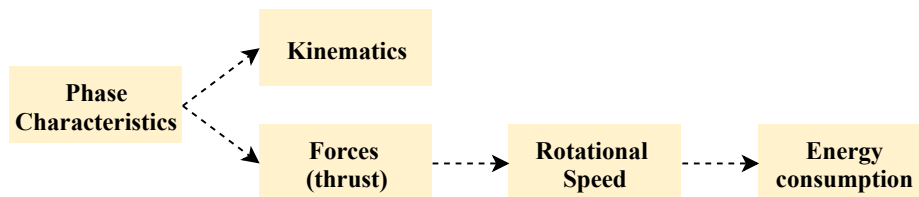


Figure 1.56: Segment analysis flow path.

Each mission segment is analysed according to the methodology shown in Fig. 1.56. A set of parameters is selected in order to provide an exhaustively description of each phases (time, distance covered, thrust level etc.); their choice is aimed to study the behaviour of the airplane at the RFP constrain limits.

It is worth describing the procedure to estimate the energy consumption from the thrust profile, a procedure common to all the segment analysis.

From Thrust profile to Energy consumption

The engines behaviour is modeled using the *Blade Element Method Theory (BEMT)* which is able to calculate the engine response in terms of thrust, torque and required power as functions of the rotational speed and the flight velocity. The issue is to inverse the relation provided by BEMT in order to estimate the rotational speed of the engine (and thus the power required) once the thrust profile is known, for all the different flight velocities.

First, the thrust response as a function of the square of rotational speed and the flight velocity is mapped using BEMT. This behaviour tends to be non-linear as the flight speed increases and its non-linearity is mainly concentrated in the region close to zero RPM, as shown in Fig. 1.57.

Thus a polynomial third order interpolation is carried out in order to capture properly the non-linearity and to easily inverse the Thrust-Rotational Speed relationship as shown in Fig. 1.58.

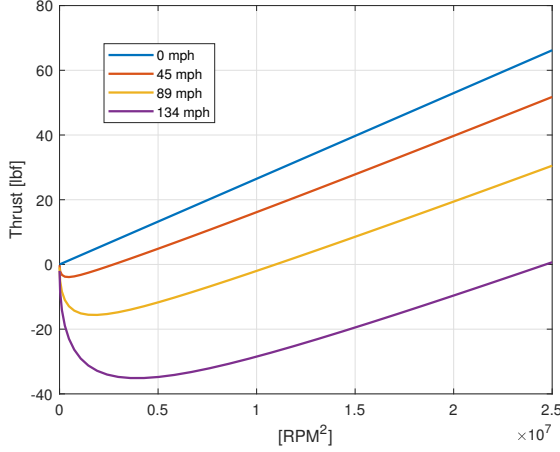


Figure 1.57: Thrust behaviour with respect to RPM^2 of the wing engines.

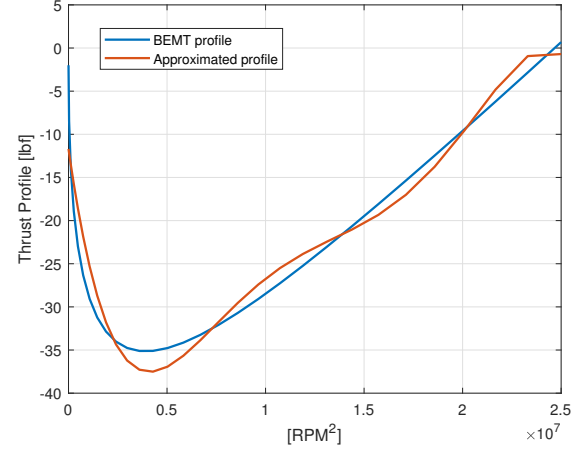


Figure 1.58: Approximation of the thrust profile as function of RPM^2 for wing engines for a flight velocity of $v = 134\text{mph}$.

Take Off and Hovering

From the proposal the total phase duration is fixed to $T_{total} = 90\text{s}$ within which the aircraft must reach an altitude of $h = 15\text{ft}$ and hover. Starting from these constraints, the motion of the E-VTOL is divided into four parts: *Acceleration segment - Constant Speed segment - Deceleration segment - Hovering* such that the resulting kinematics of the take-off is expressed according to

$$\begin{cases} h = \frac{1}{2}a_{acc}\Delta t_{acc}^2 + \omega_{cs}\Delta t_{cs} + \omega_{cs}\Delta t_{dec} + \frac{1}{2}a_{dec}\Delta t_{dec}^2 \\ T_{to} = \Delta t_{acc} + \Delta t_{cs} + \Delta t_{dec} \\ T_{to} = T_{total} - T_h \end{cases} \quad (1.40)$$

where a_i and Δt_i are respectively the accelerations and times of the segments, ω_{cs} is the vertical velocity of the Constant Speed segment, T_{to} is the time period for the take off and T_h is the time period for the hovering.

Assuming that **the acceleration and deceleration segments take the same amount of time** (and thus the same acceleration value with opposite sign), the problem can be parametrized as function of the constant speed segment velocity ω_{cs} .

The design parameters thus are ω_{cs} and T_{to} whose values are imposed to $\omega_{cs} = 1\text{ft/s}$ and $T_{to} = 60\text{s}$ in order not to overload the engines. Due to the previous assumptions, the problem is perfectly symmetric with respect to its kinematics. This implies that the energy consumption is not dependant on the design parameters. The results are listed in Table.1.27.

	Acceleration segment	Constant Speed segment	Deceleration segment
Accelerations [ft/s^2]	0.89	0	-0.89
Time periods [s]	1	58	1
Wing Thrust [lbf]	2,179	2,121	2,063
Canard Thrust [lbf]	1,469	1,430	1,391
Wing Rotational Speed [RPM]	7,672	7,566	7,461
Canard Rotational Speed [RPM]	7,882	7,774	7,663

Table 1.27: Hovering results.

With an **Energy consumption** = 11.25 [kWh].

Transition to climb

During this phase, the transition between vertical and horizontal flight occurs and the wing engines tilt from the vertical configuration ($\Omega = 0$) to the horizontal one ($\Omega = \frac{\pi}{2}$). Due to the tilting of the engine, the aircraft is subjected to an horizontal acceleration leading to the generation of an increasing amount of lift during the transient period. A balance between tilting velocity, horizontal acceleration and lift produced is thus necessary to avoid loss of elevation which represents the main issue of the phase.

In order to solve the problem the Eqs. 1.41, describing this type of motion with respect to an earth inertial reference frame, are integrated imposing:

- Constant angle of attack of the airplane $\alpha = 0$ [deg].
- The maximum difference between the weight of the aircraft and the global sustaining force (lift + vertical thrust) to a value of $\Delta F = 2.25$ [lbf].
- Constant tilting velocity of the engines $\dot{\omega} = \frac{\pi}{2T}$, where T is the transition period.

$$\begin{cases} m\ddot{x} = T_w \sin\Omega - D - D_e & (1.41a) \\ m\ddot{y} = L + T_w \cos\Omega + T_c - mg & (1.41b) \\ T_w \cos\alpha l_w + T_w \sin\Omega h_w + L_w L_{wp} - D_e h_w = L_c l_{cp} + T_c l_c & (1.41c) \\ L_w l_{wp} + T_w h_w = L_c l_{cp} & (1.41d) \end{cases}$$

Imposing different transient periods it is possible to analyse the impact of the transient phase on the energy consumption and engine workload as shown in Fig. 1.59.

As shown in Fig. 1.60 the lift generation at the transition end, though it never reaches the required value to sustain the flight, remains very close to it. Comparing Fig. 1.59 with Fig. 1.60 and considering that: engines must be overload the least possible and the lift generated at the end of the transition must be as close as possible to the weight of the aircraft, **the transition period is imposed to 20s.**

The missing amount of lift necessary to compensate the weight is assumed to be compensated by a small variation of the angle of attack of the aircraft commanded by the automatic pilot.

According to the transient period choice the thrust profile and lift generation is presented in Fig. 1.61, while the other results are listed in the Table 1.28.

After this phase the canard engines are turned off.

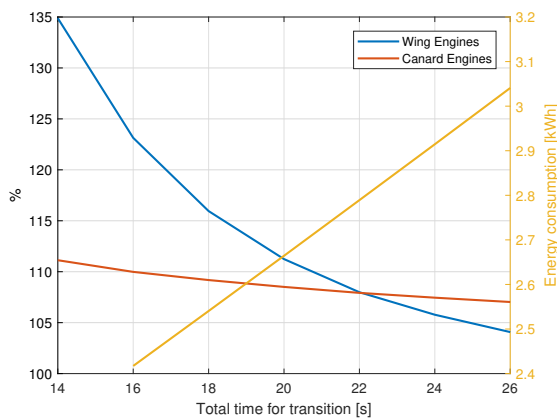


Figure 1.59: The red and the blue lines represent the peak power required by the engines for the transition phase, expressed in percentage with respect to the hover nominal power. In yellow is presented the energy requirement trend with respect to the total transition period.

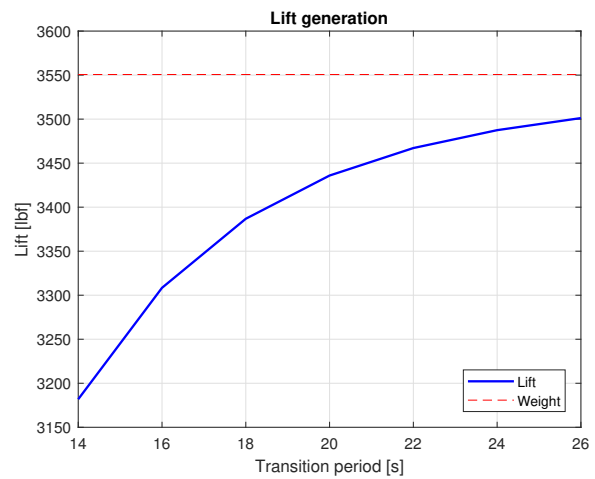
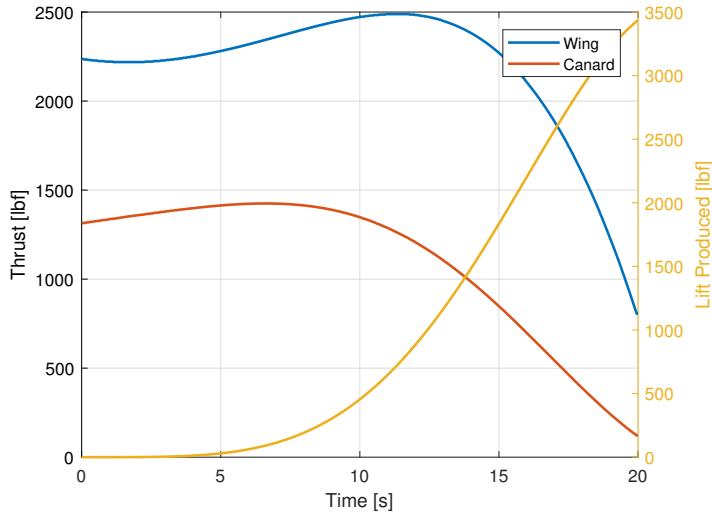


Figure 1.60: Lift produced at the end of the transition period as function of the transition period.



Period [s]	20
Distance [mi]	0.33
Altitude loss [in]	6.3
Final Velocity [mph]	141
Wing Peak [-]	111%
Canard Peak [-]	108%
ΔL [lbf]	115
Energy consumption [kWh]	2.66

Table 1.28: Transient results.

Figure 1.61: Wing, canard thrust (magnitudes) and lift profile over the transition phase.

Climb

Once the transition phase is completed, the aircraft is supposed to reach the velocity enabling it to sustain the flight at the cruise designed angle of attack. It takes the value of $V_{ref} = 143mph$ and it is set as the reference velocity for climbing.

According to the climb Eqs. 1.42, valid under the hypothesis of small climb angle γ , and setting the climb reference velocity to V_{ref} it is possible to study the performances dependence on the variation of cruise altitude and desired climbing velocity. The relation between performances and altitude of cruise is investigated by fixing the climbing velocity to the minimum imposed by the proposal, $V_{climb} = 500$ ft/min, while the influence of the climbing velocity is studied imposing the end of climb altitude at $h = 1500$ ft.; results are shown in Fig.(1.62) and Fig. 1.63.

$$\begin{cases} \gamma = \frac{T-D}{W} \\ V_v = \frac{P_a - P_r}{W} \end{cases} \quad (1.42)$$

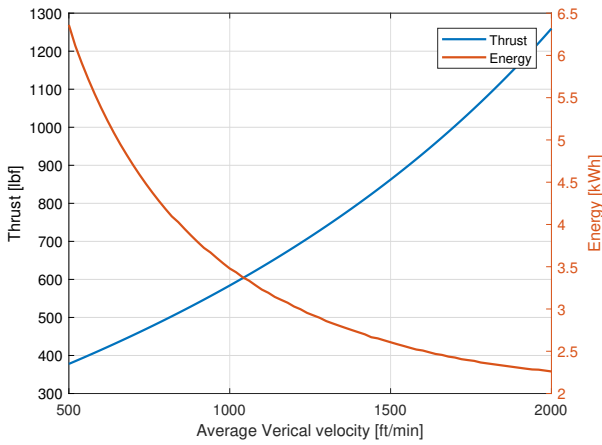


Figure 1.62: Wing engine thrust and energy consumption as a function of the desired vertical velocity.

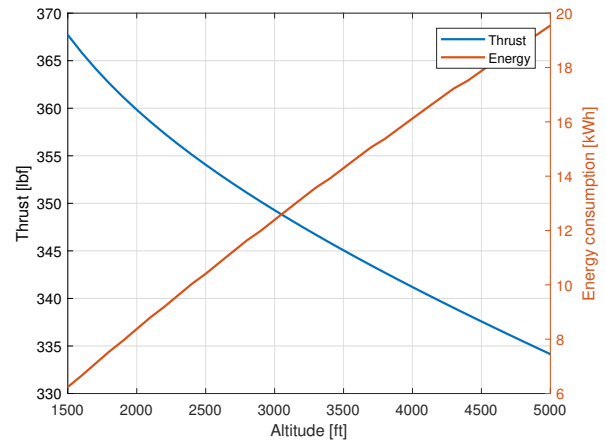


Figure 1.63: Wing engine thrust and energy consumption as a function of the cruise altitude.

Imposing $h_{cruise} = 1,500ft$ and $V_v = 500 ft/min$ result are presented in Tab. 1.29

Period [s]	154
Distance covered d_{climb} [mi]	6.15
γ [deg]	2.6
Thrust [lbf]	378
Rotational Speed [RPM]	6408
Energy consumption [kWh]	6.36

Table 1.29: Climb results for minimum requirements.

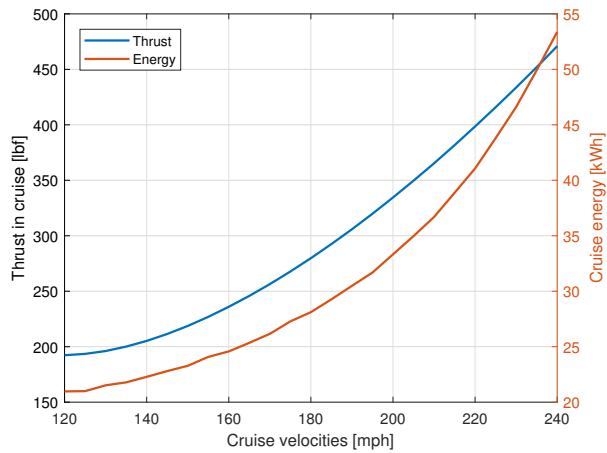
Cruise

The analysis of the cruise phase is based on the evaluation of performances depending on the cruise velocity. It is supposed that the variation of density with respect to altitude, for a cruise altitude of 1,500 ft is negligible; thus the performances evaluation are analysed imposing $\rho_{@1500ft} = \rho_0 = 0.00238 [slug/ft^3]$.

Moreover as the proposal imposes an average velocity of 150 mph for climbing, cruise and descent phases, a $V_{Cruise} = 160mph$ is imposed to match the requirement.

In the proposal, it is stated that the distance from the beginning of the climb to the cruise end must be equal to 60 mi; thus, referring to the minimum requirements for the climb phase, the necessary cruise distance must be $d_{cruise}[mi] = 60 - d_{climb}$. The analysis is conducted until the *maximum cruise speed* = 240 mph, imposed by engine limitations.

Results are shown in Fig. 1.64 while performance parameters referring to minimal requirements are listed in table 1.30, for $V_{cruise} = 160mph$ as specified previously;



Period [min]	22.5
Velocity [mph]	160
Thrust [lbf]	236
Rotational Speed [RPM]	6552
Energy consumption [kWh]	24.57

Table 1.30: Cruise results.

Figure 1.64: Wing engine thrust and energy consumption as function of the cruise velocity.

Descent

The equation adopted to investigate the descent phase are Eq. 1.42, the same used in the climb section.

An analysis depending on the initial descent velocity is presented in Fig. 1.65 and Fig. 1.66. As clearly shown by Fig. 1.66 for cruise velocities lower than 160 mph is not possible to achieve a vertical descending velocity of -1,000 ft/min as it would require a negative thrust by the engines. For sake of consistency with the methodology proposed, the descent reference velocity is imposed at $V_{Descent} = 165$ mph, the first velocity enabling the airplane to match a descent rate of -1,000 ft/min. It's supposed a small acceleration commanded by the autopilot from V_{Cruise} to $V_{Descent}$ before starting the descent phase. The results are presented in Tab. 1.31.

The results of the analysis concerning the influence of the variation of the vertical velocity upon the performance parameters are presented in Fig. 1.67.

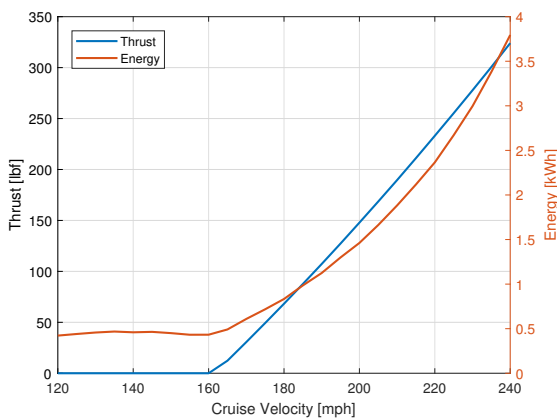


Figure 1.65: Thrust and energy requirement with respect to cruise velocity.

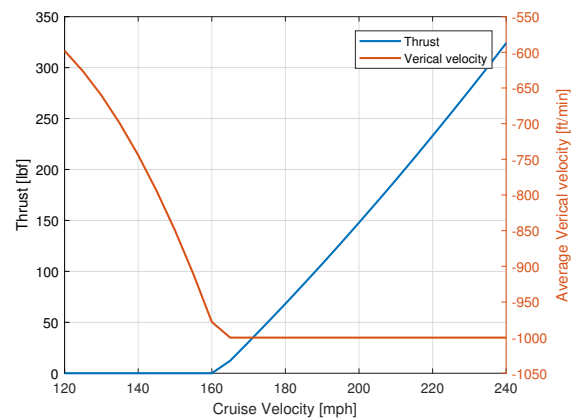


Figure 1.66: Maximum vertical velocities as function of cruise velocity.

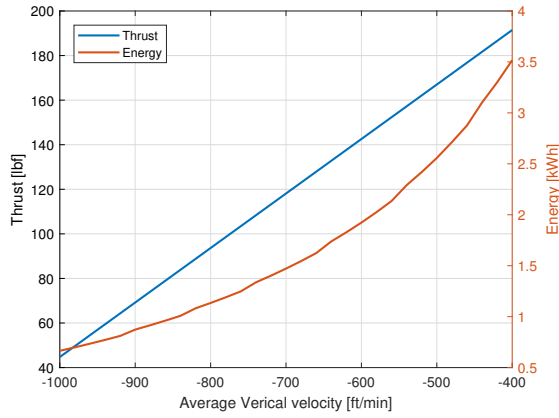


Figure 1.67: Thrust and energy requirement with respect to desired descending velocity at $V_{Descent}$.

Period [s]	87
Distance covered [mi]	3.98
γ [deg]	-4
Thrust [lbf]	12
Rotational Speed [RPM]	6178
Energy consumption [kWh]	0.5

Table 1.31: Descent results.

Transition to hover

During this phase, the E-VTOL changes its flight type, from horizontal to vertical. The wing engines thus tilt from $\Omega = \frac{\pi}{2}$ to $\Omega = 0$ and the canard engines are turned on and tuned to keep the aircraft elevation and to maintain the pitching moment balance. The equations of motion Eqs. 1.41 are, already presented in the Transient section.

Under the very same assumptions, the design parameter is the transition period T_{det} which directly influences the performance parameters; its impact upon the energy consumption is shown in Fig. 1.68. In order to reach quickly the vertical condition to start the breaking phase and not to overload the tilting motors of the wing engines, a de-transient period of $T_{det} = 6s$ is selected.

This segment is studied considering an horizontal velocity at the transition beginning of $V_{in} = 143$ mph and it is assumed to be reached after the descent segment by a correction commanded by the autopilot.

The thrust profiles are presented in Fig. 1.69 while the other important parameters are listed in Table 1.32.

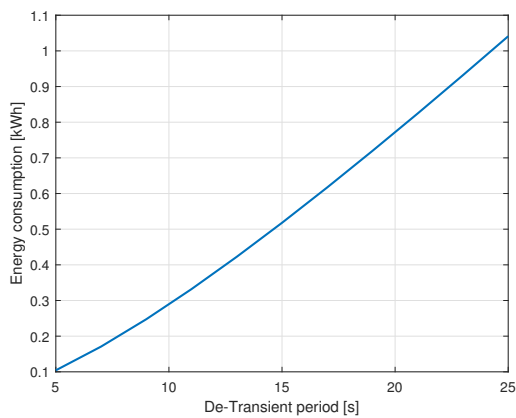


Figure 1.68: Energy consumption as function of de-transient period.

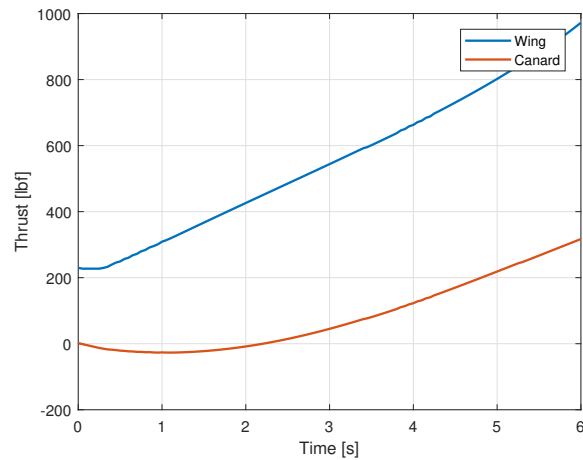


Figure 1.69: Wing and canard engine thrust profile (magnitude) as function of de-transient period.

As shown in Fig. 1.69, for a small amount of time, canard engines are supposed to deliver a negative thrust. As engines are not design to provide bi-directional thrust, this effect is assumed to be provided by a a reduction of the canard lift though elevator action.

Period [s]	6
Distance covered [mi]	0.22
Altitude variation [ft]	0
Final velocity [mph]	114
Final Lift [lbf]	2260
Energy consumption [kWh]	0.14

Table 1.32: De-transient results.

Braking

As stated in the previous section, at the end of the transition to hover phase the aircraft moves at $V_{FinalDetransient} = 114mph$. In order to achieve the vertical landing, it is necessary to brake the airplane using the canard air brakes and the drag produced by the wing engine duct once they are vertically oriented. This process must be achieved without loss of altitude and maintaining the attitude of the aircraft constant. The equations of motion are the following

$$\begin{cases} m\ddot{x} = -D - D_s - D_e & (1.43a) \\ m\ddot{y} = L + T_w + T_c - mg & (1.43b) \\ T_w l_w - D_e h_w + L_w L_{wp} = L_c l_{cp} + T_c l_c - D_s h_c & (1.43c) \\ L_w l_{wp} + T_w h_w = L_c l_{cp} & (1.43d) \end{cases}$$

Integrating Eqs. 1.43 until an horizontal velocity of $V_{fin} = 20mph$ returns wing and canard engine thrust profile as shown in Fig. 1.70. Once V_{fin} an active braking maneuver (high increase of the angle of attack over the stall angle), commanded by the auto-pilot, is assumed to be performed in order to definitively stop the E-VTOL. The active braking maneuver is not initiated earlier because the increase in the angle of attack required by the maneuver would result in the stall of the canard. It is worth underlining the influence of the different sources of drag during the time evolution of the braking maneuver as shown in Fig. 1.71.

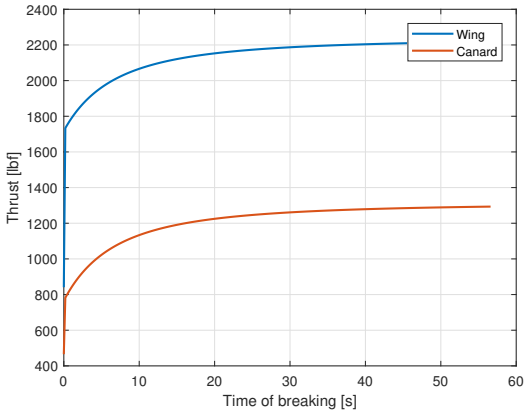


Figure 1.70: Wing and canard engine thrust (magnitude) profile during breaking.

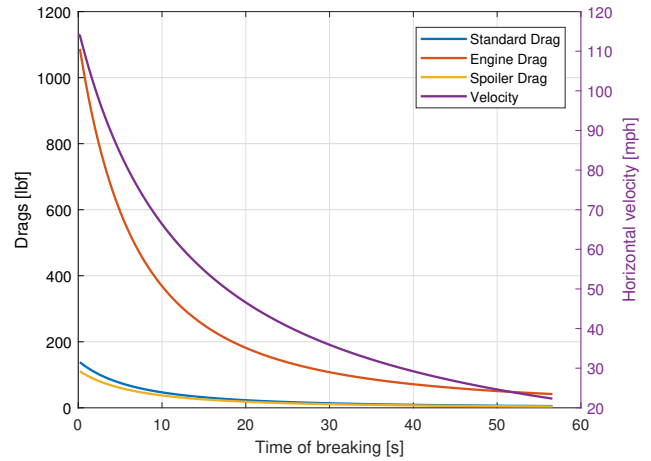


Figure 1.71: Trend of the different drags during the breaking manoeuvre with the horizontal velocity profile (in purple).

The Table 1.33 provide the remaining results:

Period [s]	56
Distance covered [mi]	0.72
Altitude loss [ft]	0
Final velocity [mph]	20
Energy consumption [kWh]	6.67

Table 1.33: Breaking results.

Hovering and Landing

Using the assumptions explained in the Take Off and Hovering section, the obtained results are presented in Table 1.27 with acceleration and deceleration segment inverted. Here are presented in Table 1.34 for sake of simplicity:

	Acceleration segment	Constant Speed segment	Deceleration segment
Accelerations [ft/s ²]	-0.89	0	0.89
Time periods [s]	1	58	1
Wing Thrust [lbf]	2,063	2,120	2,179
Canard Thrust [lbf]	1,391	1,430	1,469
Wing Rotational Speed [RPM]	7,461	7,566	7,672
Canard Rotational Speed [RPM]	7,663	7,774	7,882

Table 1.34: Landing results.

11.2 Reserve mission

The properties of the *Take-Off and Hovering*, *Transient*, *De-transient* and *Breaking* segments remains identical. Suitable values of the design parameters for *Climb*, *Cruise* and *Descent* must however be selected.

From the specific analysis conducted upon each segment, the following values are chosen in order to minimize the energy consumption of the reserve mission:

- **Climb:** Vertical velocity $V_{v_{climb}} = 1,000$ ft/min
- **Cruise:** Cruise equivalent velocity $V_c = 143$ mph
- **Descent:** Vertical velocity $V_{v_{desc}} = -750$ ft/min with an an horizontal velocity imposed to $V_{desc} = 103$ mph.

According to these choices, the result are listed in table 1.35

Total time [min]	5.7
Distance covered [mi]	7.4
Energy consumption [kWh]	22.9

Table 1.35: De-transient results.

11.3 Global Results

In order to have a global overview of the influence of every mission segment upon the mission performance parameters, the following graphs are presented.

Energy Consumption

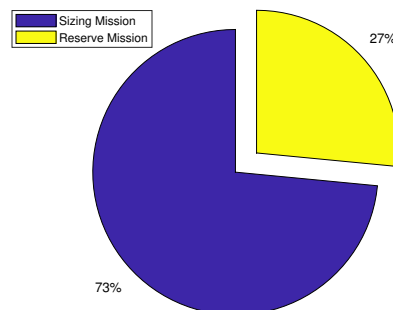


Figure 1.72: Relation between sizing mission energy and reserve mission energy.

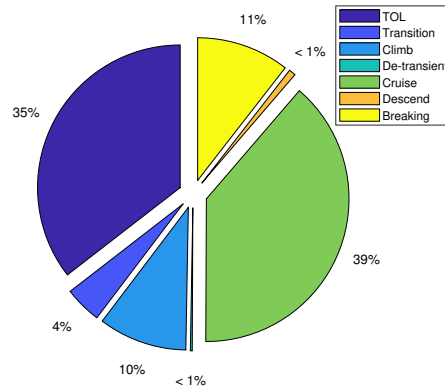


Figure 1.73: Partition of energy consumption during the sizing mission.

Time period and distance covered

The results refers to the sizing mission.

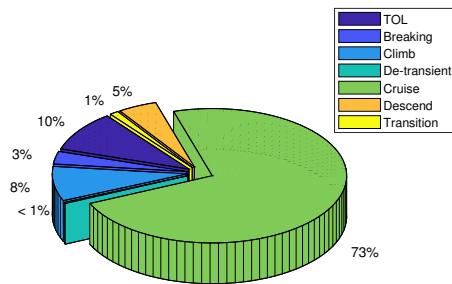


Figure 1.74: Phases time period.

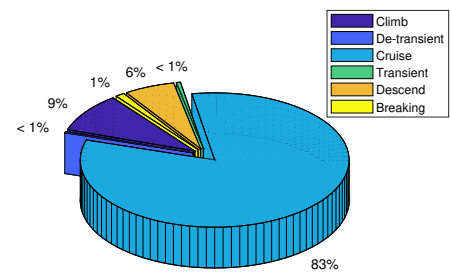


Figure 1.75: Phases covered distance.

11.4 Point Performances

This section is dedicated to demonstrate the performances of the Mistral Air Taxi during take-off, hover and transition at 5,000 ft MSL elevation with ISA + 10 conditions. The maximum speed requirement is not discussed as already demonstrated in *Cruise* analysis. In this section, "high and hot" conditions refer to atmosphere parameters computed at 5,000 ft MSL elevation with ISA + 10 while "sizing" conditions refer to 0ft elevation with ISA + 0 ones. The approach followed to analyse take off and hover and transition phases in "high and hot" conditions are equal to the related ones presented in the *Sizing mission* section.

"High and hot" take off and hover

The kinematics and dynamics parameters of the motion (distances, velocities, accelerations and thrusts) are imposed to be the same to the ones presented for the sizing conditions; this implies that the differences between the two atmospheric

conditions rely just on the engine related performances, i.e. RPM and energy consumption. The Tab. 1.36 resumes the results for this kind of situation (H) and compares them to the ones previously obtained at 0 ft MSL elevation with ISA + 0 (S).

	Acceleration segment	Constant Speed segment	Deceleration segment
S) Wing Rotational Speed [RPM]	7,575	7,566	7,566
H) Wing Rotational Speed [RPM]	8,276	8,275	8,265
S) Canard Rotational Speed [RPM]	7,777	7,774	7,773
H) Canard Rotational Speed [RPM]	8,495	8,495	8,495
Energy consumption[kWh]			
High and hot	12.3		
Sizing	11.25		

Table 1.36: Hovering results.

In the "high and hot" situation the engines are requested to increase their performances by increasing the RPM with respect to the sizing environment in order to provide the same thrust ; what is worth to be highlighted is that even in the "high and hot" situation the required RPM for the engine remains in the range of the allowable RPM of the electric motor driving their motion. It is thus possible to conclude that the aircraft is able to perform such a manoeuvre in the "high and hot" circumstances with an increase of energy consumption of 9.3 %.

High and hot transition

The effect of "high and hot" atmosphere condition upon transition phase are significant. By conducting the very same analyses performed in the sizing mission it results that selecting a transient period of $T = 20s$ it requests the engine to exceed their range of allowable RPM; the transition thus is impossible to be performed by imposing the same design parameter. In order to match the requirement and considering a balance between energy consumption and engine workload, a transition time for the "high and hot" transition is set to $T_{H\&HT\text{transition}} = 30s$.

The thrusts profile is shown in Fig. 1.76 where it's compare with the one obtained for the sizing atmosphere. The other important difference are listed in Tab. 1.37.

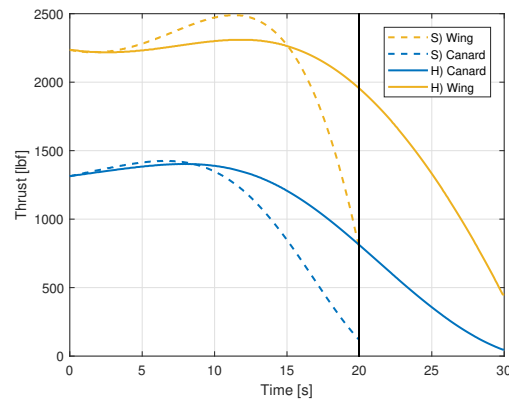


Figure 1.76: Thrust profiles (absolute value of thrust) during transitions; dashed lines represent the thrusts profile for sizing mission, solid lines are the "high and hot" ones.

	Sizing atmosphere	High and hot atmosphere
Period [s]	20	30
Distance [mi]	0.33	0.61
Altitude loss [in]	6.3	1.7
Final Velocity [mph]	141	156
Wing Peak [-]	111%	103%
Canard Peak [-]	108%	107%
ΔL [lbf]	115	42
Energy consumption [kWh]	2.66	4.82

Table 1.37: Transient results.

The impossibility of achieve the transition with the same transition period of sizing condition highlights the delicacy of this phase. This is pointed out also by the significant differences between the performance parameters of the two cases, as shown in Tab. 1.37. The reduction of the air density affects significantly the performance parameters as well as a longer time period; those affect considerably the energy consumption of the segment with an increase of the 81%, while tend to compensate their effects upon the workload of the engines whose peaks remain under acceptable and feasible limits.

12 Mechanism

The engine placed along the wing span are designed to be tilted from vertical to horizontal configuration and viceversa, as shown in Fig. 1.23. In order to achieve such a motion the system presented hereunder is analysed.

A generic mechanism can be divided in three main systems as shown in Fig. 1.77:

- **Engine:** it must provide mechanical power.

- **Transmission:** it must transfer the engine power to the user, and from a kinematical point of view establish a relation between the engine's and user's velocities.
- **User:** it uses the power coming from the engine in order to achieve a specific goal.

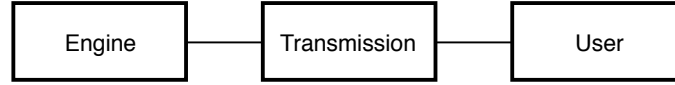


Figure 1.77: Mechanism block diagram.

The assumption of one degree of freedom implies that the position of all components can be described according to a single variable, which, in this case, refers to the rotation of the drive shaft. Moreover, it implies also that deformations are considered negligible.

In order to write down the differential equation governing the machine's behaviour it is useful to adopt the *Kinetic Energy Theorem*

$$\left\{ \begin{array}{l} \Pi = \frac{dE_k}{dt} \end{array} \right. \quad (1.44a)$$

$$\left\{ \begin{array}{l} \Pi = W_e + W_t + W_u \end{array} \right. \quad (1.44b)$$

$$\left\{ \begin{array}{l} E_k = E_{ke} + E_{ku} \end{array} \right. \quad (1.44c)$$

where W_e stands for all the forces and moments (except inertia ones) acting on the engine side, W_u for all the ones acting on the user's side and W_t the power loss in the transmission due to frictions and internal resistances.

Starting from Eqs. 1.44 the first step is to set up a good approximation model for the engine dynamics. In order to do so, each single engine is modeled considering a massless rigid beam of length l with a tip mass M condensing the total weight of the engine itself and the ducted fan.

$$J_e = Ml^2 \quad (1.45)$$

l value is chosen in order to condense the entire mass in the centre of the ducted fan cross section.

Motion definition

Once the user is properly modelled, it is necessary to define the kinematics of the motion to compute the design parameters of the system, i.e. the torque and the power needed.

The motion is divided into three segments:

- **Acceleration segment** defined by the angular velocity \dot{w}_1 and a time period Δt_1 .
- **Regime segment** defined by the regime velocity ω_r and a time period Δt_r .

- **Deceleration segment** defined by the angular deceleration $\dot{\omega}_2$ and a time period Δt_2 .

which transposed into equation, considering as approximation that the acceleration and deceleration segments behave the same way, reads

$$\begin{cases} \frac{1}{2}\dot{\omega}_1\Delta t_1^2 + \omega_r\Delta t_r + \omega_r\Delta t_2 - \frac{1}{2}\dot{\omega}_2\Delta t_2^2 = \frac{\pi}{2} \\ \Delta t_1 + \Delta t_r + \Delta t_2 = T \\ \Delta t_1 = \Delta t_2 \\ \dot{\omega}_1 = \dot{\omega}_2 \end{cases} \quad (1.46)$$

From those considerations it's possible to reduce the mechanism to a one degree of freedom system, parameterizing all the variables as function of ω_r ,

$$\begin{cases} \Delta t_r = \frac{\pi}{\omega_r} - T \\ \Delta t_1 = T - \frac{\pi}{2\omega_r} \\ \dot{\omega}_1 = \frac{\omega_r}{\Delta t_1} \end{cases} \quad (1.47)$$

Taking as design condition the transition to hover phase of the aircraft mission, developed in details in the *Performance Analysis* section, a total time of $T = 6s$ is set and the rotational velocity ω_r is imposed equal to 0.31 [rad/s].

It's thus possible to determine the kinematics characteristics of the system whose value are presented in Fig. 1.78.

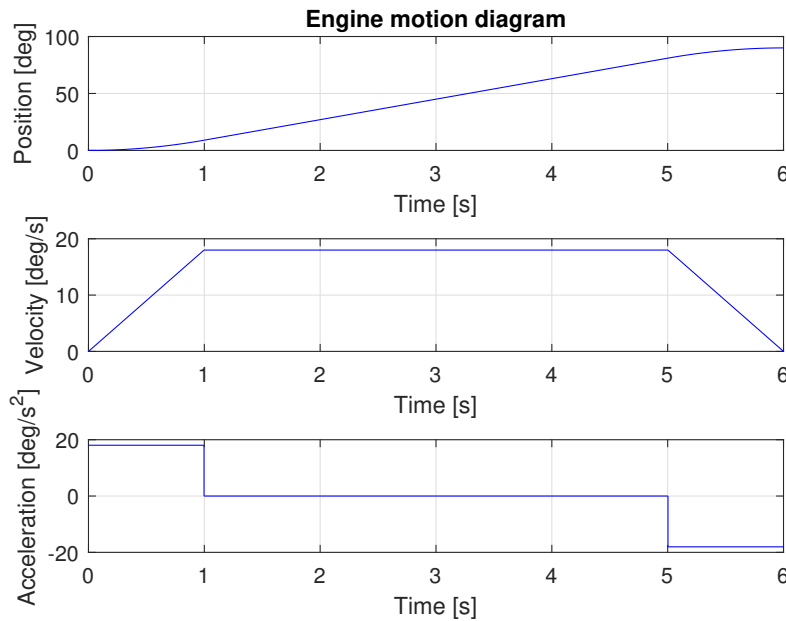


Figure 1.78: Engine motion diagram: from the top to the bottom 1) position as function of time 2) angular velocity as function of time 3) angular acceleration as function of time.

Motor selection

It was decided to install a complete system for each set of seven engines. It is thus required to install two separate driving system on-board of the aircraft, one for each half-wing.

The requirements in terms of power P , required moment M and ω_r for a cluster of seven wing engines are presented in table 1.38. Those specifications together with weight and volume considerations tighten the range of admissible electric motors to be installed.

A market analysis has been performed and the *Oriental Motor* company appears as one of the most advanced company because of its high-level technology products and market share. The motor and transmission assembly BLM5200HPK-5KV450S is chosen from its product list according to the criteria previously explained. The engine characteristics are shown in Tab. 1.39 and the systems installation is highlighted by a red box in Fig. 1.79

P [W]	25
M [lbfm]	109
ω_r [rad/s]	0.31

Table 1.38: Engine dynamics parameter for a cluster of seven engines.

Total weight [lb]	26.5
Total volume [ft^3]	0.18
Engine power [kW]	0.2
Output Moment [lbfm]	102-146

Table 1.39: From the motor and transmission selection, sizes and system parameter are presented.

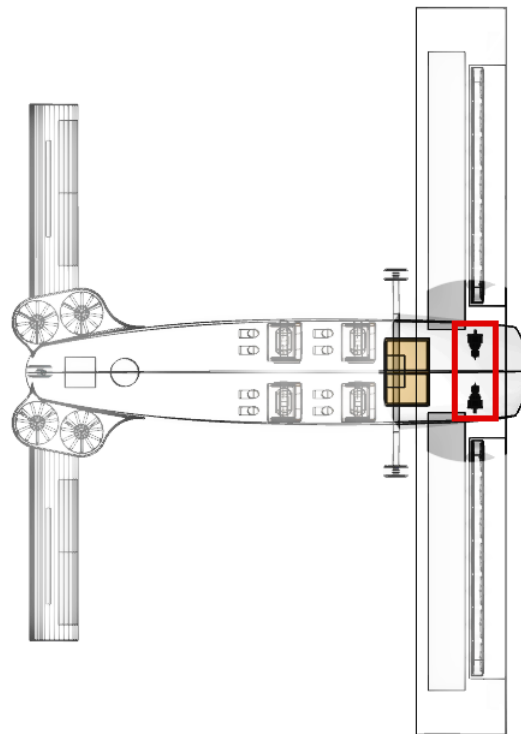


Figure 1.79: Tilting system installation.

13 Trade-off study

13.1 Wing characteristics

The wing is one of the main component of an aircraft. As such, it should be properly designed. The objective of this section is to analyse how the Mistral Air Taxi design is affected when important wing parameters such as the aspect ratio and the surface area are modified by 10%. The effect of taper is negligible as explained in the wing design section. Also, the swept angle is zero since it is not appropriate for Mistral Air Taxi subsonic flight conditions. The following trade-offs will indicate whether the chosen wing's characteristics are optimal. The results are presented in table 1.40 using the reference wing with an aspect ratio of 8 and a surface of 129.167 ft².

Aspect ratio

A bigger aspect ratio increases the wing span. As a result, there is more available space for the engines and control surfaces at the expenses of compactness(longer wingspan). Nevertheless, the chord will shrink and increase the effect of the engines on the wing's lift generation. Notice that the calculated $C_{L,w}$ does not take into account the effect of the engines, advanced CFD simulations should be performed in order to evaluate the real effect. The stability is enhanced but maneuverability is reduced (more prone to stall), this is not recommended for the urban environment. The presence of multiple flying objects in a reduced space, between buildings and above crown areas makes aircraft's reaction time and safety crucial. Drag is reduced but with a negligible effect on energy requirements and GTOW and the aircraft can withstand higher load factor.

A reduced aspect ratio provides the opposite characteristics with respect to the increase of aspect ratio. However, shorter wingspan complicates the positioning of engines and control surfaces, the aircraft is less stable and withstand lower load factor, the weight increases as a consequence of a major total drag and energy requirements. Since the variation with respect to the actual configuration are very small, the reference configuration is maintained.

Wing surface

The reduction of the wing surface has no interest since the positioning of the engines and wing surfaces is more difficult. Moreover, the drag, the GTOW and the total energy requirements increases and the load factor is strongly decreased, even if there is an interesting positive effect on lift generation, compactness and manoeuvrability.

In the other hand, an increase of the wing surface provides more space but with a huge lose of lift generation and an increase in drag, GTOW and energy requirements. Moreover, a bigger wingspan and a larger load factor impinges a bigger stiffness and a more resistant structure which means better material or/and heavier wings and also the aircraft is more prone to stall.

The reference configuration is maintained since the it generates less drag and thus less energy requirements, offers enough space for the engines and control surfaces and the difference between the different configurations do not worth the changes of the wing's characteristics.

	AR8 and S_w 107.64	AR-10%	AR+10%	S_w -10%	S_w +10%
b_w	32.15 ft	-6.46	+6.14	-8.72	+8.01
c_w	4 ft	+6.91	-5.72	-8.71	+8.01
GTOW	3,470.1 [lbs]	+0.0815	+0.027	+0.0416	+0.5606
$C_{L,w}$	0.3255 [-]	0	0	+20	-14.29
D_{TOT}	222.4 [lbf]	+1.67	-1.24	+1.88	+0.46
Stability margin κ_n	9[-]	-22.22	+33.33	+16.67	-28.89
Total energy requirements	78.13 [kWh]	+0.86	-0.64	+0.63	+0.45
Limit load factor n_{lim}	4.47 [-]	-3.30	+2.86	-7.97	+6.8
Equivalent stall velocity V_{S1}	78.73 [kts]	+0.99	-0.74	+3.70	-2.96

Table 1.40: Trade-off analysis for the aspect ratio of the wing. The values represent the % of variation with respect to the reference configuration obtained after the design.

14 Cost analysis

So far, the design of the Mistral Air Taxi has been detailed. The objective of this section is to study the costs (development, production and operating) associated with the aircraft. In turn, those costs will greatly affect the competitiveness of the aircraft. Indeed, when looking for new aircraft, a company will be offered many different options, all of which will be very similar in terms of performance as manufacturing companies will only answer a request for proposals they can meet. Therefore, one of the main ways for the costumer to decide on which aircraft to choose is the cost.

In this study, the costs will be separated into three main sections:

- The research, development, testing and certification costs (RDTC costs) which include all the costs linked to the design of the aircraft (engineering hours), the tooling development and the testing performed for certification. These costs are mostly not dependant on the number of aircraft produced.
- The production costs which include the labor costs as well as the costs of acquiring the materials, parts and components (e.g. electric motors, avionics, etc.) for the aircraft. Obviously, these costs heavily depend on the number of units produced (economics of scale).
- The operating costs which include all the costs related to the everyday operation of the aircraft: personnel (ground crew, back office personnel), energy cost (or in our case electricity), maintenance, insurance and miscellaneous charges such as taxes. Even though, these costs are at the expense of the customer, it is important to estimate them. Indeed, lower operating costs could justify a higher selling price.

14.1 Method used

The method used to estimate the cost of the program is based on the adaptation of the DAPCA-IV method by professor Eastlake of Embry-Riddle university [57]. The DAPCA-IV is a statistical method developed by the RAND corporation to assess the development costs of a new aircraft. The method is mainly based on military aircraft and is thus not well adapted to general aviation. However, the Eastlake variant is well suited for general aviation. The method used is presented in [57].

The method estimates the workload for the different parts of the development and production of the aircraft (the engineering, tooling and manufacturing hours) based on simple aircraft parameters such as the structural weight or its maximum speed. Then based on the cost of labor, a rough estimate of the cost can be calculated. It is interesting to note that since the method provides an estimate of the workload facing the developers, it could also be used for planning purposes (for instance, estimating an entry-in-service date).

As this method is calculated assuming the cost of living in the year 2012, a transform CPI factor between years 2012 and 2028 is used to adjust all results to the latter. The estimated CPI of 2028 can be found in [58].

14.2 Market size and potential

The Mistral Air Taxi is expected to enter service in 2028. It is necessary to estimate the potential of the market in order to determine the number of aircraft that must be produced over a given period.

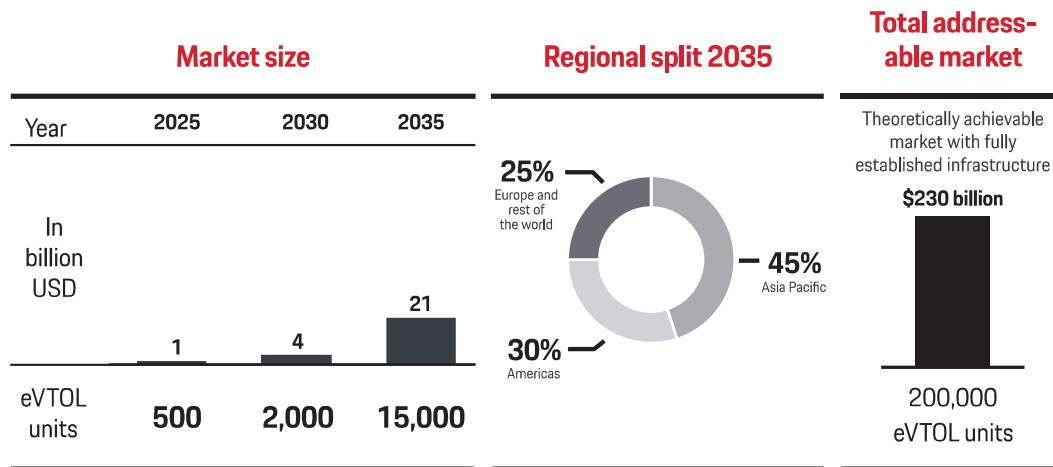


Figure 1.80: E-VTOL market size evolution and regional split between the year 2025 and 2035 from [59].

As explained in [59], the market for passenger E-VTOL is expected to become increasingly important after 2025. It is forecast that the worldwide fleet of E-VTOL will reach 15,000 units by the year 2035. With an entry in service in 2028, the Mistral Air Taxi will be launched at exactly the right time to meet the demand. That being said, it has been decided to set an objective of 2,000 units sold on a 5 year period (from 2028 to 2033). This amounts to an average of 400 units per year. This objective might seem ambitious for the years prior to 2030. But it does seem reasonable for latter years.

Moreover, the fact that 45% of the E-VTOL will be found in Asian countries (Fig. 1.80), combined to the lower cost

of labor and the presence of many industries in Asia, amply justifies the offshoring of manufacturing to Asia. Looking at recent studies comparing the cost of labor in different countries (see Fig. 1.81), the proposed location for manufacturing is Vietnam. This offshoring of the production is expected to sharply decrease the cost of the aircraft. It must however be noted that Asian imports might be facing tariffs (giving a number would be pure speculation as the year 2028 is still far-off, therefore this will not be taken into account in this analysis). This would reduce the benefit of the offshoring for the aircraft sold in USA and in Europe.

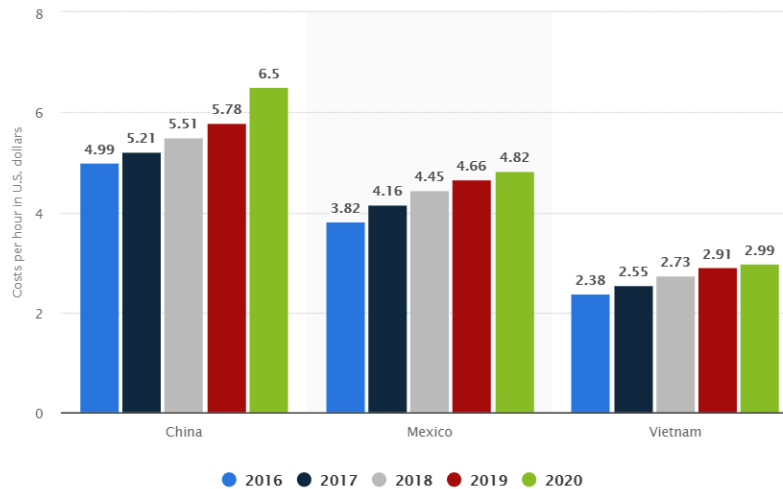


Figure 1.81: Comparison of the labor cost in different countries [60].

14.3 Development and manufacturing costs

Using the formulas presented in [57], an estimate for the cost of the program can be found. The results are presented in the tables hereunder.

	Man-hours	Rate [\$/hr]	Total cost [\$]
Engineering	798,008	90	206,622,000
Development support	/	/	6,418,000
Flight test operations	/	/	616,000
Tooling	538,542	60	92,960,000
Total cost to certify			306,616,000

Table 1.41: Breakdown of the certification cost for the aircraft.

In this analysis, the costs related to the construction of a factory (land or building costs for instance) are not considered. It is assumed that these costs are at the expense of the third party manufacturer that will be chosen for the production of the aircraft.

The development and certification costs have been estimated. They amount to approximately 153,308 \$ per aircraft. The production costs must then be accounted for in order to determine a selling price. The results obtained using the formulas found in [57] are presented in Table 1.42. A detailed breakdown of the cost of the avionics associated with the autonomous system is available in the appendix.

	Man-hours	Rate [\$/hr]	Total cost [\$]	Cost per unit [\$/unit]
Certification	/	/		153,308
Manufacturing labor	4,265,836	5	61,362,000	30,681
Quality control	/	/	11,566,000	5,783
Materials/Equipment	/	/	100,718,000	50,359
Fixed landing gear discount	/	/		-7,500
Avionics	/	/		9,746
Engines	/	/		7,731
Propellers	/	/		11,379
Battery	/	/		32,028
Liabilities insurance	/	/		35,192
Total cost	/	/		328,707
Selling price with 15 % margin	/	/		378,013

Table 1.42: Breakdown of the total cost for one aircraft.

Using the objective of 2,000 aircraft produced over the first 5 years, the total cost per unit is found to be 328,707 \$. Assuming a 15% profit margin, the program acquisition cost is 378,013\$ compared to the flyaway cost of 103,743\$. It must be noted that in Table 1.42, the price for the fixed landing gear is negative because the method used was developed for airplanes with retractable landing gear. Fixed landing gear are cheaper, therefore an estimated amount of 7,500 \$ is subtracted from the price of each unit.

14.4 Break-even analysis

The certification costs are independent of the number of units produced. This means that the cost of an aircraft will depend on the total number of units produced. The price of one Mistral Air Taxi as a function of the total number of aircraft produced is shown in Fig. 1.82. As can be observed, the unit costs sharply decreases when the number of unit produced increases. From more than 2 M\$ per unit when only 100 aircraft are build, the production cost decrease to just over 477 K\$ when 1,000 airplanes are built.

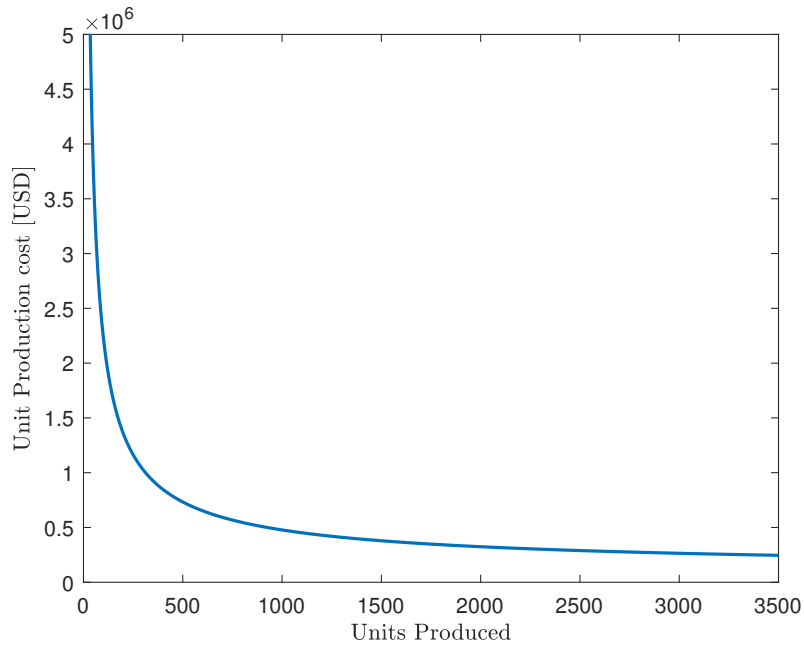


Figure 1.82: The development cost in millions of dollars as a function of units produced.

The next logical step is to perform a break-even analysis in order to determine how many aircraft must be sold before the program starts making profits. The certification cost including the cost of engineering, development support and flight test operations and tooling are considered as the total fixed cost. The variable costs include the labour for manufacturing, the materials, the batteries and motors. The break-even point is defined as the point where revenue equals the costs incurred. In this case, this point is found to be when 1,512 units are sold. The selling price is obtained assuming a 15% profit margin.

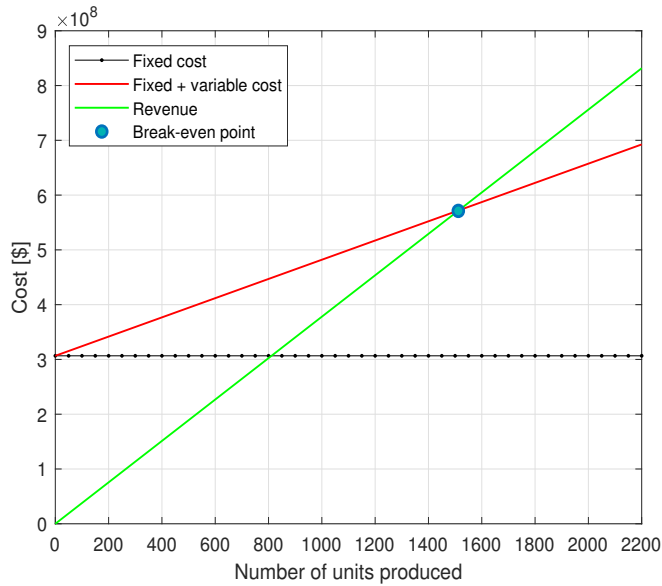


Figure 1.83: Fixed cost, total cost and revenue as a function of the number of units produced.

14.5 Operating costs

As explained previously, it is important to obtain an estimation of the operating costs of the aircraft. We will assume here an annual flight time of 1,500 hours (which corresponds to 4 hours of flight per day). The elements to take into account for the operating costs are the following:

- Energy costs: usually this energy refers to fuel costs. In the case of E-VTOL, this refers to the price of electricity. Of course, it is assumed here that the batteries are recharged using electricity from the public grid.
- Maintenance, overhaul and inspection costs: the maintenance of an electric engine is simpler than of a turbojet or piston engine. Therefore, it is assumed that 0.1 hour of maintenance is required for each flight hour. The same goes for the overhaul cost which will definitely be smaller than for piston engines. It was also assumed that the rate of a certified mechanics was 50 \$/hr. Finally, inspection costs are assumed to be 500 \$/year.
- Insurance costs: aircraft are usually insured based on their values.

The results obtained using the formulas found in [57] are presented in Table 1.43

	yearly cost [\$/year]	cost per flight hour [\$/hr]
Energy	30,778	20.52
Maintenance	9,450	6.3
Overhaul	17,010	11.34
Inspection	630	0.42
Insurance	8,031	5.35
Total:	65,899	43.93

Table 1.43: Breakdown of the operating cost per aircraft.

Taking all the above into account, it was calculated that the operating cost of the Mistral Air Taxi is 43.93 \$ per flight hour. This figure is most likely lower than the real operating cost as there are other expenses that must be accounted for. Even though the aircraft is autonomous, ground operators will be involved. It can be imagined that there will be some boarding agents or people responsible for flight planning. The exact organization is left to the final customer and cannot be known in advance. Therefore this cost was not taken into account. Moreover, there could be extra costs for landing, for parking the aircraft whilst it is not used or for liability insurance. A recommended price per passenger for the typical mission is estimated at 33 \$ per seat(see Appendix 4).

14.6 Comparison with other means of transport

In order to assess the competitiveness of our aircraft, a comparison between several different means of transportation is performed. The trip on which the comparison is performed is from New York to New Haven (see Fig. 1.84) and assuming

the cost of living in the year 2019. All sources are listed in Appendix 4.

Vehicle type	Travel time [min]	Seats	Price [\$]
Mistral Air Taxi	30	1-4	110
UberBLACK	105	1-4	330
Bus	175	1	33
Train	102	1	208
Small Prop Aircraft	28	1-3	1570

Table 1.44: Comparison of different means of transport in terms of travel time and cost for a trip from New York to New Haven.

It is clear that the Mistral Air Taxi offers the best compromise between cost and travel time between those 2 cities. Taxis only offer a longer and costlier trip, and while other aircraft can provide the same travel time, their cost is too high for them to be competitive.

A second example of intra-city travel is also presented. The chosen trip is from Newark Liberty International Airport to John F. Kennedy International Airport (see Fig. 1.85), which are the main airports in New York city. As the trip is much shorter, not all means of transport from the previous table were retrieved. Once again, it appears that the Mistral Air Taxi achieves the lowest travel time at a very competitive operating cost.

Vehicle type	Travel time [min]	Seats	Price [\$]
Mistral Air Taxi	14	1-4	51
UberBLACK	56	4	90
Helicopter Transfer	24	1	390

Table 1.45: Comparison of different means of transport in terms of travel time and cost for a trip from Newark to Kennedy Airport.

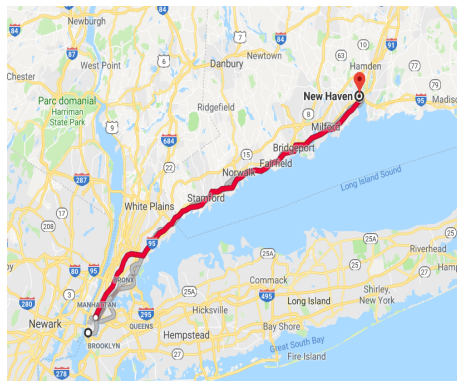


Figure 1.84: Trip between New York and New Haven[61].

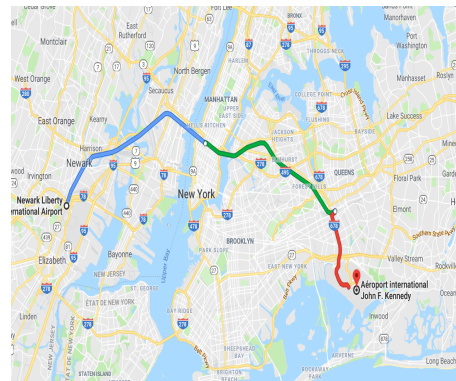


Figure 1.85: Trip between Newark and Kennedy airports [61].

15 Conclusion

The report presented the conceptual and preliminary design of the Mistral Air Taxi. The final objective was to establish a solid, FAA compliant configuration which was able to satisfy to the RFP of the AIAA.

In real life, design experts spend few days to finish the conceptual and preliminary stages. The alacrity is based on years of experience, simple designing tool and numerous assumptions. Major results of this project also rely on approximations. Moreover, difficulty is added by the nonexistence of similar aircraft to use as reference. The major assumptions are done when given characteristics such as battery energy density are anticipated to be existing in 2028. Moreover, the effect of the engines on the wing should undoubtedly be improved, the effect of this positioning on the lift generation is unclear. The autonomous system is based on suppositions extracted for the car industry.

Methods Even if there was no accurate data on E-VTOL aircraft, the GA aircraft data provided by reference books such as Raymer and Roskam were sufficient. The design was pushed further thanks to a more extensive analysis in an effort to minimize the influence of the simplifications and hypotheses taken. The principal objective was to optimize the weight since the use batteries penalized the performance of the aircraft.

From the trade-off analysis it was concluded that the design phase has been performed correctly. The performance analysis showed that the aircraft is able to accomplish the missions and the cost analysis demonstrated the economical viability of such aircraft.

Results The final result of this work is a four-seater E-VTOL aircraft that fully meets the imposed requirements. Geometrical parameters for the aircraft were fixed with one main objective in mind : enhance the customer's experience. As such, the main cabin is spacious and offers great travel comfort. The configuration includes a canard and a distributed propulsion. The high wing configuration offers great stability margin comprised between 8 and 18%. Moreover, it was demonstrated through a thorough analysis of the aircraft performance that the design is fully compliant with the RFP. It can fly all the segment of its mission. It is also able to fulfill its mission under "high-and-hot" conditions.

Bibliography

- [1] United Nations, Department of Economic and Social Affairs, Population Division. *World Urbanization Prospects: The 2014 Revision, Highlights*. 2014. (ST/ESA/SER.A/352).
- [2] Swadesir Lewis, Bil Ceas. *Urban air transportation journey time comparison for Melbourne metropolitan area*
- [3] Binder Robert B., Garrow Laurie A et al. *If You Fly It , Will Commuters Come ? Predicting Demand for eVTOL Urban Air Trips*. 2018. 2018 Aviation Technology, Integration, and Operations Conference.
- [4] Michael L. Anderson Maximilian Auffhammer. *Pounds That Kill: The External Costs of Vehicle Weight*
- [5] AIAA. *Request for proposal: Electric Vertical Takeoff and Landing Aircraft*. 2018-2019 Graduate Team Aircraft Contest.
- [6] Noels, Ludovic. *Aircraft Design: Introduction to Conceptual design* Course notes. Uliege. 2013.
- [7] Raymer Daniel, P. *Aircraft Design: A conceptual approach* AIAA Education series. 1999.
- [8] Jean Hermetz, Michael Ridel, Carsten Doll. *Distributed electric propulsion for small business aircraft a concept-plane for key-technologies investigations*. ICAS 2016, Sep 2016, DAEJEON, South Korea.
- [9] K. Sampigethaya and R. Poovendran. *Cyber-physical system framework for future aircraft and air traffic control*. In 2012 IEEE Aerospace Conference.
- [10] N. R. Council. *Autonomy Research for Civil Aviation: Toward a New Era of Flight*.
- [11] Vectored Thrust. (2019, January 21). Retrieved February 7, 2019, from <http://evtol.news/vectored-thrust/>
- [12] D. Finger, F.Götten, C. Braun et al. *Initial Sizing for a Family of Hybrid-Electric VTOL General Aviation Aircraft*.67. Deutscher Luft-und Raumfahrtkongress DLRK 2018.
- [13] Carreyette, J. F. (1950). *Aircraft wing weight estimation*. Aircraft Engineering, 22(1), 8–11.
- [14] ROSKAM, Jan. *Airplane design*. DARcorporation, 1985.
- [15] G. Dimitriadis, L. Noels. *Aircraft Design: Aerodynamics* Lecture notes. Uliege. 2017.
- [16] George Jacobellis, Alex Angilella, Jean-Paul Reddinger, Andrew Howard, Matthew Misorowski, Michael Pontecorvo, Jayanth Krishnamurthi. *The Emperor UAV: Executive Summary*. 31st Annual American Helicopter Society Student Design, Competition: Graduate Submission.
- [17] Osgar John Ohanian III. *Ducted Fan Aerodynamics and Modeling, with Applications of Steady and Synthetic Jet Flow Control*. Faculty of the Virginia Polytechnic Institute and State University May 4th, 2011, Blacksburg, VA.
- [18] Yun Jiang, Bo Zhang and Tao Huang. *CFD Study of an Annular-Ducted Fan Lift System for VTOL Aircraft*. UAV Research Institute, Northwestern Polytechnical University, China. (ISSN 2226-4310)
- [19] Dyer, K.G. *Aerodynamic Study of a Small, Ducted VTOL Aerial Vehicle*. Master’s Thesis, Massachusetts Institute of Technology, Department of Aeronautics and Astronautics, Cambridge, MA, USA, 2002; pp. 31–49.
- [20] Bahram Raeisi. *Aerodynamic study of tilting asymmetrical ducted fans mounted at the wing tips of a vtol uav*. Toronto, Ontario, Canada, 2016.
- [21] Thomas LAMBERT. Liège Université, Aeroelasticity and experiment aerodynamics lab (ULiege-AEA). Modified version of the BEMT_VPM code of A.M. Harrington from the university of Maryland. Original version : <https://sourceforge.net/projects/bemt/>
- [22] B. Greschner, C. Yu, S. Zheng, M. Zhuang, Z. J. Wang and F. Thiele. *Knowledge Based Airfoil Aerodynamic and Aeroacoustic Design*.
- [23] Mounir Zeraoulia, Mohamed Benbouzid, Demba Diallo. *Electric Motor Drive Selection Issues for HEV Propulsion Systems: A Comparative Study*. IEEE VPPC’05, Sep 2005, Chicago, United States.
- [24] Ghassan Zubi, Rodolfo Dufo-López, Monica Carvalho, Guzay Pasaoglu. *The lithium-ion battery: State of the art and future perspectives*.

- [25] RECHARGE aisbl. (The European Association for Advanced Rechargeable Batteries) *E-mobility Roadmap for the EU battery industry*. July 2013
- [26] Michael Kreimeier. *Evaluation of On-Demand Air Mobility Concepts with Utilization of Electric Powered Small Aircraft*. Von der Fakultät für Maschinenwesen der Rheinisch-Westfälischen Technischen Hochschule Aachen. 22. März 2018
- [27] US Department of Defense Office of the Secretary of Defense, *Unmanned Aircraft Systems Roadmap 2005-2030* (2005)
- [28] Jeffrey D. Sinsay, Brendan Tracey and Juan J. Alonso, Dean A. Kontinos, John E. Melton and Shon Grabbe. *Air Vehicle Design and Technology Considerations for an Electric VTOL Metro-Regional Public Transportation System*.
- [29] Claire Curry. Blomberg New Finance. *Lithium-ion Battery Costs and Market. Squeezed margins seed technology improvements & new business models*. July 5, 2017.
- [30] Michael Dudley. *Promising Electric Aircraft Drive Systems. EAA Electric Aircraft World Symposium*. 2010.
- [31] Kim, Hyun D., Perry, Aaron T., and Ansell, Phillip J. *A Review of Distributed Electric Propulsion Concepts for Air Vehicle Technology*. (AFRC-E-DAA-TN56442) Jul 12, 2018
- [32] Armstrong, M., Ross, C., Blackwelder, M. and Rajashekara, K. *Trade Studies for NASA N3-X Turboelectric Distributed Propulsion System Electrical Power System Architecture*. SAE Int. J. Aerosp. 5(2):2012, doi: 10.4271/2012-01-2163
- [33] Society of Automotive Engineers. *Automation Levels for cars*.
- [34] R.J. Roosien and T.M. van Birgelen. *Introducing automation in aviation. Lessons learned for self-driving vehicles*. December 2017.
- [35] Captain Mark Chesney and Wg Cdr Ian Shaw. *ICAO RSG-PA. 4th Pan-American Aviation Safety Conference*. December 2017.
- [36] National Highway Traffic Safety Administration. *Traffic Safety Facts 2014*.
- [37] Federal Highway administration for US Department of Transportation *Average Annual Miles per Driver by Age Group* <https://www.fhwa.dot.gov/ohim/onh00/bar8.htm> [On-line 29/4/2019].
- [38] Multiple. *AERO magazine QRT02/07*. The Boeing Company.
- [39] Heather Bradshaw-Martin, Catherine Easton. *Autonomous or driveless cars and disability: a legal and ethic analysis*.
- [40] Uber. *Fast-Forwarding to a Future of On-Demand Urban Air Transportation*.
- [41] N. Oliver, T. Calvard, and K. Potočnik *The tragic crash of flight AF447 shows the unlikely but catastrophic consequences of automation..* Harvard Business Review. <https://hbr.org/2017/09/the-tragic-crash-of-flight-af447-shows-the-unlikely-but-catastrophic-consequences-of-automation>. [On-line 7/2/2019].
- [42] Ivo Emanuilov. *Autonomous Systems in Aviation: Between Product Liability and Innovation*.
- [43] S. Bhattacharyya, D. Cofer, D. Musliner, J. Mueller, and E. Engstrom. *Certification considerations for adaptive systems*.
- [44] Office of the secretary of Defense. *Unmanned aircraft system roadmap. 2005 - 2030*.
- [45] *Autonomous Systems* <https://www.nasa.gov/feature/autonomous-systems>. [On-line 29/4/2019].
- [46] N. Vinothini and S. Sorna Lakshmi *An embedded real-time system for autonomous flight control*.
- [47] Mark Ballin. *ARMD Strategic Thrust 6: Assured Autonomy for Aviation Transformation*.
- [48] D. Danks and A. J. London. *Regulating Autonomous Systems: Beyond Standards*.
- [49] Yasmina Bestaoui Sebbane. *Smart Autonomous Aircraft: Flight Control and Planning for UAV*.

- [50] Parker D. Vascik, Hamsa Balakrishnan, R. John Hansman. *Assessment of air traffic control for urban air mobility and unmanned systems.*
- [51] Torenbeek Egbert, P. *Synthesis of Subsonic Airplane Design* Kluwer Academic Publishers. 1982
- [52] T. H. G. Megson. *Aircraft Structures for Engineering Students*. 6th Edition.
- [53] Office of the Federal Register National Archives and Records Administration. *Code of Federal Regulations: Title 14 Aeronautics and Space* Ed. 2017. Section 23.335 Paragraph (b)(4)(ii) and (iii).
- [54] Marco Aurelio Rossi et al. *Design and analysis of a composite fuselage*
- [55] *USAF Stability and Control Data Compendium (DATCOM)*
- [56] Brian D. O. Anderson and John B. Moore. *Optimal Control: Linear Quadratic Methods* - Dover Books - 1st edition (April 30, 2004).
- [57] Gudmundsson, Snorri. *General aviation aircraft design: Applied Methods and Procedures*. Butterworth-Heinemann, 2013.
- [58] Oregon State University. *Inflation Conversion Factors for years 1774 to estimated 2028*. Retrieved on April 2019, from <https://liberalarts.oregonstate.edu/spp/polisci/research/inflation-conversion-factors>.
- [59] Doppler, Steffan et al. . *The futur of vertical mobility: Sizing the market for passengers, inspection, and goods services until 2035*. Porsche Consulting, 2018.
- [60] Statista, *Manufacturing Labor Costs per Hour: China, Vietnam, Mexico 2016-2020*. Retrieved on March 2019 from www.statista.com/statistics/744071/manufacturing-labor-costs-per-hour-china-vietnam-mexico/.
- [61] *Map of New York and the surrounding states*. Google maps. 2019.
- [62] Uber's price estimator. Retrieved on May 2019, from <https://www.uber.com/us/en/price-estimate/>.
- [63] Greyhound lines. Retrieved on May 2019, from <https://www.greyhound.com/>.
- [64] Amtrak. Retrieved on May 2019, from <https://www.amtrak.com/home.html>.
- [65] Privatefly. Retrieved on May 2019, from <https://www.privatefly.com/us/private-jet-charter/private-jet-charter>.
- [66] TaxiFareFinder. Retrieved on May 2019, from <https://www.taxifarefinder.com/>.
- [67] BLADE Airport. Retrieved on May 2019, from <https://blade.flyblade.com/p/airport>.
- [68] New York Helicopter. Retrieved on May 2019, from <https://www.newyorkhelicopter.com/>.
- [69] Advance Propulsion Centre (APC) UK *Roadmaps Explored – Understanding the battery challenges from chemistry to recycling*. (Electrical Energy Storage workshop)
- [70] Aditya Jain. *Cost of a Self-Driving Car's Components*. www.automotiveelectronics.com/cost-of-components-of-a-self-driving-car.

A Appendix

1 Batteries

Battery type	Strengths	Weaknesses
Lead-acid	<ul style="list-style-type: none"> + Relatively low initial cost + Mature technology + Large number of manufacturers worldwide + Reliance on abundant cheap materials + Satisfactory round-trip efficiency + No memory effect + Low self-discharge rate + Proven efficiency of recycling schemes + Outstanding specific energy and power + Long calendar and cycle lives + High roundtrip efficiency + Low O&M requirements + Satisfactory operating temperature ranges + High reliability + Technological diversity; several chemistries + Intensive global R&D efforts + Chemistries with eco-friendly materials available + Reasonable self-discharge rate + Relatively fast recharge 	<ul style="list-style-type: none"> - Modest specific energy and power - Short cycle life - High O&M requirements - Performance sensitive to temperature - Limited reliability - Long charging time - Safety concerns; gas release - Reliance on hazardous lead^a - High initial cost - Advanced BMS required - Safety concerns; thermal runaway incidents - Material bottleneck concerns; lithium and cobalt - Currently weak recovery and recycling schemes
Li-ion	<ul style="list-style-type: none"> + Moderate initial cost + Satisfactory specific energy and power + Satisfactory round-trip efficiency + Low O&M requirements + High reliability + Reliance on eco-friendly materials + Good safety record + Satisfactory operating temperature ranges + Relatively fast recharge + Relatively low initial cost + Outstanding calendar and cycle lives + Mature technology + High reliability + Low O&M requirements + Reasonable self-discharge rate + Good safety record + Extensive operating temperature ranges + Relatively fast recharge 	<ul style="list-style-type: none"> - High self-discharge rate - Slight memory effect - Relatively short cycle life - Currently weak recovery and recycling schemes
NiMH	<ul style="list-style-type: none"> + Moderate initial cost + Satisfactory specific energy and power + Satisfactory round-trip efficiency + Low O&M requirements + High reliability + Reliance on eco-friendly materials + Good safety record + Satisfactory operating temperature ranges + Relatively fast recharge + Relatively low initial cost + Outstanding calendar and cycle lives + Mature technology + High reliability + Low O&M requirements + Reasonable self-discharge rate + Good safety record + Extensive operating temperature ranges + Relatively fast recharge 	<ul style="list-style-type: none"> - Modest specific energy and power - Memory effect - Relatively low round-trip efficiency - Reliance on hazardous cadmium^b
NiCd	<ul style="list-style-type: none"> + Moderate initial cost + Satisfactory specific energy and power + Satisfactory round-trip efficiency + Low O&M requirements + High reliability + Reliance on eco-friendly materials + Good safety record + Satisfactory operating temperature ranges + Relatively fast recharge + Relatively low initial cost + Outstanding calendar and cycle lives + Mature technology + High reliability + Low O&M requirements + Reasonable self-discharge rate + Good safety record + Extensive operating temperature ranges + Relatively fast recharge 	<ul style="list-style-type: none"> - Modest specific energy and power - Memory effect - Relatively low round-trip efficiency - Reliance on hazardous cadmium^b

Figure A.1: Strengths and weaknesses of lead-acid, NiMH and NiCd batteries.

2 Dynamic analysis

The full 6-DOF non linear equation of motion here presented refers to the body-attached frame of the airplane.

$$\begin{cases} m(\dot{u} - rV + qW) = X & \text{(A.1a)} \\ m(\dot{v} - pW + rU) = Y & \text{(A.1b)} \\ m(\dot{w} - qU + pV) = Z & \text{(A.1c)} \end{cases}$$

$$I_x \dot{p} - (I_y - I_z)qr - I_{xz}(\dot{r} + pq) = L \quad \text{(A.1d)}$$

$$I_y \dot{q} + (I_x - I_z)pr + I_{xz}(p^2 + r^2) = M \quad \text{(A.1e)}$$

$$I_z \dot{r} - (I_x - I_y)qp - I_{xz}(\dot{p} - qr) = N \quad \text{(A.1f)}$$

3 Autonomous system cost breakdown

OBJECT	Number	Unit Price USD	Subtotal
Sonars	30	15,00	450,00
Long Range Radar	2	150,00	300,00
Short Range Radar	11	50,00	550,00
Lidar	2	200,00	400,00
Long Range Camera	2	200,00	400,00
Short Range Camera	11	60,00	660,00
Wide Angle Camera	1	100,00	100,00
GPS/DGPS	2	1000,00	2000,00
CPU/GPU	2	1000,00	2000,00
Other (antenas, pitote tubes, engines mounted sensors	2	1000,00	2000,00
		Total	8860,00
		+10% Margin Total	9746,00

Figure A.2: Autonomous system cost breakdown [70].

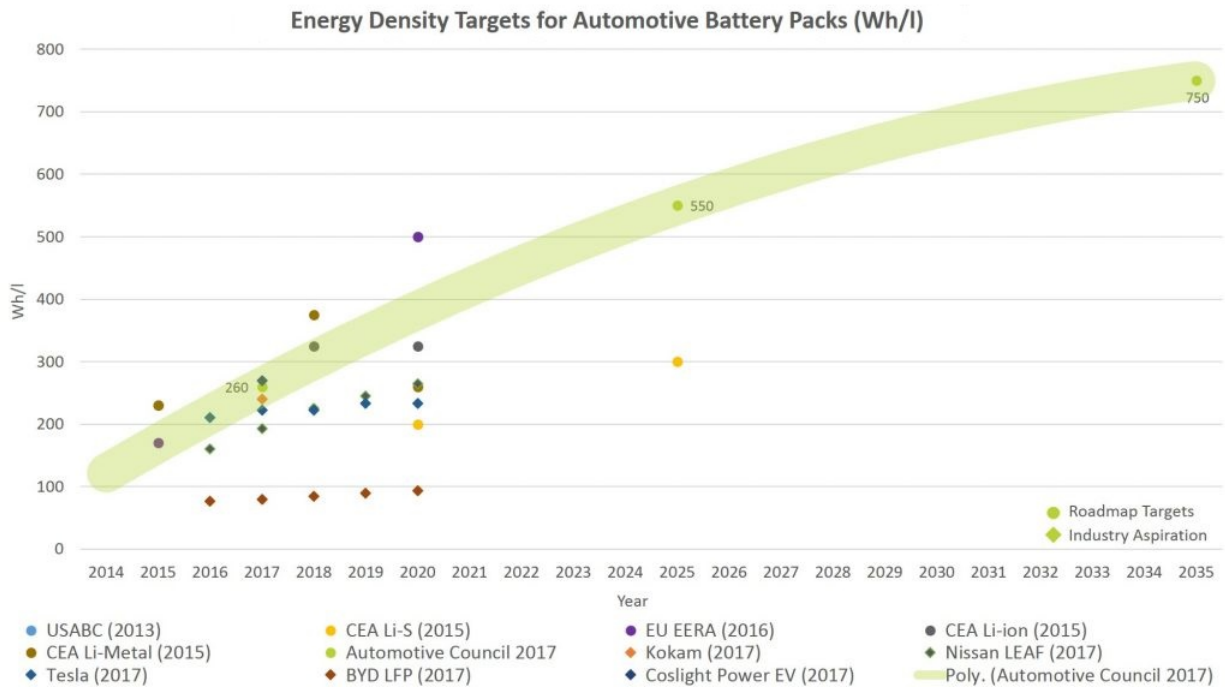


Figure A.3: Volumetric energy density trends.[69]

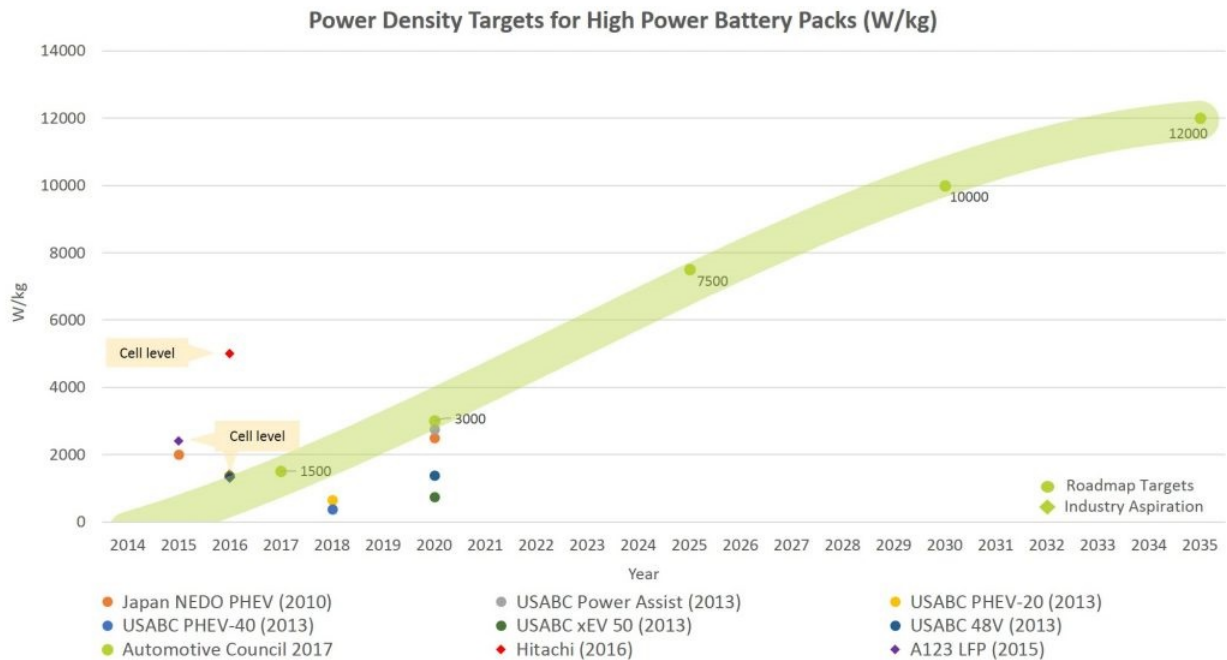


Figure A.4: Power density trends.[69]

4 Cost comparison between different means of transport

The sources from which the price of the different means of transportation are obtained are listed in this section. At the exception of the Mistral, prices were taken from booking websites, in typical conditions (working day, in the afternoon). When possible, the mean of transportation with similar comfort to the Mistral Air Taxi was chosen.

- **Mistral Air Taxi:** A customer cost per flight hour of 220 \$ is computed in order to have a margin of 400% on the

total cost per flight hour (see Table 1.43), accounting for any expense that would not have been included. The cost of the flight is then estimated by computing the travel time, based on the crow-fly distance and the cruise velocity of 150 mph.

- **Uber:** The price is estimated for the premium service UberBLACK, providing similar comfort, using Uber's estimator[62]. The travel time is estimated from Google Maps [61].
- **Bus:** The price and the estimated travel time are obtained from Greyhound Lines' website[63].
- **Train:** The price and the estimated travel time are obtained from Amtrak's website[64].
- **Small propeller aircraft:** The price and the estimated time are obtained from PrivateFly[65]. The airplane selected is a Cirrus SR-22.
- **Taxi:** The price and the estimated travel time are obtained from an online estimator website[63].
- **Helicopter:** As there is no direct line between the two airports but only between airports and heliports (see Fig. A.5), the price for one line provided by BLADE Airport[67] must be doubled. The travel time of 12 min[68] is also doubled. Ground transportation between helipads is included in the price.

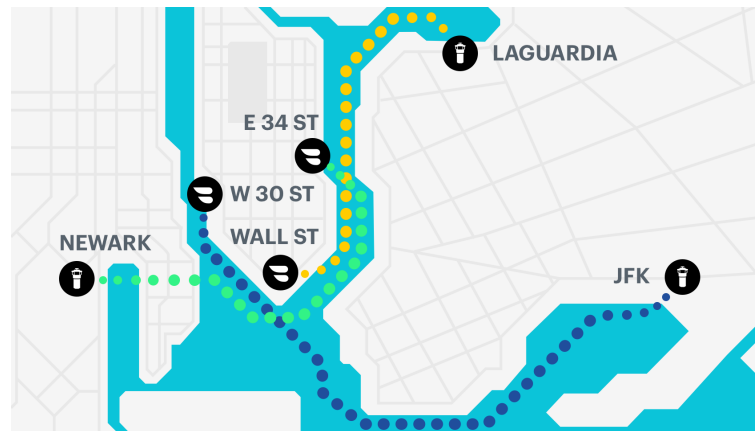


Figure A.5: BLADE Airport lines in New York.